Time-Resolved Surface Enhanced Resonance Raman Spectro-Electrochemistry of Heme Proteins

D I S S E R T A T I O N

zur Erlangung des Grades

"Doktor der Naturwissenschaften"

eingereicht

am Fachbereich Chemie, Pharmazie und Geowissenschaften

der Johannes Gutenberg-Universität in Mainz

Marc Großerüschkamp
geboren in Frankfurt am Main

Mainz, 08. November 2010

Dekan:

1. Berichterstatter:

2. Berichterstatter:

Tag der mündlichen Prüfung: 09.12.2010

Die vorliegende Arbeit wurde am Max-Planck-Institut für Polymerforschung in Mainz und am Austrian Institute of Technology (AIT) in Wien in der Zeit von Januar 2008 bis Dezember 2010 angefertigt.

Abstract

The membrane protein Cytochrome c Oxidase (CcO) is one of the most important functional bio-molecules. It appears in almost every eukaryotic cell and many bacteria. Although the different species differ in the number of subunits, the functional differences are merely marginal. CcO is the terminal link in the electron transfer pathway of the mitochondrial respiratory chain. Electrons transferred to the catalytic center of the enzyme conduce to the reduction of molecular oxygen to water. Oxygen reduction is coupled to the pumping of protons into the inter-membrane space and hence generates a difference in electrochemical potential of protons across the inner mitochondrial membrane. This potential difference drives the synthesis of adenosine triphosphate (ATP), which is the universal energy carrier within all biological cells. The goal of the present work is to contribute to a better understanding of the functional mechanisms of CcO by using time-resolved surface enhanced resonance Raman spectroscopy (TR-SERRS). Despite intensive research effort within the last decades, the functional mechanism of CcO is still subject to controversial discussions.

It was the primary goal of this dissertation to initiate electron transfer to the redox centers Cu_A, heme a, heme a_3 and Cu_B electrochemically and to observe the corresponding redox transitions in-situ with a focus on the two heme structures by using SERRS. A measuring cell was developed, which allowed combination of electrochemical excitation with Raman spectroscopy for the purpose of performing the accordant measurements. Cytochrome c was used as a benchmark system to test the new measuring cell and to prove the feasibility of appropriate Raman measurements. In contrast to CcO the heme protein cc contains only a single heme structure. Nevertheless, characteristic Raman bands of the hemes can be observed for both proteins.

In order to investigate CcO it was immobilized on top of a silver substrate and embedded into an artificial membrane. The catalytic activity of CcO and therefore the complete functional capability of the enzyme within

the biomimetic membrane architecture was verified using cyclic voltammetry. Raman spectroscopy was performed using a special nano-structured silver surface, which was developed within the scope of the present work. This new substrate combined two fundamental properties. It facilitated the formation of a protein tethered bilayer lipid membrane (ptBLM) and it allowed obtaining Raman spectra with sufficient high signal-to-noise ratios.

Spectro-electrochemical investigations showed that at open circuit potential the enzyme exists in a mixed-valence state, with heme a and and heme a_3 in the reduced and oxidized state, respectively. This was considered as an intermediate state between the non-activated and the fully activated state of CcO. Time-resolved SERRS measurements revealed that a hampered electron transfer to the redox center heme a_3 characterizes this intermediate state.

Contents

Chapter 1

Motivation

"The cost of living", an article by Peter Rich published by *Nature* in 2003 provides a remarkable and amazing calculation of what is needed – from the energetic and biochemical point of view – just to keep a human being alive [1]. A synopsis of this article is given in the next paragraph and is meant to motivate and to arouse interest in the reader for the scientific field of mitochondrial respiration.

The human body is a complex biological system of its physiological functions, which are based upon biochemical and molecular processes. It is not surprising that this complex structure requires energy even at rest. The amount of energy needed is quite amazing. At rest approximately $100\,\mathrm{k}cal/\mathrm{h}$, corresponding to $420\,\mathrm{kJ/h}$ or $116\,\mathrm{W}$, are needed. Under working conditions this is increased by a factor of up to six. Energy is stored in the form of adenosine triphosphate (ATP) and released by cleaving a phosphate group of ATP. A billion years ago the early eucariotic cell was invaded by a bacterium having a highly efficient system for utilizing available energy sources – the oxygen consuming respiratory chain, at the end of which ATP was synthesized. The genetic information was transferred to the nucleus, whereby the former bacterial symbionts were transformed into mitochondrial organelles. Therefore, today the major aspects of bacterial and mitochondrial respiration coincide.

In 1966 Peter Mitchell [2] won the Nobel Prize for showing that ATP syn-

thesis is driven by a protonmotive force, which is coupled to electron transfer. After all, electrons derived from food by a series of metabolic reactions are consumed in converting the oxygen we breathe into water. The five protein complexes forming the respiratory chain are embedded into the inner mitochondrial membrane. The ion-impermeable membrane seals the matrix from the inter membrane space. Therefore energy can by stored by building up pH and charge gradients across the membrane. Complex I, III and IV are known to pump protons into the inter membrane space, while complex V uses this gradient as the driving force for ATP synthesis. Complex IV - Cytochrome c Oxidase (CcO) - the most important link in this chain is the central element of the work presented in this dissertation. In order to illustrate the incredible performance of the respiratory chain and to envision the significance of efficiency an easy calculation is performed at this point:

Considering the 116 W an average human needs at rest, the basic physical law of electrical power ($P = U \cdot I$)[1] and the potential difference of 200 mV across the inner mitochondrial membrane, a current as high as $I = 522\,\mathrm{A} = 522\,\mathrm{C/s}$ results. A single proton carries a charge of $1.6 \cdot 10^{-19}\,\mathrm{C}$. The current of 522 A is therefore equal to a flux of $3 \cdot 10^{21}$ protons per second. Assuming 3.3 protons consumed on average for the synthesis of one ATP molecule [1] from ADP, this corresponds to a total of $9 \cdot 10^{20}$ ATP Molecules per second or $7.8 \cdot 10^{25}$ per day. The molecular weight of ATP is 507.18 g/mol. Therefore, the turnover rate of ATP is 65.7 kg per day.

In fact roughly 90% of the oxygen we breath is used to power this enormous turnover of the respiratory chain. The finding that the catalytic center of Cytochrome c Oxidase is the site where the oxygen is reduced to water [3] emphasizes the fundamental importance of this enzyme. An adult male consumes around 380 liters of oxygen every day in order to cover the energy demand. Hence approximately 340 L or 14 mol dioxygen are reduced to water by Cytochrome c Oxidase every day. During one catalytic cycle four electrons are consumed and one dioxygen molecule is reduced to water. Considering $2 \cdot\ 10^{19}$ molecules of CcO in the human body, approximately 20 electrons per second must be transferred to the catalytic center of every CcO

[1] P, U and I represent the power, voltage and current

molecule.

Within the past four decades CcO was extensively investigated with respect to its structure and function. In the mid-1990s the crystal structure of bovine heart and Paracoccus-Denitrificans CcO were determined by x-ray crystallography at 2.8Å resolution by Shinya Yoshikawa [4] and Hartmut Michel [5], respectively. The proton pumping mechanism, however, had been observed roughly twenty years earlier and was first described by Mårten Wikström [6] in 1977. Over the years the functional mechanism was investigated with great success. Alternative proton transfer pathways and different reaction intermediate species have been identified. It was shown that electrons were exchanged between four redox centers termed Cu_A, heme a, heme a_3 and Cu_B. Electrons, taken up by Cu_A are transferred via heme a to the binuclear catalytic center heme a_3 / Cu_B. IR spectroscopy and Raman spectroscopy proved to be particularly promising techniques for studying the role of CcO's redox centers as they are mutually complementary. IR spectroscopy is more sensitive to the protein environment of the redox centers, while Raman spectroscopy is a powerful tool to determine the redox, spin and coordination state of hemes. Exciting Raman scattering in the near uv frequency region matching the so-called Soret absorption band of heme proteins is referred to as resonance Raman scattering. Resonance Raman scattering is distinguished by an increased scattering intensity. In the majority of cases CcO was investigated in the solubilized form. Electron transfer was then achieved by mediators exchanging charges with the individual redox centers. Recently a new approach was introduced based on the immobilization of the protein embedded into a biomimetic artificial membrane. For this purpose his-tagged protein was tethered in a unidirectional orientation to metal substrates and subsequently stabilized by reconstitution into a protein tethered bilayer lipid membrane (ptBLM). The use of metal substrates offers the possibility of applying electrical potentials on the one hand and of taking advantage of the surface enhancement effect on the other. Surface enhancement is achieved by using metal substrates, which show localized surface plasmon resonances due to a definite roughness on the nano-scale.

It is the primary goal of the present dissertation to quantify the elec-

tron transfer rate to Cytochrome c Oxidase in an artificial biomimetic membrane architecture by time-resolved surface-enhanced resonance Raman spectroscopy (TR-SERRS). For this purpose different intermediate steps had to be achieved. A measuring cell had to be designed allowing reliable and reproducible SERRS measurements. Therefore the following criteria had to be met:

- electron transfer can be triggered electrochemically
- photo degradation must be avoided
- allowing anaerobic conditions
- high mechanical stability.

The measuring cell and the SERRS setup had to be tested. This was done by investigating electron transfer to the water soluble heme protein cytochrome c as a benchmark system. A nano-structured silver surface had to be designed allowing both surface-enhanced Raman spectroscopy and membrane reconstitution after protein immobilization. In a final step electron transfer to the redox centers of Cytochrome c Oxidase had to be monitored by static potential dependent SERRS, before kinetic parameters of electron transfer could be derived from TR-SERRS experiments using the ptBLM.

Chapter 2

Introduction

2.1 The Mitochondrial Respiratory Chain

Mitochondria are organelles found in most eucariotic cells. As all organelles they are designed to fulfill a specific task. In this case it is the conversion of oxygen into water. Mitochondria are located in the cytoplasm of the cells and are enclosed by a bilayer lipid membrane (BLM). Adenosine triphosphate (ATP) is the universal energy carrier within higher organisms such as the human body. Most of the ATP is generated by mitochondria. Thus, they are often referred to as the power plants of biological cells. The outer membrane seals the mitochondrion from the cytoplasm. However, different protein complexes functioning as channels are incorporated providing the possibility of exchanging salts, among other compounds, with the cytosol. Beside the outer membrane, separating the organelle from the cell's cytoplasm there is a second membrane, the mitochondrion's inner membrane (see Figure 2.1). The typical lamalla-like structure demonstrated in the TEM image shown in Figure 2.2 is generated by the arrangement of this inner membrane, which forms compartments the so-called cristae. A class of membrane proteins is incorporated into the inner membrane, which in turn forms a functional unit, the mitochondrial respiratory chain. The task of the respiratory chain is to recycle ADP to ATP. This recycling takes place primarily through oxidative phosphorylation (OP). OP is the process in which ATP is formed

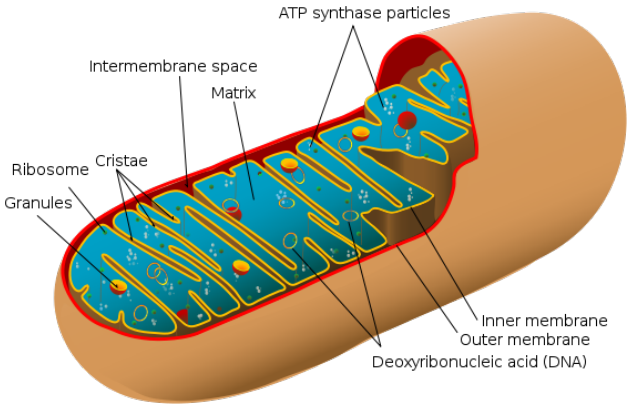

Figure 2.1: Schematic cross-section of a mitochondrium. A characteristic is the lamella-structure of the inner mitochondrial membrane. By this structure the total surface area of the membrane is increased. Therefore more proteins can be incorporated and the effectiveness is increased.

Figure 2.2: TEM image of a mitochondrium. The lammalla-structured inner membrane is easily recognized.

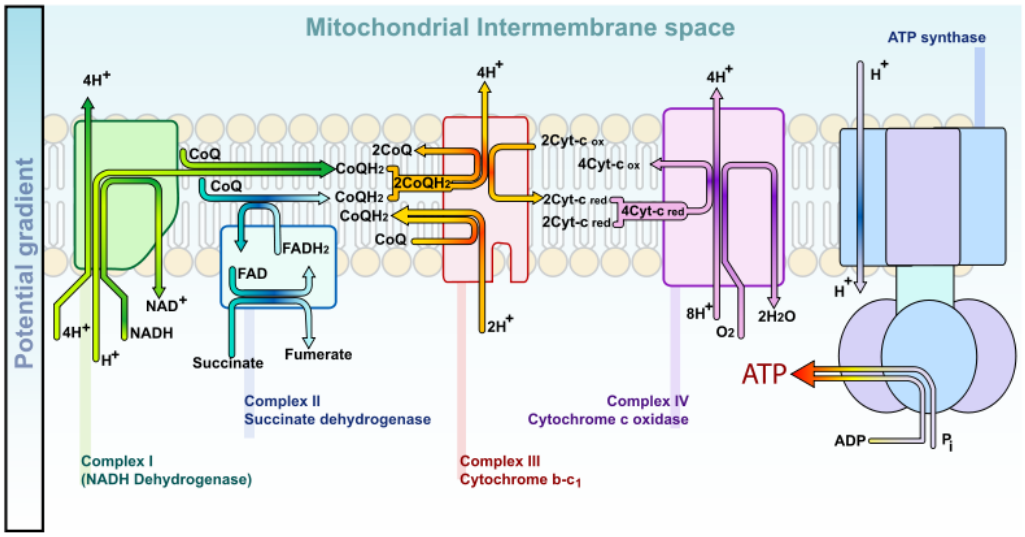

Figure 2.3: The mitochondrial respiratory chain. At the end of the chain ATP is formed by the proton-driven ATP-synthase. The proton gradient is generated by complex I, III and IV.

as a result of the transfer of electrons from NADH or $NADH_2$ to O_2 by a series of electron carriers (complexes I-IV). The electron transfer potential of $NADH/NADH_2$ relative to that of O_2 is the driving force of OP. It drives the proton translocation across the inner membrane. The proton gradient generated is then used by the protein ATP-synthase (complex V) to convert ADP to ATP. The total chemical reaction of complex I to IV can be expressed in a simple chemical reaction scheme:

$$\frac{1}{2}O_2 + NADH + H^+ + 10H_i^+ \rightarrow H_2O + NAD^+ + 10H_o^+ \qquad (2.1)$$

The change in free enthalpy due to the conversion of NADH and O_2 to NAD^+ and H_2O amounts to $\Delta H_{NADH} = -220\,\mathrm{kJ/mol}$. At the same time the change in free enthalpy due to the transport of a single proton into the inter-membrane space is $\Delta H_{H^+} = 21.82\,\mathrm{kJ/mol}$. Accounting for the 10 protons pumped during one cycle this sums up to $\Delta H_{10\,H^+} = 218.2\,\mathrm{kJ/mol}$, which is just slightly less then ΔH_{NADH} envisioning the high efficiency of this enzymatic cycle. A more detailed treatment of the biochemical aspects

of mitochondrial respiration can be found in reference [7]. Complex IV, which is termed cytochrome c oxidase (CcO), plays a central role within the respiratory chain. CcO is the protein within which the molecular oxygen we breath is reduced to water. The mechanisms of electron transfer, proton translocation and oxygen reduction of CcO are discussed in chapter 2.1.1.

2.1.1 Cytochrome c Oxidase

Cytochrome c Oxidase (CcO) is the terminal enzyme in the respiratory chain of mitochondria and aerobic bacteria. It is composed of four subunits (SU): SU I (63 kDa), SU II (29 kDa), SU III (30 kDa) and SU IV (5.4 kDa). The structure of CcO as obtained by X-ray diffraction [8] is depicted in Figure 2.4.

By transferring electrons from cytochrome c to molecular oxygen the latter is catalyzed to water [9, 10]. This process is coupled to a translocation of protons across the membrane [11] into which CcO is embedded. The resulting proton gradient drives the synthesis of ATP by ATP-synthase [11]. During one catalytic cycle four electrons are taken up and one dioxygen is reduced to water, while four protons are pumped [12]:

$$4\ cytochrome\, c^{2+} + 8\ H_i^+ + O_2 \longrightarrow 4\ cytochrome\, c^{3+} + 4\ H_o^+ + 2\ H_2O \quad (2.2)$$

where H_i^+ and H_i^+ represent the protons taken up from the inside of mitochondria or bacteria and the protons released at the outside, respectively. Cytochrome c, which is located at the outside delivers four electrons to the binuclear center Cu_A, which is the first of four redox centers and is located close to the outer membrane surface. Subsequently electrons are transfered to the next center, a low-spin heme a. Finally the electrons reach the binuclear center hema a_3-Cu_B. At this site the catalytic reduction of oxygen takes place [13, 14]. Therefore this center is also referred to as the catalytic center. The arrangement of the four redox centers is depicted in Figure 2.5. SU II contains Cu_A that receives electrons from cc; heme a, heme a_3, and Cu_B are incorporated in SU I. Ludwig et al. [15] reported that a complex of SU I and II of the CcO from P.*dentrificans* is already fully active with

respect to both dioxygen reduction and proton pumping. Together with SU III they are referred to as the core parts or core subunits of the enzyme, since they are present in most terminal heme-copper containing terminal oxidases. Depending on the origin of a specific CcO molecule more SUs may be attached. However, in most of the cases the function of these additional SUs is not understood yet.

A detailed discussion of the catalytic cycle and the mechanism of proton pumping can be found in a discussion of H. Michel [12]. Another article of potential interest to the reader deals with the remaining mysteries of CcO [16].

2.1.2 Cytochrome c

The heme protein cytochrome c functions as the electron carrier between complex III and IV of the mitochondrial respiratory chain. One electron is taken up from complex III by converting the central iron from Fe^{3+} to Fe^{2+}. Subsequently the electron is then transfered to complex IV (CcO). Furthermore, cc seems to play an essential role in apoptosis (programmed cell death) [17, 18]. A pro-apoptotic signal stimulates the release of cc from mitochondria. This triggers a further signal cascade leading to apoptosis. However, the role of apoptosis is not within the scope of this work; rather the focus of the present work lies in the electron transfer mechanism of cc.

2.2 Membrane Proteins and Biomimetic Architectures

The review article by Tan et al. [19] provides an excellent overview of the importance of membrane proteins: biological membranes form an essential barrier between living cells and their external environments, as well as serve to compartmentalize intracellular organelles within eukaryotes. The latter include membranes that envelope the nucleus, the outer and inner membranes of the mitochondria, membrane cisternae complex of the endoplasmatic reticulum, Golgi apparatus, as well as lysosomes and secretory vesicles.

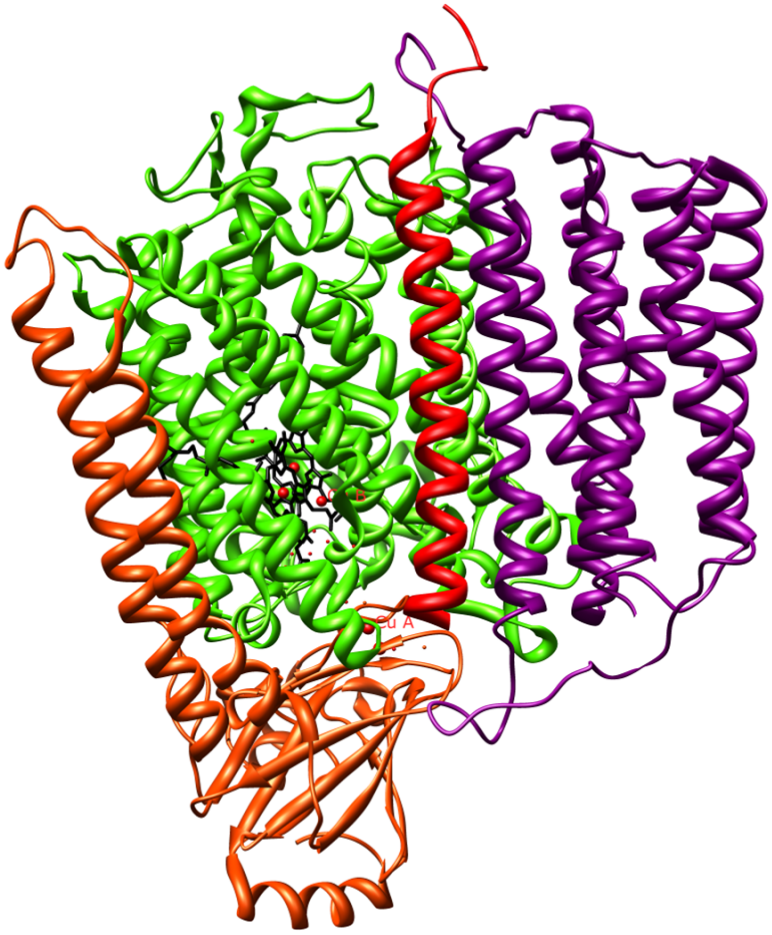

Figure 2.4: The structure of Cytochrome c Oxidase. It is composed of four subunits: SU I (green), SU II (bronze), SU III (purple) and SU IV (red). The catalytic center together with heme a is located in SU II, while Cu_A is situated in SU I.

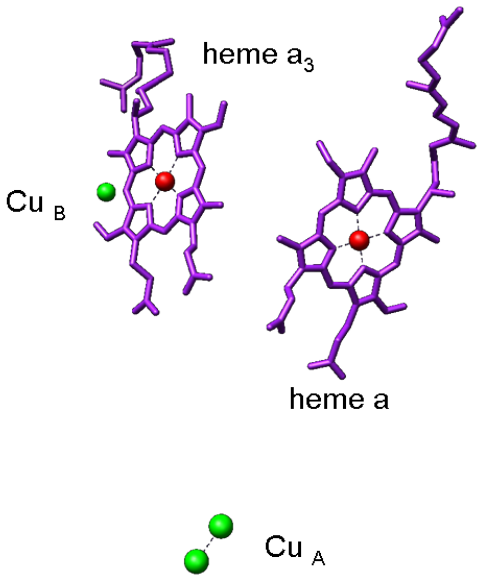

Figure 2.5: Cytochrome c Oxidase exhibits 4 redox centers. The binuclear center Cu_A by which electrons are taken up from cytochrome c, a low-spin heme a and the heme a_3-Cu_B catalytic center, where oxygen is reduced to water.

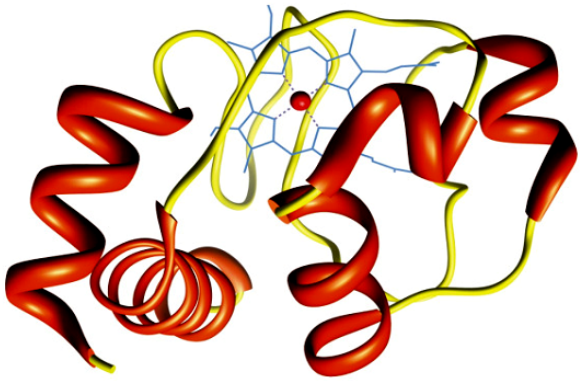

Figure 2.6: Cytochrome c is the electron acceptor of cytochrome c reductase (bc_1 complex or complex III) and the electron donor of cytochrome c oxidase. Therefore this protein can be seen as an electron carrier. Cytochrome c is a heme protein containing a single c heme.

Depending on their localizations in the whole organism and also within the cell, these membranes have different, highly specialized functions. Although 30% of naturally occurring proteins are predicted to be embedded in biological membranes, membrane proteomics is traditionally understudied due to difficulties in solubilizing, separating, and identifying membrane proteins. Given the importance of membrane proteins in the various cellular processes (such as signal transduction, ion transport and enzymatic metabolism) as well as the roles they play in diseases and their potential as drug targets, it is imperative that this class of proteins be better studied.

The authors point out that this class of proteins is understudied due to difficulties with, among other factors, the solubilization of the mostly hydrophobic molecules. However, even after extraction, purification and sulubilization of a membrane protein the study of their native function is not trivial. The proteins need to be in an environment which replaces the native lipid membrane in order not to alter the protein structure or to disable their native function. Throughout this work a novel membrane architecture was used to mimic the native lipid membrane: the protein tethered bilayer lipid membrane [20, 21] (ptBLM).

2.2.1 Protein Tethered Bilayer Lipid Membrane

The ptBLM is an artificial membrane system mimicking the the native biological lipid membrane. Such biomimetic systems are needed when proteins are extracted from their native environment and then probed in an artificial environment, because the integrity and function of protein strongly depends on the right environmental conditions. The ptBLM is formed in two steps. At first the protein which is surrounded by detergent molecules is immobilized on top of a metal substrate. In the second step the tethered protein is stabilized by reconstitution into a bilayer lipid membrane. The membrane is formed by dialysis using biobeads (Figure 2.7). In contrast to tethered bilayer lipid membranes (tBLM) the protein is tethered instead of the lipid. This is advantageous since the distance between the membrane and the metal surface is determined by the protein itself. In the case of tBLMs spacer-molecules

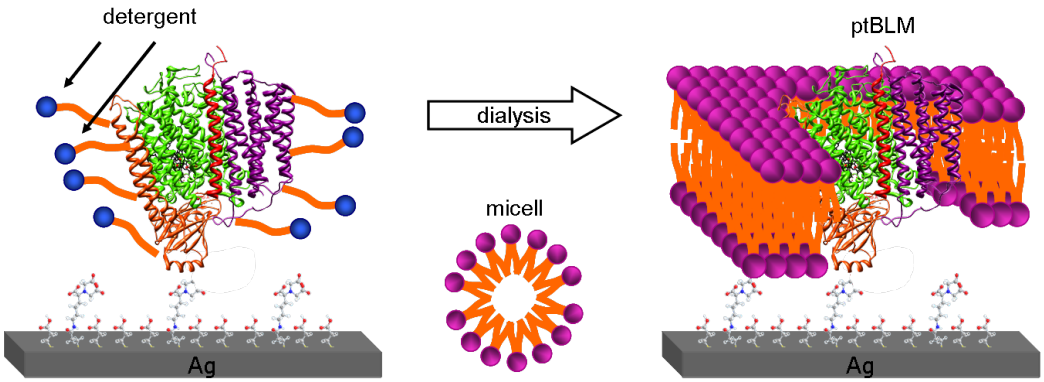

Figure 2.7: The ptBLM. CcO is tethered to a metal substrate using the his-tag technology. Thereafter the protein is stabilized by reconstitution into a bilayer lipid membrane.

with the right length must be used for tethering the lipids. Otherwise not enough room is provided for the protein or the distance is too long, causing an instabilities within the membrane. The protein is tethered to the metal substrate by using a histidine-anchor (his-tag) as shown in Figure 2.8. His-tag anchors attached to proteins are frequently used for the purification of the protein. The metal is functionalized with a specific linker molecule. The histidine, the -COOH termini of the linker molecule together with a Ni^{2+} ion form a chelate complex, thus binding the protein to the surface. An important characteristic of the ptBLM is the immobilization of the protein in an unidirectional fashion. If the his-tag is engineered to the c-terminus of SU II, CcO is tethered with the cytochrome c binding site directed towards the metal surface. Applying electric potentials between the metal substrate and a counter electrode leads to the exchange of electrons between the metal substrate and the redox centers of CcO. This phenomenon is referred to as electronic wiring of the protein [20]. The mechansm is illustrated in Figure 2.9.

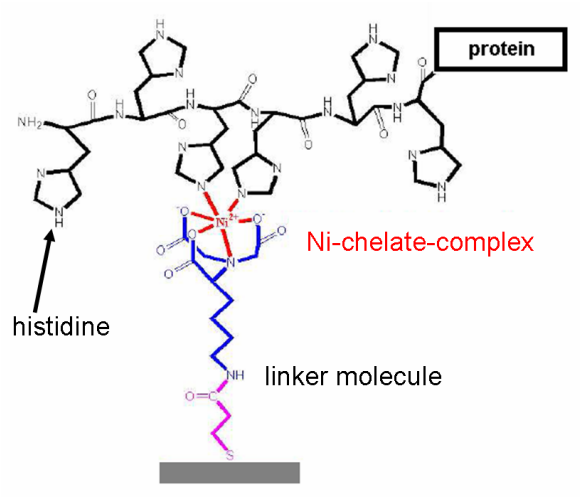

Figure 2.8: A coordinating Ni-ion is used to form a chelate complex together with the his-tag of the protein and the linker molecule.

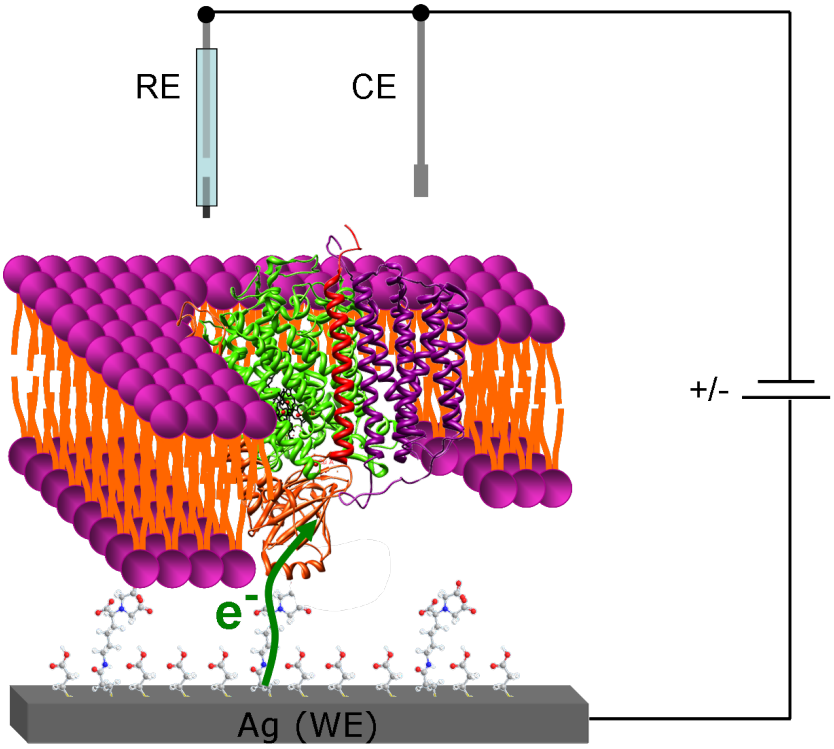

Figure 2.9: By applying electric potentials between the silver substrate (WE) and the counter electrode inserted into the PBS buffer solution a direct electron transfer between metal and protein is achieved. Due to the orientation of the protein electrons are transferred to the Cu_A center. Thereafter electrons are sequentially transmitted to the redox centers heme a, heme a_3 and Cu_B.

Chapter 3

Theory

3.1 Raman Spectroscopy

In 1928 Raman and Krishnan [22] showed that in every case in which light is scattered by molecules, either in the gas or the liquid phase, the diffuse radiation having the same frequency as the incident beam, is accompanied by a modified scattered radiation of degraded frequency. This was proved by an experiment in which sunlight was scattered by different samples. They used a telescope to converge the light from the sun, which was passed through a blue-violet filter before irradiating the sample. A second filter (yellow-green) was used to filter the scattered light. Indeed they found scattered light exhibiting a shift in the frequency. Therefore this *new type of secondary radiation*, so the title of their manuscript, was named Raman scattered light. In 1930, Chandrasekhara Venkata Raman received the Nobel Prize in physics for the discovery of this effect.

3.1.1 Molecular Vibrations

3.1.2 Raman Effect

C.V. Raman showed that light is not only elastically scattered by molecules. In fact also inelastic scattering can occur. Inelastic scattering results, when a molecular vibration is excited. An energy difference between the incident and

Figure 3.1: Chandrasekhara Venkata Raman, * November 7th 1888 in Tiruchirappalli, † November 21st 1970 in Bangalore

the inelastically scattered light is than observed concurrent with the energy of the molecular vibration. However the elastic scattering is much stronger and the inelastically scattered light is only observed when specially designed Raman setups are used to filter the Rayleigh scattered light. The scattering cross-section of Raman scattering is in the order of magnitude of $10^{-30}\,\mathrm{cm}^2$. In fact this is the major drawback of this analytical technique.

Considering the quantum mechanical aspects of Raman scattering the reason for the low scattering cross section becomes obvious. At the same time this point of view demonstrates how Raman intensities can be increased. In figure 3.2 the ground state S_0 and the first vibrational excited state n_1 of a molecule are shown. The incident exciting laser light (today only monochromatic laser light is used in Raman experiments) has the frequency ν_e. Therefore the energy is given by

$$E_e = \hbar\,\nu_e. \tag{3.1}$$

The scheme in figure 3.2 illustrates that the energy E_e is higher than the energy difference to the next vibrational excited state, but at the same time smaller than the energy difference to the first electronic excited state S_1.

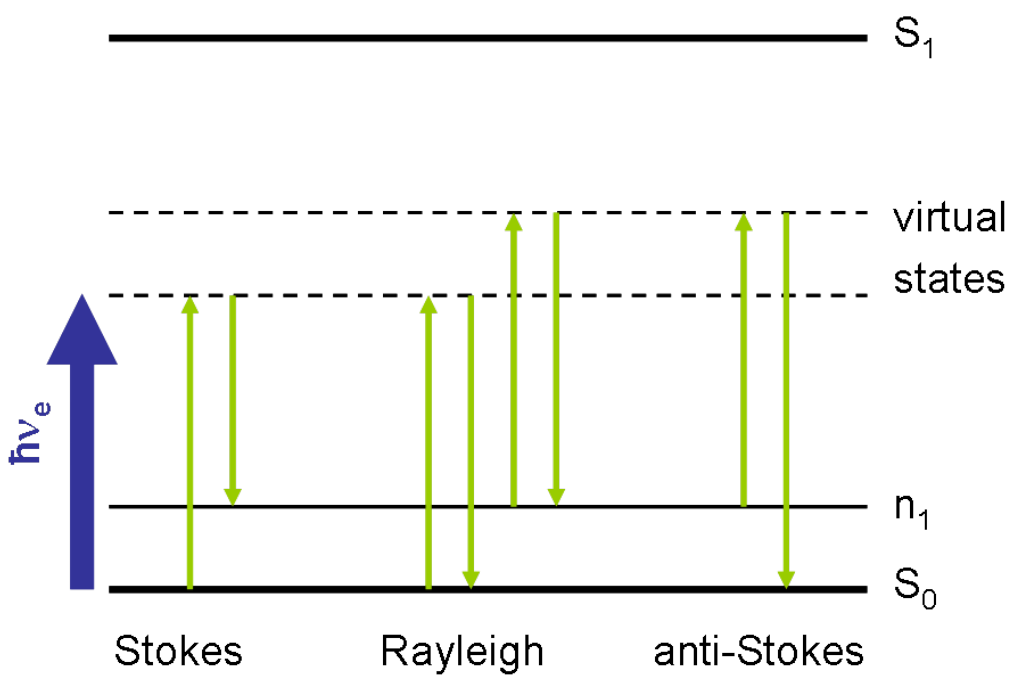

Figure 3.2: Energy differences in Raman scattering. The ground state S_0, the first electronic excited state S_1 as well as virtual states and vibrational states n_1 are shown. In the case of Stokes and anti-Stokes Raman scattering the wavelength of incident light is up-shifted and down-shifted, respectively.

Therefore the photon is not absorbed but scattered. The intermediate excited state is a so-called virtual state because it is quantum mechanically not allowed. The molecule instantaneously returns to the ground state S_0 (Rayleigh scattering), or with a marginal chance to a vibrational excited state n_1(Stokes Raman scattering). In the latter case the frequency of the scattered light is down-shifted. For normal Raman scattering the ratio of elastic and inelastic light scattering is $10^7 : 1$ [23]. If a molecule is already present in the excited state n_1, after excitation to a virtual state can return to S_0. The frequency is therefore shifted to higher frequencies which is called anti-Stokes Raman scattering. However, the first case is much more likely, since at room temperature the ground state is dominant. The instable virtual state explains the low cross-section of Raman scattering [23]. Since the residence time in the virtual state is extremely short it is unlikely that a

molecular vibration is excited by transmitting kinetic energy to the nuclei. Hence, the chance to excite such molecular vibrations is increased if not a virtual state but a real electronic excited state is intermittently formed. This is a special case of Raman scattering and is discussed separately in Section 3.1.3.

Considering the incident laser light as an oscillating electromagnetic field, it gives rise to a quasi-classical view of the Raman effect. The incoming electric field **E** induces a dipole moment

$$\mu_{ind} = \alpha \cdot \mathbf{E}. \tag{3.2}$$

Here, α is the polarizability, which is a function of the displacement q from equilibrium q_0. Therefore the photon emitted by the induced dipole moment can be modulated by an excited molecular vibration. The electric component of the laser light is described by the electric field vector

$$\mathbf{E} = \mathbf{E_0} \cdot \cos(2\pi\nu_0 t). \tag{3.3}$$

Therefore Equation 3.2 can be written as

$$\mu_{ind} = \alpha \cdot \mathbf{E_0} \cos(2\pi\nu_0 t). \tag{3.4}$$

An excited molecular vibration will distort the electron cloud during the oscillation and therefore change the polarizability periodically. The polarizability can be written as a Taylor expansion about the equilibrium geometry:

$$\alpha = \alpha_0 + \left(\frac{\partial\alpha}{\partial q}\right)_0 q + \frac{1}{2}\left(\frac{\partial^2\alpha}{\partial q^2}\right)_0 q^2 + ... \tag{3.5}$$

where α_0 is the equilibrium value of α and q is the deviation from equilibrium. Due to the harmonic excitation the deviation is also described by a harmonic oscillation:

$$q = q_0 \cdot \cos(2\pi\nu t) \tag{3.6}$$

Substituting q in Equation 3.5 leads to

$$\alpha = \alpha_0 + \left(\frac{\partial \alpha}{\partial q}\right)_0 q_0 \cdot \cos(2\pi\nu t) + ... \tag{3.7}$$

neglecting the second derivative for the sake of simplicity. Further substituting Equation 3.7 into Equation 3.4 results in

$$\mu_{ind} = \alpha_0 \cdot \ \mathbf{E_0} \cos(\omega_0 t) + q_0 \cdot \mathbf{E_0} \left(\frac{\partial \alpha}{\partial q}\right)_0 \cdot \cos(\omega_0 t) \cdot \cos(\omega t), \tag{3.8}$$

where $2\pi\nu$ and $2\pi\nu_0$ was replaced by ω and ω_0, respectively. Using the trigonometric identity

$$\cos(s) \cdot \cos(b) = \frac{1}{2}\left[\cos(a+b) + \cos(a-b)\right], \tag{3.9}$$

the expression for the induced dipole becomes

$$\begin{aligned} \mu_{ind} = \underbrace{\alpha_0 \cdot \ \mathbf{E_0} \cos(\omega_0 t)}_{Rayleigh} + \underbrace{q_0 \cdot \mathbf{E_0} \left(\frac{\partial \alpha}{\partial q}\right)_0 \cdot \cos((\omega_0 - \omega)t)}_{Stokes} + \\ \underbrace{q_0 \cdot \mathbf{E_0} \left(\frac{\partial \alpha}{\partial q}\right)_0 \cdot \cos((\omega_0 + \omega)t)}_{anti-Stokes}. \end{aligned} \tag{3.10}$$

The first term describes Rayleigh scattering. The frequency of the incident light ins not altered but re-emitted with the same frequency ω_0. The second term represents Stokes Raman scattering, where the frequency of incident light is changed to lower values and therefore higher wavelength. The last term describes the case of anti-Stokes Raman scattering. Here the frequency of the scattered light is up-shifted due to the elimination of a vibrational mode as shown in figure 3.2.

Furthermore from Equation 3.10 one can derive the selection rules for Raman-active vibrations. Obviously the first derivative of α shows that

Stokes or anti-Stokes Raman scattering can occur, only if

$$\left(\frac{\partial \alpha}{\partial q}\right)_0 \neq 0 \tag{3.11}$$

and the second and third term in Equation 3.10 are different from zero. Hence, Raman scattering can only occur if the polarizability of a molecule changes during vibration [23–25].

The intensity of the Raman scattered light I_{RS} finally depends on the frequency of the exciting laser light ω_0, the polarizability α of the probed molecule and the intensity of the incident light I_0:

$$I_{RS} = C \cdot I_0 \cdot \alpha^2 \omega^4 \tag{3.12}$$

C consists of constants and is given given by $C = \frac{8\pi}{9c}$ [24].

3.1.3 Resonance Effect

In section 3.1.2 the principle of normal Raman scattering was demonstrated. An essential characteristic of Raman scattering is the excitation of a so-called virtual state, which persists only for the time of the molecule-photon interaction. The extremely short lifetime of this virtual state was mentioned to be the reason for the low scattering cross-section. However, depending on the molecule, which is probed and the laser frequency used for excitation, the frequency of the laser light can be in resonance with a real electronic transition of the molecule. Therefore, no unstable virtual state is excited, but a real electronic excited state, which has a longer durability (Figure 3.3). The probability to induce a molecular vibration is increased. The distortion of the electron cloud persists long enough for the nuclei to relax to the equilibrium geometry of the excited state. Resonance Raman (RR) scattering was first observed by Shorygin [26] in 1947. The mechanism was explained by Albrecht [27]. The enhancement due to RR scattering is often in the order of 10^3 or 10^4 [25]. Spiro applied RR scattering to heme proteins [28, 29], which have a strong absorption in the near UV region due to a $\pi - \pi^*$ electronic transition. The resulting absorption band is the so-called Soret-

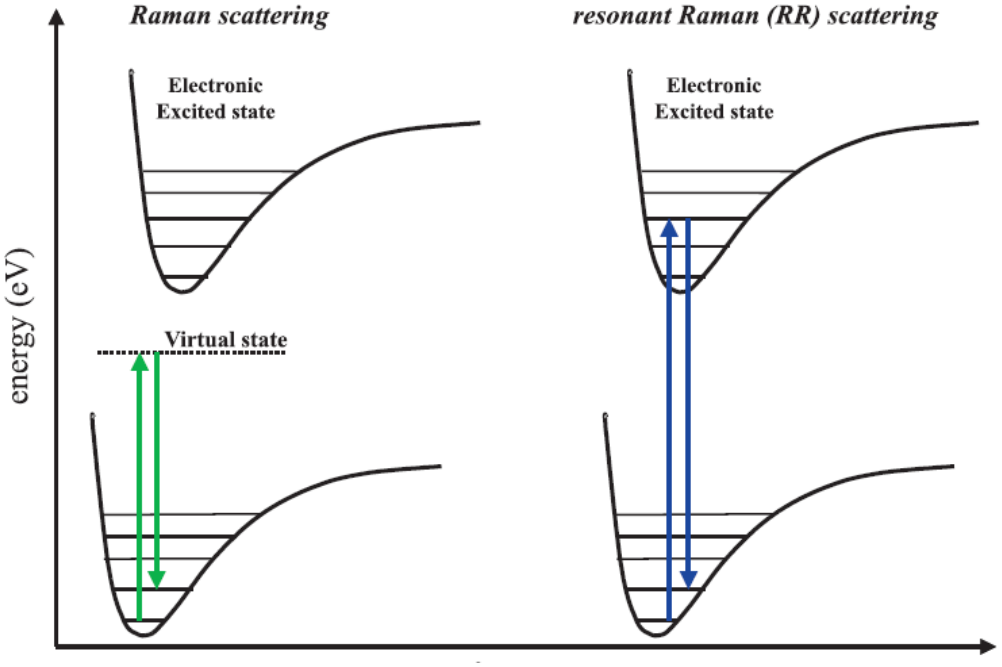

Figure 3.3: The difference between *normal* Raman scattering and resonance Raman scattering. In *normal* Raman scattering a virtual state is excited, stable only for the duration of the interaction with the photon. In resonance Raman scattering a real electronic excited state is intermittently reached. The electronic excited state is stable for a longer time-span, whereby the chance to excite a molecular vibration is enhanced.

band which was already discovered in 1883 by Soret [30]. RR scattering of hemes and heme proteins is described in 3.1.3.

RR Scattering at Heme Proteins

A large family of proteins is characterized by the incorporation of one or more heme structures. A heme is composed of a porphyrin ring in the center of which a metal ion is located. Porphyrins are symmetric ring structures and organic chromophores. They are composed of four pyrrole rings. In hemes the porphyrin ring is the ligand of the central metal ion (Figure 3.4). Further functional groups can be attached to the porphyrin. Thereby different kinds of hemes (for example heme a, b or c) are distinguished. The extended π sys-

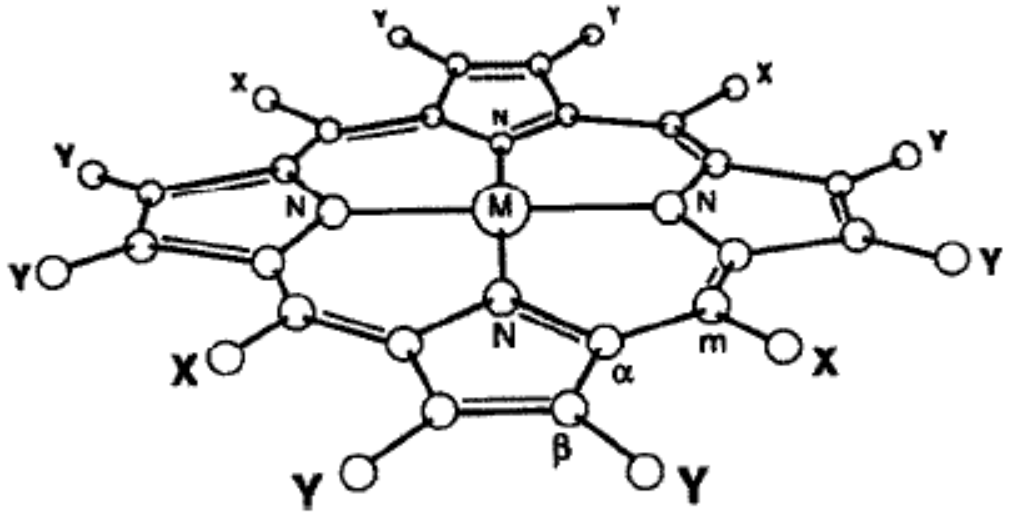

Figure 3.4: A heme is composed of a porphyrin ring. The center of which is a metal ion (M). The nitrogen atoms are labeled N. The various carbon atoms are labeled α, β or m, depending on their position. Various heme types differ in the functional groups labeled X or Y which are attached to the outer carbon atoms.

tem gives rise to a relatively small HOMO-LUMO[1] energy gap (ca. 2eV), and consequently metalloporphyrins absorb light strongly in the visible region of the spectrum [31]. As discussed in chapter 3.1.1 and 3.1.2 the absorption of light is accompanied by the excitation of vibrational excited states. Early heme protein studies revealed ground state vibrational frequency shifts associated with the ligation chemistry of the heme group. Subsequent work has uncovered useful correlations between structure and spectra, including sensitivities of specific band frequencies to the ligation, oxidation and spin state of the central metal ion [31]. Most of the RR bands have been assigned to metalloporphyrin normal modes on the basis of extensive isotope substitution studies [32, 33]. For better understanding the most fundamental vibrational modes are depicted in Figure 3.5. In the work of Kitagawa et al. [34] the various vibrational modes of the Ni-octaethylporphyrin (Ni-OEP) spectrum were assigned to designations ν_i. Until today these designations are used for

[1]HOMO = highest occupied molecular orbit; LUMO = lowest unoccupied molecular orbit

ν_i	Description	Ni-OEP
ν_2	$\nu_(C_\beta - C_\beta)$	1602
ν_3	$\nu_(C_\alpha - C_m)_{sym}$	1520
ν_4	$\nu_(Pyr - half - ring)_{sym}$	1383
ν_{10}	$\nu_(C_\alpha - C_m)_{asym}$	1655
ν_{11}	$\nu_(C_\beta - C_\beta)$	1577
ν_{12}	$\nu_(Pyr - half - ring)_{sym}$	1331
ν_{14}	$\nu_(C_\beta - Y)_{sym}$	1131

Table 3.1: Skeletal vibrational modes (Figure 3.5) assigned to designations (ν_i) and the wavenumber (given in in cm^{-1}) at which they appear in the Ni-OEP spectrum.

a distinct denomination of Raman modes originating from porphyrin structures such as hemes. In Table 3.1 the most important mode designations are given. It turned out that another advantage of RR scattering is that in chromophores such as hemes the charge-transfer transitions of the inherent metal complex generally enhance metal-ligand stretching modes. These modes are sensitive for the redox state of the central metal ion (e.g. ν_4). Therefor the intensity of the corresponding bands can be used as a marker for the redox state of heme proteins.

An excellent review about the spectroscopy on metalloporphyrins is given in reference [31] to which the more interested reader is referred to.

3.1.4 Surface Enhancement

Surface-enhancement (SE) plays a crucial role for the Raman experiments presented in the scope of this dissertation. Most recent studies by other research groups focus on solubilized CcO and use mediated electron transfer to the redox centers. By using high concentrations of dissolved protein and large sample volume sufficiently high signal to noise ratios are easily reached. However using the concept of the ptBLM leads to the fact that only a monolayer of molecules is probed. Hence, the number of scattering centers and therefore observed Raman intensities are strictly limited. To overcome this limitation and to reach significantly higher Raman intensities allowing quan-

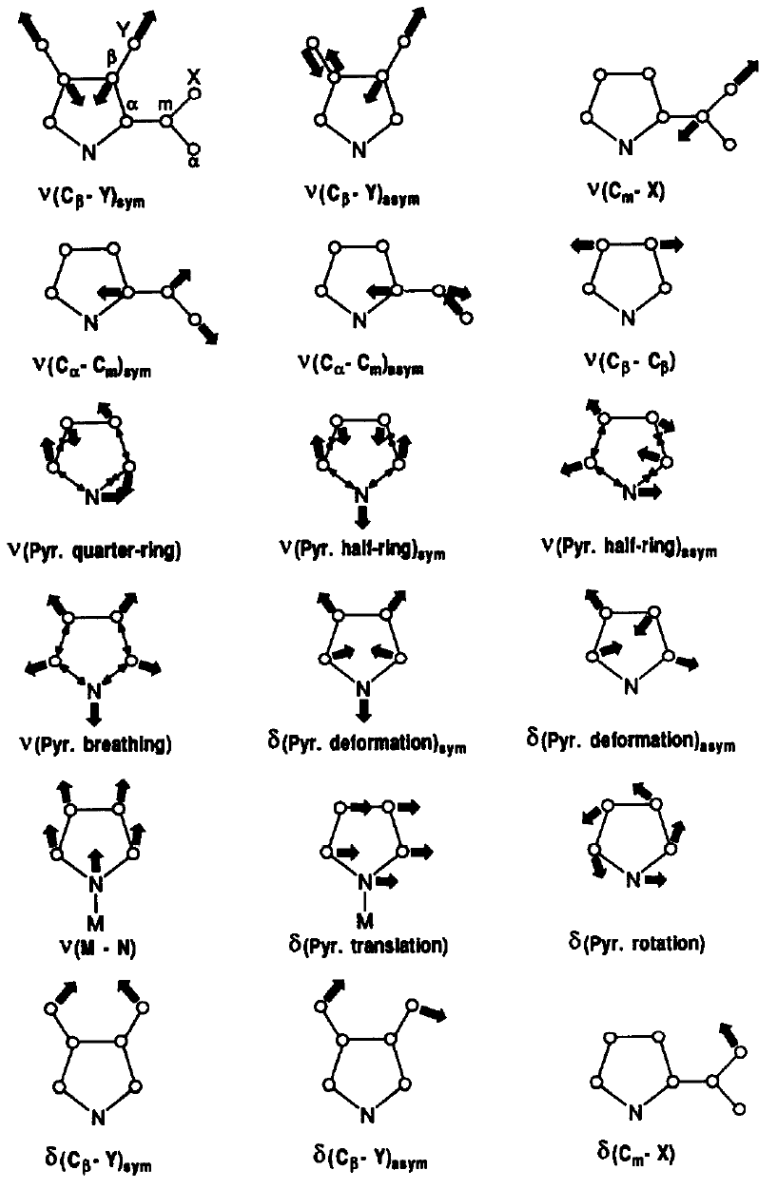

Figure 3.5: Illustration of the in-plane porphyrin skeletal vibrational modes. From Reference [31].

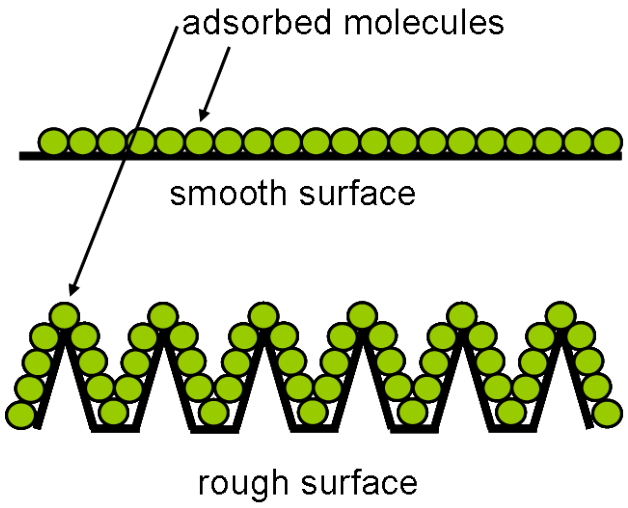

Figure 3.6: On roughened surfaces potentially more molecules can be adsorbed. Martin Fleischmann et al. used this approach to increase the Raman signal of adsorbed pyridine on silver and by chance discovered the surface enhancement effect.

titative analysis of the spectra surface-enhanced Raman spectroscopy(SERS) was employed.

The surface-enhancement effect (SEE) was discovered by chance in 1974 by Martin Fleischmann [35] and co-workers. They intended to study pyridine adsorbed to silver substrates, but the yield of Raman intensity was poor and the spectra were not significant. In order improve the signal-to-noise ratio they roughened silver electrodes as they planned to increase the effective surface area, hence to adsorb more molecules (Figure 3.6). As a result of the surface enhancement the spectra were now much more meaningful. Consequently two types of pyridine adsorption at the silver electrode were identified. However the enhanced Raman scattering intensity was attributed to the increased effective surface area of the roughened silver.

Years later Jeanmaire and Van Duyne [36] published an article titled *Anomalously Intense Raman-Spectra Of Pyridine At A Silver Electrode* as they noticed the enhancement could not only be due to the increased number of molecules. They proposed an electromagnetic effect to explain such intense Raman spectra. At he same time Albrecht and Creighton [37] proposed

a charge transfer effect to be the causation of enhancement. Today it is known that both, the charge transfer as well as the electromagnetic effect contribute to surface enhanced Raman scattering. Nevertheless, the surface enhancement effect is not completely understood yet.

Electromagnetic Enhancement

When the permittivity $\epsilon(\omega) = \epsilon_1(\omega) + i\epsilon_2(\omega)$ of a metal has a negative real component ϵ_1 and a small imaginary component ϵ_2, the metal is capable of of sustaining a surface plasmon resonance (SPR). This resonance is a coherent oscillation of the conduction electrons excited by electromagnetic radiation. In bulk silver this resonance is in the near ultra-violet region of the spectrum. For nanoparticles the plasmons are localized and the resonance is therefore referred to as localized surface plasmon resonance (LSPR). The excitation of LSPRs is essential for the electromagnetic contribution to the surface enhancement effect and is described in the following.

Different models have been employed meant to explain the electromagnetic enhancement effect (EEE). A model providing a good insight into the mechanisms of EEE describes the interaction of a single nanoscopic metal particle with the electromagnetic field of an incident laser beam and a molecule at a distance d from the particle's center (Figure 3.7). The radius of the nanoparticle is given by r. It is assumed that the radius r is much smaller than the wavelength λ_0 of the incident light (frequency ω_0). Therefore the electric field is considered homogeneous in the first approach. The frequency dependent permittivity of the sphere is given by $\epsilon(\omega)$. In general the particle is assumed to be smaller than 100nm in diameter. The particle together with the molecule are surrounded by a medium with the permittivity ϵ_m; in this case the frequency dependence is not essential for the model and is therefor disregarded.

When a metal sphere is placed in an oscillating electric field E_0 a dipole-moment p_{sp} is induced. It will be proportional to the electric field. The proportinal constant is the polarizability α_{sp} of the metal sphere.

$$p_{sp} = \alpha_{sp} \cdot E_0 \tag{3.13}$$

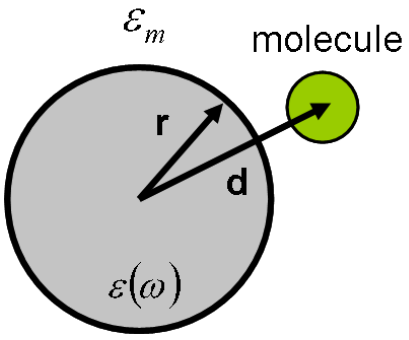

Figure 3.7: A molecule at a distance d from a metal nanoparticle with radius r. The relative permitivity of the particle and the surrounding medium is given by $\epsilon(\omega)$ and ϵ_m.

In the case of a sphere the polarizability is given by

$$\alpha_{sp} = 4\pi \cdot \epsilon_0 \cdot r^3 \cdot g_0 \tag{3.14}$$

where ϵ_0 denotes the permittivity of vacuum and

$$g_0 = \frac{\epsilon(\omega_0) - \epsilon_m}{\epsilon(\omega_0) + 2\epsilon_m}. \tag{3.15}$$

The induced dipole is oscillating together with the incident electric field E_0 and therefore emitting an electrical field E_{dip} described by

$$E_{dip} = \frac{p_{sp}}{4\pi\epsilon_0 d^3} = r^3 g_0 \frac{1}{d^3} E_0. \tag{3.16}$$

Hence, the total field experienced by the molecule is a superposition of the incident field E_0 and the field emitted by the dipole E_{dip}. The ratio of the total electric field and the incident electric field is the factor by which the field is enhanced:

$$\frac{E_{tot}}{E_0} = r^3 g_0 \frac{1}{d^3} + 1 \tag{3.17}$$

Considering the fact that Raman scattering is proportional to the intensity of the laser light and therefore proportional to the square of the electromagnetic field, the electromagnetic enhancement of the incident laser light

(A_L) is described by:

$$A_0 \propto g_0^2 \left(\frac{r}{d}\right)^6. \tag{3.18}$$

At the same time the light which is Raman scattered by the molecule is enhanced by the same mechanism. Enhancement of the Raman scatterd light (A_S) follows the proportionality

$$A_S \propto g_S^2 \left(\frac{r}{d}\right)^6, \tag{3.19}$$

where

$$g_0 = \frac{\epsilon(\omega_0) - \epsilon_m}{\epsilon(\omega_0) + 2\epsilon_m} \tag{3.20}$$

in accordance with Equation 3.15.Consequently the total electromagnetic enhancement factor EF_{EM} is given by the product

$$EF_{EM} = A_0 \cdot A_S \propto g_0^2 g_S^2 \left(\frac{r}{d}\right)^{12}. \tag{3.21}$$

Some important conclusions can be extracted from this relation.

- The enhancement is proportional to $\frac{1}{r^{12}}$, i.e. the enhanced electromagnetic field decays strong with the distance. Therefore it is important to have the molecule which is probed close to the surface.
- The enhancement factor can not be increased by using larger particles, due to the limitation to a maximum size of around 100 nm.
- The crucial parameters are g_0 and g_S. Both of them have a singularity in their denominator which is dependent on material constants. [2]

By choosing the right material $\epsilon(\omega_0) + 2\epsilon_m$ and $\epsilon(\omega_S) + 2\epsilon_m$ can be tuned to be close to zero and therefore lead to enormous enhancements, in some cases reaching 10^{10} or more [38]. The singularity coincides with the surface plasmon resonance condition. For silver in the near ultraviolet region, the resonance condition holds, while in the same region ϵ_2 is small ($\epsilon_m = 1.77$ for

[2]The permittivity is often referred to as a material constant, but in fact it is important to consider that ϵ is a function of the frequency $\Rightarrow \epsilon(\omega)$

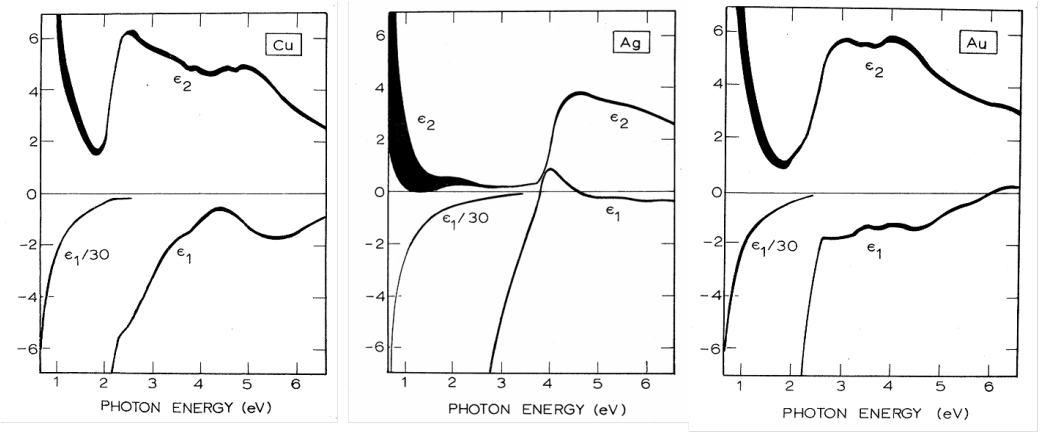

Figure 3.8: Real an imaginary part (ϵ_1 and ϵ_2) of the permittivities of copper, silver and gold, plotted as a function of photon energy. For silver resonance condition hold in the near ultraviolet region, while at the same time damping is low.

water, $\epsilon_1 = -3.54$ and $\epsilon_2 = 0.11$ at 382 nm for bulk Ag) [39]. The imaginary part ϵ_2 of the permittivity is often referred to as the quality factor, because this value is associated with damping of the plasmon resonance, where small values correspond to low damping. In general silver and copper are good enhancers in the blue to ultraviolet region, while gold is an efficient enhancer in the IR-region. The plot of the real and imaginary part of the material as a function of photon energy illustrates this finding (Figure 3.8).

The fundamental mechanism of electromagnetic enhancement is illustrated by this model, explaining why silver is commonly used as a SERS-activ substrate. However, shape-effects, and particle-particle interactions are not explained. In terms of rough surfaces these effects have to be taken into account. Still, the model of a single metal sphere is a good starting point to explain the mechanisms of surface enhancement on rough surfaces. In a first approximation a rough surface can be regarded as many truncated spheroids on a plane surface (Figure 3.9). Hence, the sphere model can be expanded phenomenologically to rough surfaces by including shape effects and interactions between the nanoscopic structures and the plane surface.

In order to explore the shape effect more closely, the extinction cross section for randomly oriented silver spheroids are shown in figure 3.10. The

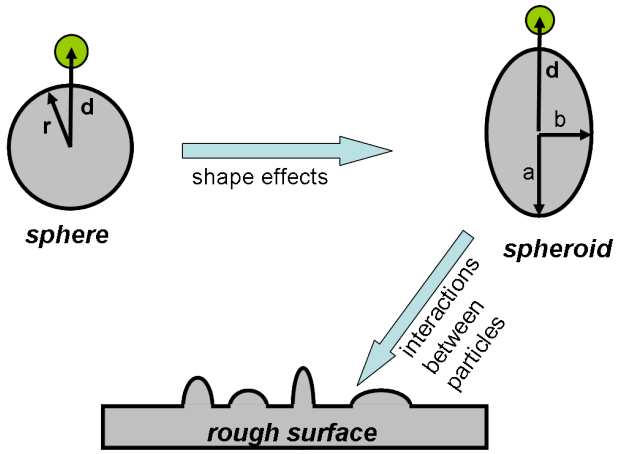

Figure 3.9: The sphere model can successively modified to describe rough surfaces by accounting for shape effects and particle-particle interactions.

central features are the two sharp extinction peaks for the spheroids and the single peak for the sphere. These peaks are due to excitation of the two dipolar plasmon resonances corresponding to the components of the electric field parallel to the axes of the spheroid. The peak at higher wavelength corresponds to the major axis, the one at lower wavelength to the minor axis [40]. Therefore, by changing the aspect ratios of nanoparticles the resonance frequency can be tuned.

Plotting the Raman enhancement of the same spheroids in the same frequency range illustrates an important characteristic of Equation 3.21. Due to the displaced singularities of g_0 and g_S two closely spaced peaks occur (Figure 3.11), whereas the separation of the two peaks peaks varies with the Raman shift. The peak at longer wavelength corresponds to the LSP resonance with the excitation wavelength of the laser ($\lambda_{0,1}$). The second peak at shorter wavelength corresponds to LSP resonance with the Raman scattered light ($\lambda_R = \lambda_{0,2} = \lambda_{0,1} + \Delta\lambda$). Of course, for both cases the LSP resonance frequency is the same. In one case the incident light is first enhanced and than Raman scattered, in the other case the incident light is first Raman scattered, and than enhanced.

Rough surfaces are considerably more complicated to describe and the enhancement is hard to predict. The LSPs of neighboring nanostructures may

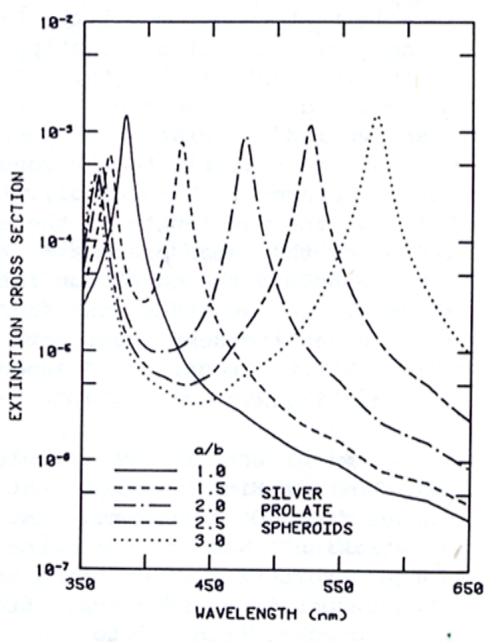

Figure 3.10: Spheroids exhibit LSP resonances at excitation wavelengths depending on their aspect ratio. LSP resonance along the minor axis remains unchanged, while the second resonance frequency due to electron oscillation along the major axis of the spheroid is observed at higher wavelength for higher aspect ratios.

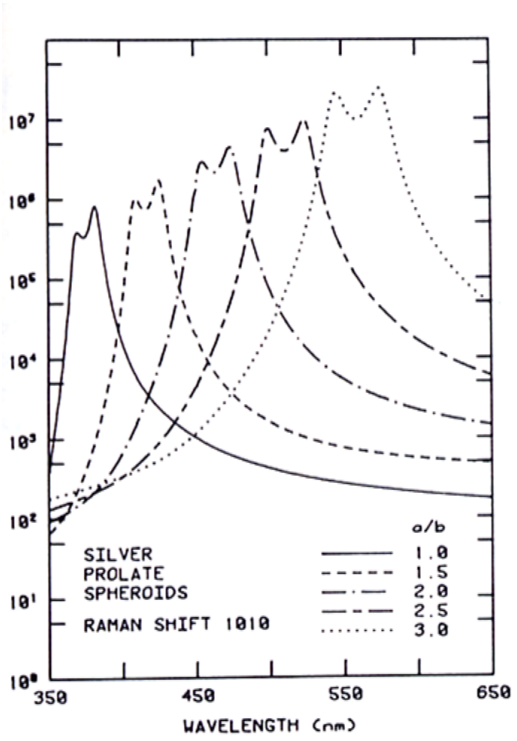

Figure 3.11: Raman scattering is enhanced if either the frequency of the incident laser light or the frequency of the Raman scattered light is in resonance with the LSP of the nanoparticles.

interfere with each other. This can lead to even higher field enhancements ("hot spots") but also to shifts in the resonance frequency of the coupled LSPs. In the case when the nanoparticles are neither spheres nor spheroids the shape can play a significant role. It is well known that at points with high surface curvatures highest enhancement is observed. This is explained with the fact the the streamlines of the electric field are perpendicular to the metal surface and therefore concentrate at those tips. Since this phenomenon is similar to the principle of a lightening rod it is often referred to as the lightening rod effect.

Chemical Enhancement

In addition the electromagnetic surface enhancement the spectra of Raman scattering molecules can be enhanced by a further mechanism, which is the chemical enhancement, also denoted as charge transfer (CT) effect. In contrast to electromagnetic enhancement, chemical enhancement is limited to molecules which are chemically adsorbed to the metal substrate. The charge transfer effect is more similar to the resonance Raman effect than to the electromagnetic surface enhancement. The nature of chemical enhancement is much more controversially discussed than the EEE. Several CT mechanisms are discussed in the literature [41–46], however, there is a mechanism described by Lombardi et al. [47] which is widely accepted.

The CT phenomena involves the transfer of an electron from the Fermi level of the metal to an unoccupied molecular orbital of the adsorbate or vice versa [47], as illustrated in figure 3.12. The evidence for this particular type of excitation has been mainly obtained from electrochemical experiments [42, 44]. When a molecule is adsorbed to a metal substrate laser excitation brings the possibility of transferring charges, electrons or holes, between the Fermi level of the metal and the lowest unoccupied molecular orbital (LUMO) or the highest occupied molecular orbital (HOMO) of the molecule. The CT transition from the HOMO to the Fermi level is illustrated in figure 3.12. For CT to take place the Fermi level must be between the HOMO and LUMO of the molecule, which is chemisorbed to the metal. The incident Raman

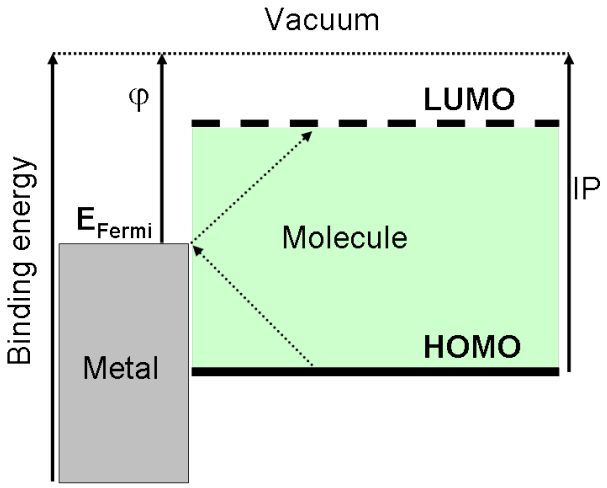

Figure 3.12: Illustration of the charge-transfer effect. Here IP is the ionization potential of the molecule and φ is the work function of the metal. Charge-transfer transitions between the Fermi level of the metal and the LUMO or HOMO of the molecule can appear. If the energy of the laser light is in resonance with one of this transitions a special case of resonance Raman scattering is created.

excitation laser light can be in resonance with one of the electronic transition, either metal to molecule or vice versa, creating a spacial case of resonance Raman scattering (Section 3.1.3).

3.2 Surface Plasmon Resonance Spectroscopy

Surface plasmon resonance spectroscopy (SPRS) is a method used to determine the thickness of thin layers or the the refractive index of those. The phenomenon of surface plasmons (SPs) can be derived from Maxwell's equations. However, SPs were first described by Ritchie [48] and the first SPRS measurements were published 1659 by Turbadar [49]. The excitation of SPs however, requires the use of specific configuration of exciting laser, the metal film and a coupling device. One can distinguish between the Otto [50] and the Kretschmann [51] configuration. The latter of both was used for the SPRS measurements presented in this dissertation.

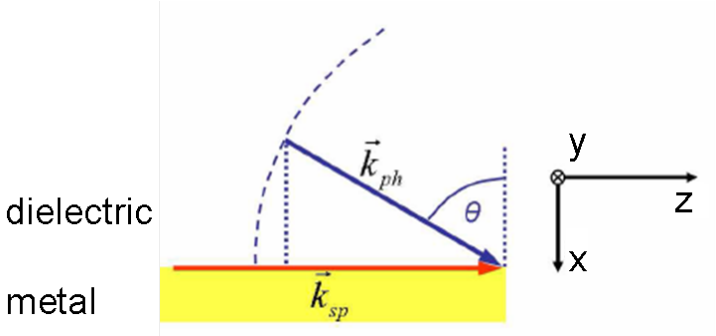

Figure 3.13: The surface plasmon is propagating along the dielectric-metal interface as illustrated by the wave vector k_{SP}. The incident photons are described by k_{ph}. The dielectric-metall interface lies in the y-z-plane.

3.2.1 Surface Plasmon Excitation

SPs can be regarded as collective oscillations of the free electron gas of a metal. They are excited by an incident electro-magnetic wave. SPs are longitudinal evanescent waves propagating along the metal-dielectric interface. Depending on the employed metal SPs are damped more or less strongly due to the dissipation of energy into the metal because of the conversion to heat [52].

The correlation between the wave vector k and the frequency ω of the electro-magnetic field is described by the dispersion relation:

$$\omega^2 = \frac{c^2 k^2}{n^2} \tag{3.22}$$

In this relation c is the speed of light and n is the refractive index of the medium. In general the refractive index is complex:

$$n = \sqrt{\epsilon} = n' + i \cdot n'' \tag{3.23}$$

Figure 3.13 illustrates the direction of incoming light and surface plasmon propagation. The wave vector of the incident light is described by k_{ph} while the wave vector of the surface plasmon is k_{sp}. The dielectric metal interface is in the y-z-plane. Hence, in order to match the resonance condition of the

SP the z-component of k_{ph} must coincide with k_{sp}. For that reason light polarized perpendicular to the plane of incidence (s-polarized) is not capable of exciting surface plasmons. Therefore, p-polarized light is used for SP excitation. In Figure 3.14 the dispersion relation of a photon in air, in a high refractive index prism together with the dispersion of a surface plasmon are shown. Depending on the angle of incidence θ (see Figure 3.13) the dispersion of the photon in air is represented by a straight line somewhere between the ω-axis and point A. The z-component of the photon $k_{Z,ph}$ never matches that of the surface plasmon $k_{Z,sp}$. Using a prism as a coupling device leads to an increased $k_{Z,ph}$, coinciding with $_{Z,sp}$ in point C. However point C is not in line with the laser frequency ω_L used for excitation. Varying the angle θ finally leads to the case where $k_{Z,ph}$, $k_{Z,sp}$ and ω_L (point B), which is the case of surface plasmon excitation [53]. The evanescent character of the SP is illustrated in Figure 3.15. The SP is excited at the dielectric-metal interface (y-z-plane) and propagates along the z-direction. The principle of prism coupling is shown in Figure 3.16. The thickness of the metal film is usually in the range between 40 and 50 nm so as to achieve that the evanescent field of the SP extends into the dielectric medium.

3.2.2 Detecting Adsorption by SPRS

In SPRS the angle dependent intensity reflected from the metal-dielectric interface (I_R) is measured. At the angle of total reflaction (θ_{TR}) I_R reaches a maximum, while at the angle of SP resonance (θ_{SPR}) the reflected intensity decreases to a minimum. The angle θ_{SPR} depends on the refractive index of the metal and the dielectric. Adsorption of any kind of material leads to a change in refractive index at the metal-dielectric interface, which causes a shift of θ_{SPR} and therefor a change in $I_R(\theta)$. A typical angular scan is depicted in Figure 3.17. After reaching θ_{TR} the reflectivity, which is defined as

$$R = \frac{I_R}{I_0}, \tag{3.24}$$

reaches $R = 1$. Here I_0 denotes the intensity of the incident light. The dip in reflectivity at higher angles corresponds to SPR. At $\theta = \theta_{SPR}$ the reflectivity

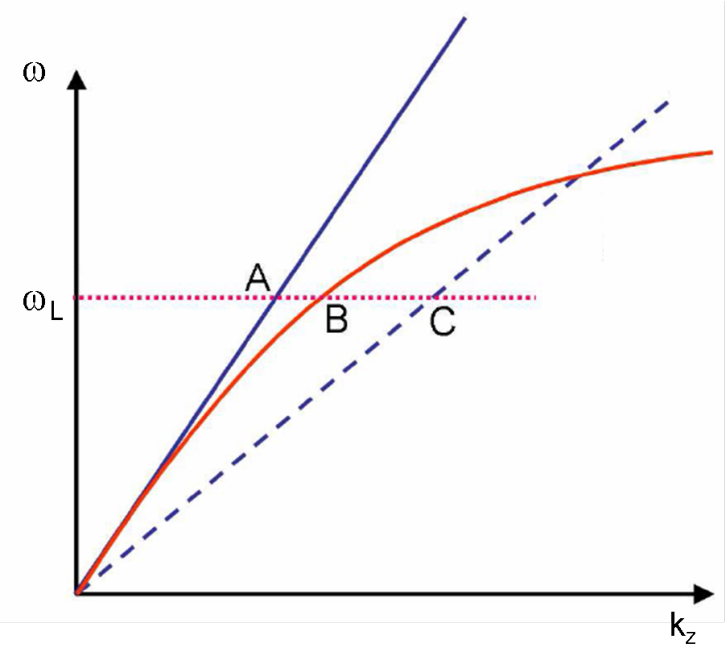

Figure 3.14: Dispersion relation of a photon in air (solid blue), in a high refractive index prism (dashed blue) compared to the dispersion relation of a surfcae plasmon(red). Depending on the angle of incidence θ (see Figure 3.13) the dispersion of the photon in air is represented by a straight line somewhere between the ω-axis and point A. The z-component of the photon $k_{Z,ph}$ never matches that of the surface plasmon $k_{Z,sp}$. Using a prism as a coupling device leads to an increased $k_{Z,ph}$, coinciding with $_{Z,sp}$ in point C. However point C is not in line with the laser frequency ω_L used for excitation. Varying the angle θ finally leads to the case where $k_{Z,ph}$, $k_{Z,sp}$ and ω_L (point B), which is the case of surface plasmon excitation.

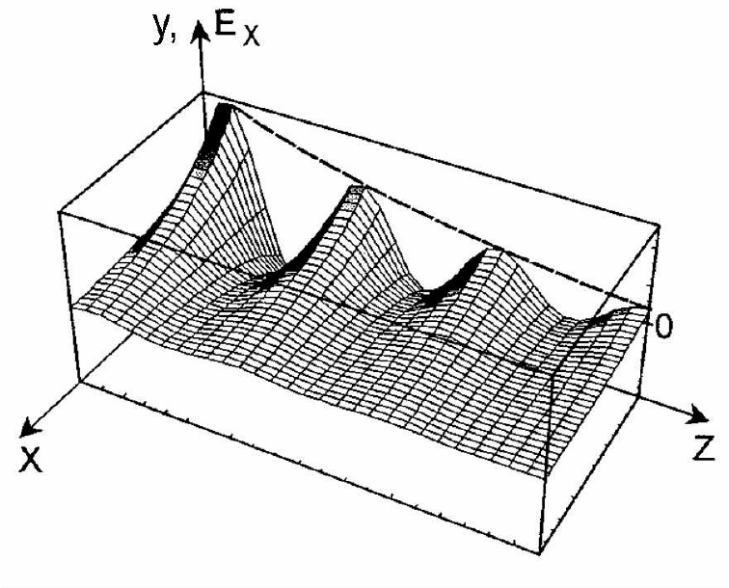

Figure 3.15: Evenscent character of a SP at a dielectric-metal interface (y-z-plane). The electric fiel component decays exponentially in x-direction. [53]

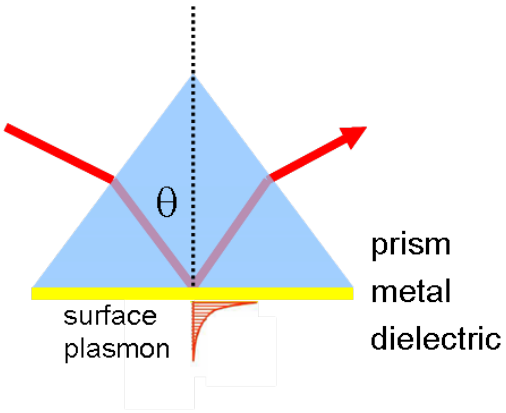

Figure 3.16: Beam path of the laser light used for surface plasmon resonance excitation. In this case a prism is used as coupling device. The exponential decay of the evanescent field is indicated by the red curve.

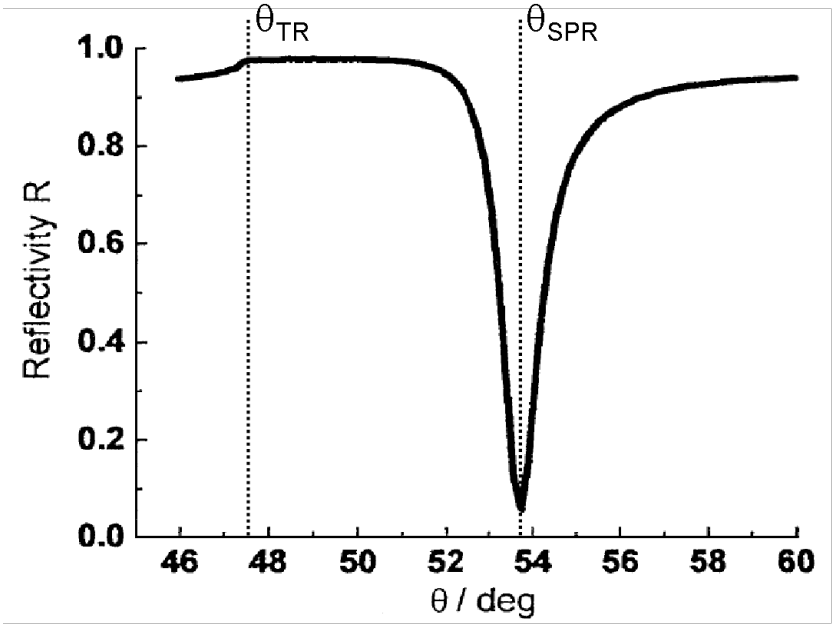

Figure 3.17: Surface plasmon excitation curve. The Reflectivity is plotted as a function of the angle θ. $R \approx 1$ at $\theta = \theta_{TR}$ and $R \approx 0$ at $\theta = \theta_{SPR}$

ideally decreases to zero. Hence, adsorption at the surface is detected by a change in θ_{SPR} due to a change in the refractive index at the metal-dielectric interface.

The interested reader is referred to the review written by Wolfgang Knoll [53] and the *Handbook of Surface Plasmon Resonance* [54]. More experimental details are described elsewhere [55].

3.3 Electrochemistry

Basically two different electrochemical methods have been employed. Electrochemical impedance spectroscopy (EIS) and cyclic voltammetry (CV). EIS used to monitor the formation of the ptBLM and to characterize the biomimetic system after formation. CV proved to be useful when investigating the redox behavior of heme proteins. Furthermore this method was capable of testing the catalytic activity of CcO in the ptBLM.

3.3.1 Electrochemical Impedance Spectroscopy (EIS)

EIS is a method commonly used to probe the electrical properties of various materials. For example the quality of coatings as well as the properties of semi conductors can be studied. In this work EIS was used to characterize the artificial membrane system ptBLM and in particular to monitor the progress of the different preparation steps, such as protein binding and membrane reconstitution. In EIS an alternating electrical potential is applied to the sample, while the current and phase shift is measured as the response of the sample. This is repeated for a large number of frequencies. The impedance is the complex resistance of the system combining ohmic, capacitive, inductive resistances. The system is exited with a sinusoidal electric potential

$$E(t) = E_0 \cdot \sin(\omega t), \tag{3.25}$$

where E_0 is the amplitude and usually between 5 and 10 mV. The potential E is applied between working electrode (WE) and the reference electrode (RE). A third electrode is used as a counter electrode (CE) to measure the current. The resulting current with the amplitude I_0 is shifted by the phase Φ and alternates with the same frequency as the exciting potential:

$$I = I_0 \cdot \sin(\omega t + \Phi). \tag{3.26}$$

Consequently the impedance is given by

$$Z(t) = \frac{E(t)}{I(t)} = \frac{E_0 \cdot \sin(\omega t)}{I_0 \cdot \sin(\omega t + \Phi)} = Z_0 \cdot \frac{\sin(\omega t)}{\sin(\omega t + \Phi)}. \tag{3.27}$$

According to Eulers relation

$$e^{i\varphi} = \cos\varphi + i \sin\varphi \tag{3.28}$$

the potential E, the current I and the impedance Z can be expressed as

$$E(t) = E_0 \cdot e^{i\omega t} \tag{3.29}$$

$$I(t) = I_0 \cdot e^{i(\omega t - \Phi)} \tag{3.30}$$

$$Z = \frac{E(t)}{I(t)} = \frac{E_0 \cdot e^{i\omega t}}{I_0 \cdot e^{i(\omega t - \Phi)}} = \frac{E_0}{I_0} \cdot e^{i\Phi} = |Z| \cdot e^{i\Phi} = Z' + iZ''. \tag{3.31}$$

The phase shift or phase angle is given by

$$\Phi = \arctan\left(\frac{Z''}{Z'}\right). \tag{3.32}$$

A further important parameter is the admittance Y, which is the reciprocal value of the impedance. Hence, the admittance corresponds to the complex conductivity and is given by

$$Y = Y' + iY'' = \frac{1}{Z} \tag{3.33}$$

with

$$Y' = \frac{Z'}{(Z')^2 + (Z'')^2} \tag{3.34}$$

and

$$Y'' = -\frac{iZ''}{(Z')^2 + (Z'')^2}. \tag{3.35}$$

Two different diagrams have been used in this work to display the results of EIS measurements. The Bode-plot shows the absolute value of the impedance and the phase Φ as a function of the frequency ω. The frequency reduced admittance-plot shows Y''/ω as a function of Y'/ω. In order to characterize a sample the resulting data can be fitted to an equivalent circuit. However, some fundamental properties can be derived from the graphs without using a fitting routine.

Capacitor

The impedance of a capacitor with the capacity C is given by

$$Z_C = -\frac{i}{\omega C}. \tag{3.36}$$

Therefore $Z'_C = 0$ and $Z''_C = -\frac{1}{\omega C}$ The phase angle calculates as $\Phi_C = \arctan(\frac{Z''_C}{Z'_C}) = -90°$. Obviously the impedance of a capacitor is dominant for small frequencies. According to Equations 3.34 and 3.35 $Y'_C = 0$ and $Y''_C = -\omega C$.

Ohmic Resistor

The impedance of an ohmic resistor is given by

$$Z_R = \frac{E}{I} = R. \tag{3.37}$$

Hence, $Z'_R = R$, $Z''_R = 0$ and $\Phi_R = 0$. In accordance with Equations 3.34 and 3.35 $Y'_R = \frac{1}{R}$ and $Y''_C = 0$.

3.3.2 Cyclic Voltammetry (CV)

CV is an analytical method where a voltage-current characteristic is recorded. A cyclic voltammogram provides information about the thermodynamics of redox processes and gives insight into the kinetics of herterogenous electron transfer reactions.

In a CV experiment a linearly changing potential is applied between the working electrode (WE) and the reference electrode (RE). Initially the potential E_i is applied. The potential is than changed (increased) with a certain scan rate $\nu = \frac{dE}{dt}$ until the first vertex potential E_{V1} is reached. The potential is than changed (decreased) until the second vertex potential E_{V2} is reached and then linearly changed until E_i is reached again. Often the cycle is repeated several times. A characteristic potential-time-curve is depicted in Figure 3.18. The vertex potentials are chosen so as to enclose the redox potentials of the sample.

Two different kinds of currents can be distinguished. Charge transfer reactions between the working electrode and the redox species are called Faradaic currents, while currents which are not associated with redox transitions are termed non-Faradaic currents.

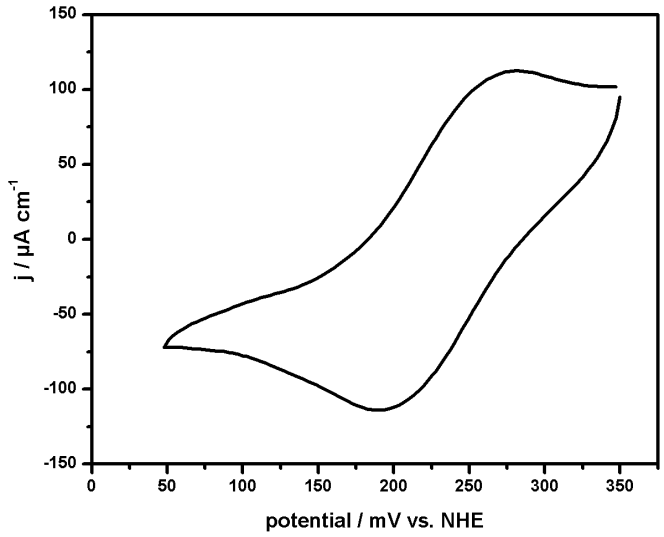

Figure 3.18: Cyclic voltammogram of cytochrome c adsorbed on a SAM of mercaptoethanol.

Non-Faradaic Currents

Non-Faradayic currrents result from the reorganization of ions in the electrolyte close to the electrode interface. They are of electrostatic nature and are associated with charge separation due to the applied potential. Therefore they are also referred to as capacitive currents. In CV the potential characteristic is described by

$$E_{app} = E_i + \nu \cdot t \tag{3.38}$$

where E_{app} is the applied potential, E_i is the initial potential, ν the scan rate and t the time. If the interface capacity is C, the resistance of the solution is R_S, then the capacitive current I_C is described by [56]

$$I_C(t) = \frac{E_i}{R_S} \cdot e^{-\frac{t}{C \cdot R_S}} + \nu \cdot \ C \cdot \left(1 - e^{-\frac{t}{C \cdot R_S}}\right). \tag{3.39}$$

Therefore I_C is determined by the capacity C and the scan rate ν. After decay of the transient current a constant current $\Delta I = \nu \cdot C$ remains.

Faradayic Currents

Heterogenous electron transfer between the WE and the redox species leads to so-called faradayic currents. Therefore, the Faradayic current is alway accompanied by a turnover from reduced to the oxidized species or vice versa. Depending on the electrode potential the reduced Species R is oxidized or the oxidized species O is reduced:

$$O + e^- \rightleftharpoons R \tag{3.40}$$

Heterogenous electron transfer at the electrode interface depend on the electrode potential E, the standard potential of the redox species E_0. The resulting current is described by the Butler-Volmer-Equation:

$$I = FAk^0 \left[C_O(0,t) \cdot e^{-\alpha \frac{nF}{RT}(E-E_0)} - C_R(0,t) \cdot e^{(1-\alpha)\frac{nF}{RT}(E-E_0)} \right] \tag{3.41}$$

F is the Faraday constant, A the electrode area, k^0 the standard rate constant, α is the transfer coefficient, R the gas constant, T the temperature, $C_O(0,t)$ and $C_R(0,t)$ are the concentrations of the oxidized and reduced species at the surface ($x = 0$) at the time t. The standard potential E_0 characterizes the point at which under thermodynamical equilibrium the concentration of reduced and oxidized species is balanced.

In equilibrium the resulting current is $I = 0$. If all steps involved in the redox mechanism are facile, so that exchange velocities of all steps are fast compared to the net reaction rate the concentrations of all species participating in them are always essentially at equilibrium, even though a net current flows [56]. In this case Equation 3.41 reduces to

$$E = E_0 + \frac{RT}{nF} \cdot \ln\left(\frac{C_0}{C_R}\right), \tag{3.42}$$

which is known as the Nernst equation. Obviously the concentration of the reduced and oxidized species is then defined by the electrode potential E only.

Chapter 4

Materials and Methods

4.1 Sample Preparation Procedures

The following preparation procedures were followed strictly in order to guarantee reproducibility. The methods described were applied independently of the kind of measurement. Thus, samples prepared for SERRS, AFM, SEM, etc. were obtained from exactly the same procedures if not stated differently.

4.1.1 Template Stripped Gold - TSG

Ultra flat and thin gold surfaces were used for surface plasmon resonance (SPR) spectroscopy. The thickness of the gold layers were chosen 50 nm in order to obtain best SPR conditions. The surface roughness (rms) obtained from the method described below was in the range of 1nm. Template stripped gold surfaces are an ideal substrate for supported bilayer lipid membranes as reported by Naumann et al. [57].

Silicon wavers were used as a template. Prior to use the silicon slides were cleaned by immersing in a mixture of H_2O, NH_3 and H_2O_2 (ratio 5:1:1) at a temperature of 70 °C. After slowly cooling down the slides were thoroughly rinsed with water and ethanol before they were stored in ethanol to prevent recontamination.

Starting from this point further preparation was proceeded in a clean room. After drying the slides with argon or nitrogen gold was deposited

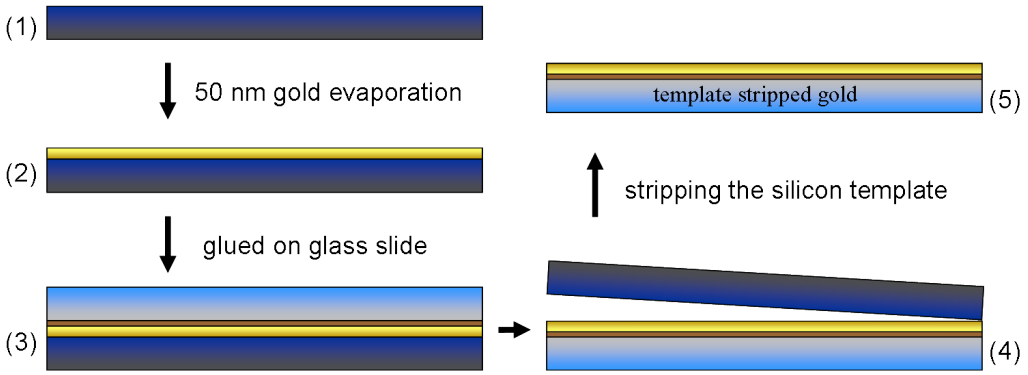

Figure 4.1: Preparation steps of Template Stripped Gold / Silver. Cleaned silcon wavers (1) were used as template. 50 nm gold or 45 nm silver were evaporated (2). Glass slides were glued to the gold or silver layer using a special optical glue curing at 150 °C (3). Right befor use the silcon template was stripped (4) and the ultra flat metal layer was ready for functionalisation (5).

by evaporation. Uniform deposition was guarantied by a rotating sample holder. Evaporation was initiated after the ambient pressure was reduced below $p_{amb} \leq 10^{-4}$Pa by heating gold grains using a resistor. The evaporation rate was kept constant below 0.1 nm/s. Subsequently the slides were kept in ethanol.

Glass slides were cleaned from dust particles by rinsing with water. Further the slides were treated with a 5% aqueous Hellmanex solution in an ultra sonic bath for 15 min followed by thoroughly rinsing with MilliQ water and drying with nitrogen. The glass slides were glued on top of the gold layer by a special optical glue (EPO-TEK 353ND-4) by means of a specially designed press. The refractive index of the glue was $n_{glue} = 1.5922$ at the used wavelength $\lambda_{laser} = 633$ nm. Prior to use the glue was evacuated at $p \leq 10^{-1}$ Pa to prevent micro defects in the glue layer. The glue was cured at 150 °C for 90 min. Since the gold layer was enclosed by the silicon slide on one side and the glue on the other side it was stable for several months.

Right before being used the template was stripped and the ultra flat, thin metal layer was functionalized. The progression of preparation is demonstrated in figure 4.1.

4.1.2 Template Stripped Silver - TSS

Template stripped silver (TSS) was prepared by the same procedure described for TSG in section 4.1.1. Instead of gold grains silver grains were used. The thickness of the evaporated silver was 45 nm in this case. All other conditions were exactly the same as in the case of TSG.

4.1.3 SERRS Substrates

As a substrate for all Raman measurements massive silver rods were chosen. They measured 10 mm in diameter and 1–1.6 mm in height. Different strategies have been followed for modifying the surface morphology in a way to make them capable of being used for SER(R)S (see section 3.1.4). Prior to these nano-stucturing procedures the top planes of silver rods were polished according to the following procedure in order to achieve a smooth basis for further treatment.

The planes of silver rods were used as SERRS substrates and/or electrodes. They were polished prior to use with a polishing machine (Buehler PHOENIX 4000) using a synthetic polishing cloth (ChemoMet, Buehler). The electrodes were successively polished with alumina (Al_2O_3) slurries with a grain size 1 (MicroPolish II (C) alpha, Buehler), 0.3 (MicroPolish II (A) alpha, Buehler), and 0.05 µm (MicroPolish II (B) gamma, Buehler), in that order. Each polishing step was performed for 3 min at 300 rpm. After each step, the electrodes were extensively rinsed with MilliQ-water and cleaned in an ultrasonic bath in order to prevent contamination with alumina particles. The rms roughness finally achieved was in the range of 3–5 nm.

Electrochemically Roughened Silver Electrodes

The electrodes were electrochemically roughened by applying oxidation-reduction pulses provided by a potentiostat (Autolab, PGSTAT302, Eco Chemie, B.V. Utrecht, Netherlands). This treatment was performed in 0.1 M KCl solution changing the potential between +500 and −100 mV and holding it for 70, 20, 15, 10, and 5 s, respectively. The rms roughness of

the electrochemically roughened silver electrodes was determined by atomic force microscopy using a Dimension3100 (Veeco Instruments Inc.). An area of $5\,\mu m \cdot 5\,\mu m$ was scanned in the tapping mode, and the rms roughness was calculated from these data. The rms roughness finally obtained was 90 nm.

Fabrication of Silver Nanoparticles

The following method was developed by C. Nowak [58].

Silver nanoparticles (AgNPs) were synthesized according to a modified version of the method of Turkevich [59] and Frens [60], who introduced citric acid as a reducing agent. 8.25 mL of 37 % formaldehyde was added to 250mL of an aqueous AgNO3 solution (10mmol/L). The mixture was heated during vigorous stirring to 100 °C for at least 15 min. Further 4 mL of an aqueous solution of citric acid (33 mmol/L) was added. The temperature was kept constant at 100 °C until the color changed in the first minutes to a bright yellow, eventually changing into a darker greenish-yellow, indicating a suspension of AgNPs. Dynamic light scattering (DLS) revealed a highly monodisperse solution of spherical NPs of an average diameter of 39 nm.

Ag Nanoparticle Modified Silver Electrodes

The development of the method was part of this dissertation. The procedure given in the following decribes the conditions found to be ideal. The development together with a detailed characterization of the achived surface morphology are described separately in section 5.3 and reference [58].

The top planes of silver rods were functionalized by self-assembled monolayers (SAMs) of cysteamnine (CA). SAMs were formed by immersion of the silver rods into an aqueous solution of CA (10 mmol/L) for 1 h. After thorough rinsing with water the functionalized silver rods were immersed into the nanoparticle suspension for 2 h. The silver rods were then rinsed with water again before further treatment.

4.1.4 Preparation of Cytochrome c Samples for SERRS

Rough (electrochemically roughened or AgNP modified) silver electrodes were immersed for 30 min into an aqueous solution of ME (1 mmol/L). The excess of ME was removed by rinsing with water. Cc was adsorbed on the SAM of ME by immersing the functionalized silver electrode into PBS buffer (20 mmol/L K_2HPO_4, 100 mmol/L $NaClO_4$, pH = 7) containing 50 µmol/L cc for at least 30 min.

4.1.5 Protein Tethered Bilayer Lipid Membrane (pt-BLM)

CcO from Rhodobacter sphaeroides was expressed and purified by Hiser and Ferguson-Miller [61]. Immobilization of CcO was performed as previously described [62]. Briefly, the AgNP modified silver electrodes were functionalized with dithiobis-(nitriloacetic acid butylamidylpropionate) (DTNTA). For that purpose (DTNTA) and dithiobis (propionic acid) (DTP) were dissolved in dry DMSO at a molar ratio of 0.1 to 0.9 to a total concentration of 5mmol/L. The silver electrodes were immersed in this solution for 24h. After rinsing with dry DMSO and drying in a stream of nitrogen, the electrodes were immersed for 30 min in a 40 mmol/L $NiSO_4$ solution in acetate buffer (50 mmol/L, pH=5.5) so as to use Ni as the coordinating ion. The excess Ni was washed off with deionized water. The Ag surface thus prepared was exposed to a solution of CcO in dodecyl β-D-maltoside (DDM) phosphate buffer (K_2HPO_4 50 mmol/L, KCl 100 mmol/L, pH = 8, 0.1 % w/v DDM), leading to an oriented adsorption of the protein. After an adsorption time of 2 h the protein excess was removed by rinsing with DDM buffer solution. Reconstitution was initiated by replacing the DDM buffer solution with a diphytanoylphosphatidylcholine (DiPhyPC) solution (40 µmol/L) in DDM-phosphate buffer together with biobeads (Bio-Rad Laboratories GmbH, Munich, Germany). After 24 h the membrane formation was completed and the electrodes were rinsed with PBS.

4.2 Electrochemistry

Electrochemical Impedance Spectroscopy (EIS) and Cyclic Voltammetry (CV) were performed using a potentiostat (Autolab, PGSTAT302, Eco Chemie, B.V. Utrecht, Netherlands). Ag/AgCl in KCl_{sat} was used as a reference electrode (RE), a platinum wire as a counter electrode (CE), while TSS or the silver rods made for SERRS experiments were used as working electrodes (WEs). If not stated differently EIS measurements were done in a frequency range from 100 kHz to 1 mHz with an amplitude of 10 mV.

4.2.1 Setup

EIS and CV measurements were performed using the measuring cell designed for SERRS experiments or the measuring cell designed for SPR spectroscopic experiments. Therefore EIS and CV could be combined either with SERRS or SPR spectroscopy. The corresponding measuring cells are described in section 5.1 and 4.3.1, respectively.

4.3 Surface Plasmon Resonance Spectroscopy

Surface plasmon resonance measurements were performed using a homebuilt SPR setup allowing for simultaneous EIS and CV measurements as described before [63]. Biefly, a HeNe laser ($\lambda_0 = 632.8\,nm$) was used for the excitation of surface plasmons in the Kretschmann configuration. The prism used as a coupling device was made from LaSFN9 ($n_{prism} = 1.84$). SPR measurements were performed using TSS or TSG slides.

4.3.1 Setup

A schematic illustration of the setup is depicted in Figure 4.2. The beam of the HeNe laser was modulated using a mechanical chopper. The beam was guided through two polarizers utilized to obtain p-polarized laser light for SP excitation and to adjust the laser power at the sample. Subsequently the laser beam was coupled into the prism, which was pressed to the glass side

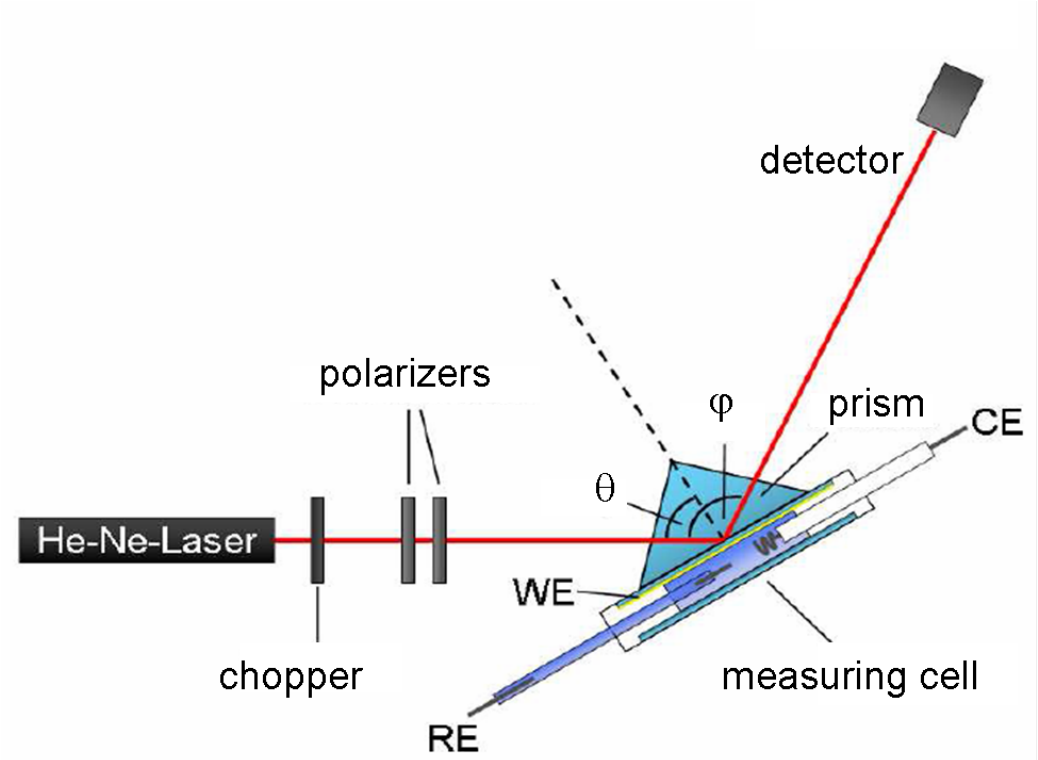

Figure 4.2: Schematic illustration of the SPR spectroscopy setup. For SPR excitation a HeNe laser was used. The beam path was guided through two polarizers before coupling into the prism and reaching the sample. The reflected light was guided to a photo detector. By using goniometers the angle of incidence was scanned. The angles of sample and detector were related by $\varphi = 2 \cdot \theta$. [64]

of either a TSS or a TSG slide. Index matching oil was used to connect the prism to the glass. The laser beam was reflected at the gold layer and further guided into a photo-detector. The measuring cell used for SPR measurements was made from teflon (Figure 4.3). Into the cell body a cylindric pocket used as liquid reservoir was machined (1). On one side the pocket was sealed with a glass slide by using a gasket ring. On the other side the TSS or TSG was mounted with the metal layer directed towards the pocket. Furthermore an inlet for the counter electrode (2) and the reference electrode (3) were placed at the top edges. A sample holder was used to press the prism to the TSS or TSG slide (Figure 4.4). Thereby the the liquid reservoir was sealed by the

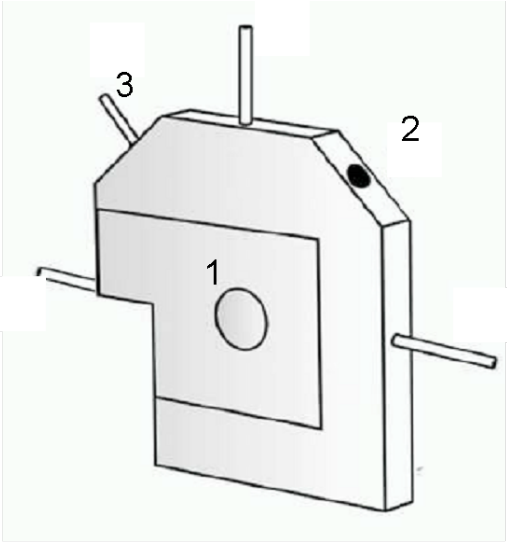

Figure 4.3: The SPR measuring cell. The cell was made from teflon to ease cleaning. A cylindric pocket in the center was used as a liquid reservoir (1). Inlets for the CE (2) and the RE (3) were placed at the top edges. A TSS or TSG slide sealing the liquid reservoir at one side was used as the WE. The other side was sealed by a glass slide. (The TSS/TSG and the glass slide are not depicted. [65]

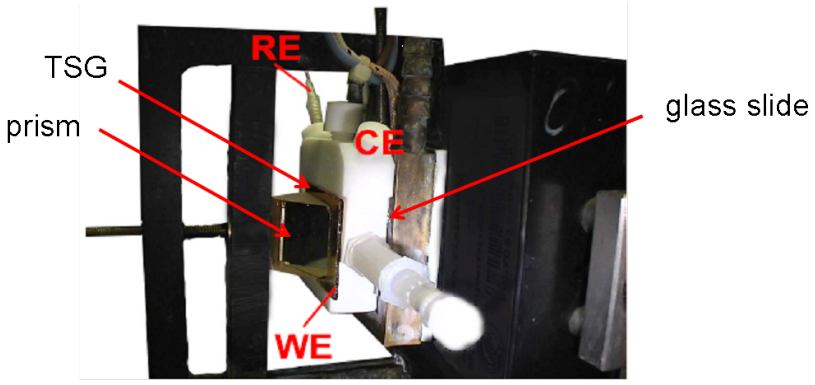

Figure 4.4: A sample holder was used to connect the glass slide, the teflon cell, the TSS/TSG slide and the prism by mechanical pressure. [64]

glass slide and the TSG/TSS slide. The sample holder and the detector were mounted onto goniometers so as to change the angle of laser incidence. The corresponding angles were related by $\varphi = 2 \cdot \theta$. The diameter of the cylindric pocket was 1 cm and the resulting surface area was 0.785 cm^2.

4.4 Spectroelectrochemistry

4.4.1 Setup

The setup used to perform SERRS measurements (Figure 4.5) was mounted onto a shock absorbing optical table (Newport Corporation). Surfaceenhanced resonance Raman (SERR) spectra were acquired using a high resolution confocal Raman microscope (LabRam, HR800, HORIBA Jobin Yvon) equipped with a liquid nitrogen-cooled back-illuminated charge-coupled device (CCD) detector (Symphony, Jobin Yvon) optimized for near-ultraviolet light. The 413 nm emission line of a Kr^+ laser (Innova 90C, Coherent) was used for excitation. The laser beam was first directed through a premonochromator (LaserspecIII, Spectrolab Research Laboratory, Newbury, England) in order to remove background radiation consisting of plasma lines produced by the laser medium.

The optical beam path was further guided by a series of adjustable mirrors through an acousto-optic modulator (AOM) (A.A. MT200/ A0,5 @ 400 nm

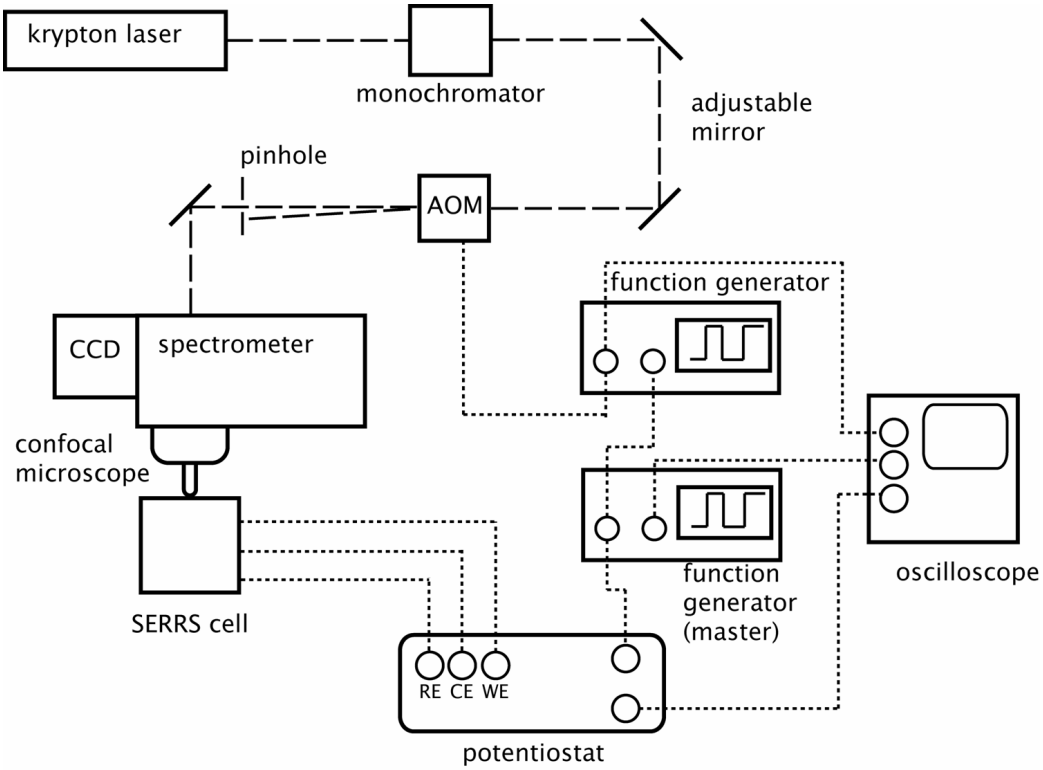

Figure 4.5: The SERRS setup is based on a confocal Raman microscope combined with a newly designed SERRS cell. Excitation is achieved by a Kr^+ laser. An AOM allows blocking of the laser beam intermittently and therefore generating short laser pulses in the ms range.

01/24091, A.A. opto-electronique, St. Remy, France) and finally coupled into the confocal microscope (BX41, Olympus). The laser beam was focused onto the protein sample, by a long-distance water immersion objective (Olympus LUMPLFL, 100 XW, WD = 1.5, NA = 1, BFOBJ) optimized for transmission of near UV light. The scattered light was then collected by the same objective and guided through a notch filter (413 nm) designed to filter out Rayleigh scattered light. The Raman scattered light was then focused onto the confocal pinhole of the microscope providing spatial resolution. Spectral resolution was achieved by an 1800 grooves/mm grating. The spectrum was imaged onto the CCD detector with an area of 2048 x 512 pixels. The focal length of the spectrograph was 800 mm. Thereby a spectral resolution of $3\,cm^{-1}$ was achieved. The increment per data point was $0.4\,cm^{-1}$.
A software controlled (Gpes, Autolab) potentiostat (Autolab, PGSTAT302, Eco Chemie, B.V., Utrecht, Netherlands) was used for modulation of the potential applied to the protein.

4.4.2 Time-Resolved Measurements

Time-resolved measurements were realized by periodic electrochemical excitation of the protein combined with synchronized illumination of the sample by short laser pulses in the ms range. For this purpose the laser beam was subsequently passing an AOM.

The AOM was mounted on a stage allowing free movement in x-, y-, z-directions and adjustment of the angular position in order to efficiently couple the laser beam onto the quartz crystal to achieve an optimum of light intensity. The AOM was controlled by a function generator (33250A 80 MHz, Agilent), which routed the exciting laser light onto the sample or blocked the beam, respectively.

In time-resolved measurements a master signal provided by a function generator (20 MHz 8021, Tabor Electronics) was used to trigger the periodic step potential of the potentiostat as well as the function generator controlling the AOM. The triggering process was screened by an oscilloscope (9354AM, LeCroy), and a synchronized electrochemical and optical excitation of the

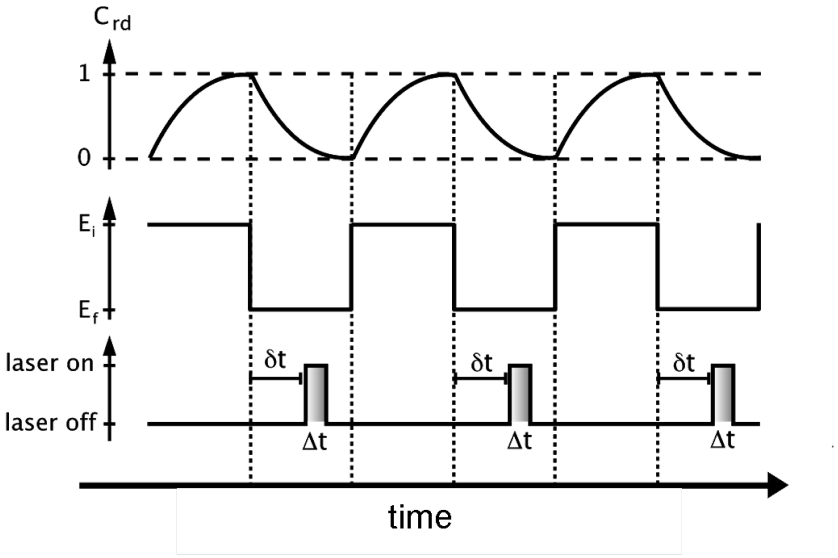

Figure 4.6: Principle of TR-SERRS measurements. TR spectra were obtained by excitation with short laser pulses, which were synchronized with the electrochemical excitation of the protein sample.

protein was achieved (Figure 4.6).

4.5 Other methods

Methods used to characterize samples or used to follow the progress of preparation steps but were not fundamental part of the dissertation are describes below.

4.5.1 Dynamic Light Scattering

Dynamic light scattering (DLS) was performed with a setup from ALV (ALV-Laser Vertriebsgesellschaft mbH, Langen, Germany). It consists of a HeNe laser as the light source, a goniometer (ALV-Laser Vertriebsgesellschaft mbH, Langen, Germany) to control the detector angle, and a fiberoptic detector to measure the intensity of the scattered light. The width of the laser beam was reduced to 1 mm by using a two-lens system. The size distribution of the AgNPs was obtained from intensity time correlation functions obtained

from the homodyne detected scattered intensity using an ALV 5000 hardware correlator. The AgNP suspension obtained from the procedure described above was diluted at a ratio of 1:10. Dust particles were removed from the suspension by filtration with Millipore filters; pore size 0.45 µm. Cylindrical Suprasil light scattering cuvettes of 10 mm diameter were used. The cuvettes were kept in a temperature-controlled toluene bath to avoid diffraction from the glass walls.

4.5.2 Scanning Electron Microscopy

Scanning electron microscopy (SEM) images were taken using a SEM instrument (1530 Gemini, Leo/ Carl Zeiss SMT - Nano Technology Systems). Some images were recorded showing exaggerated contrast in order to allow for automated particle counting.

4.5.3 Atomic Force Microscopy

Atomic force microscopy (AFM) was performed using a Dimension 3100 Scanning Probe Microscope (Veeco Instruments), which was set up in a special acoustically sealed chamber in order to reduce ambient noise. Samples were scanned in the tapping mode. One line per second was scanned with a resolution between 256 and 512 points per line.

Chapter 5

Results and Discussion

5.1 A Novel Measuring Cell Design for SERRS Applications

5.1.1 Introduction

Photodegradation of the protein by the incident laser beam is a serious problem in near UV Raman scattering [66]. In order to overcome this problem, a number of setups were designed to reduce the exposure time of the active area to the laser beam. This was achieved by using either a rotating Ag ring electrode [67], a linearly moving Ag disk electrode [68, 69], or a rotating disk electrode (RDE) [20, 70]. The latter solution seemed the most promising, particularly as far as the RDE was mounted upside down so that the laser beam could be focused onto the surface from above. A setup using this principle was described only once and not in great detail. Later on these authors returned to their earlier design of the rotating Ag ring electrode [71, 72]. The reason might be that some other details of the cell design were not solved properly, for example, the sealing of the fluid-containing cell body versus the rotating shaft of the electrode. Another problem is the electric contact to the rotating electrode. In the following a new measuring cell is presented taking these problems into account. The power of the laser beam can thus be reduced to 100 μW or even lower compared to the rotating ring and lin-

early moving disk, which use 5 [69] or 60 mW [67], respectively. The new setup was then used to perform time-resolved (TR) SERRS measurements on cytochrome c (cc).

5.1.2 Results

A custom-made measuring cell was designed for spectro-electrochemistry using SERRS (Figure 5.1). It is based on a rotating disk electrode (RDE), turned upside down for illumination by means of a confocal Raman microscope. To prevent photodegradation of the protein, the RDE was mounted on top of a rotating axis, which was belt-driven. A constant speed of 800 rpm is achieved using a DC-motor (FAULHABER 3863H012C 38A 1:5). In order for the surface of the electrode to stay exactly in the focal plane of the confocal microscope at all times, it had to be machined very precisely (deviation $< 10\,\mu$m). Moreover, the 10mm drive shaft was inserted in the cell body by two high precision ball bearings (GRW Gebr. Reinfurt GmbH and Co. KG, Würzburg). The cell body was made from polymethyl methacrylate (PMMA). The drive shaft was constructed from a stainless steel rod to provide mechanical rigidity. A conductive bolt was inserted into the drive shaft insulated by an epoxy casting resin (3430 Aand B Hysol, Loctite). A cross-section of the drive shaft is depicted in figure 5.2. The silver electrode was mounted on top of the conductive bolt by a thread, while the lower end was connected to the agile part of a mercury contact (custom-made, provided by Eco Chemie, B.V., Utrecht, Netherlands). Sealing the silver electrode, inserted into the aqueous buffer solution, against the cell body was achieved by a special axial face sealing (Hatech GLRD HT 921, technico Vertriebsgesellschaft mbH and Co. KG, Westerkappeln, Germany). The cell was sealed from ambient air by a lid made from PMMA through which the immersion objective extended into the fluid reservoir of the measuring cell. The reservoir was hermetically sealed by an O-ring between the objective and the lid to allow for an anaerobic atmosphere. Furthermore, a platinum wire used as counter electrode, a reference electrode (Ag/AgCl, KCl sat.), and inlet and outlet tubes were also inserted into the lid. The measuring cell was mounted

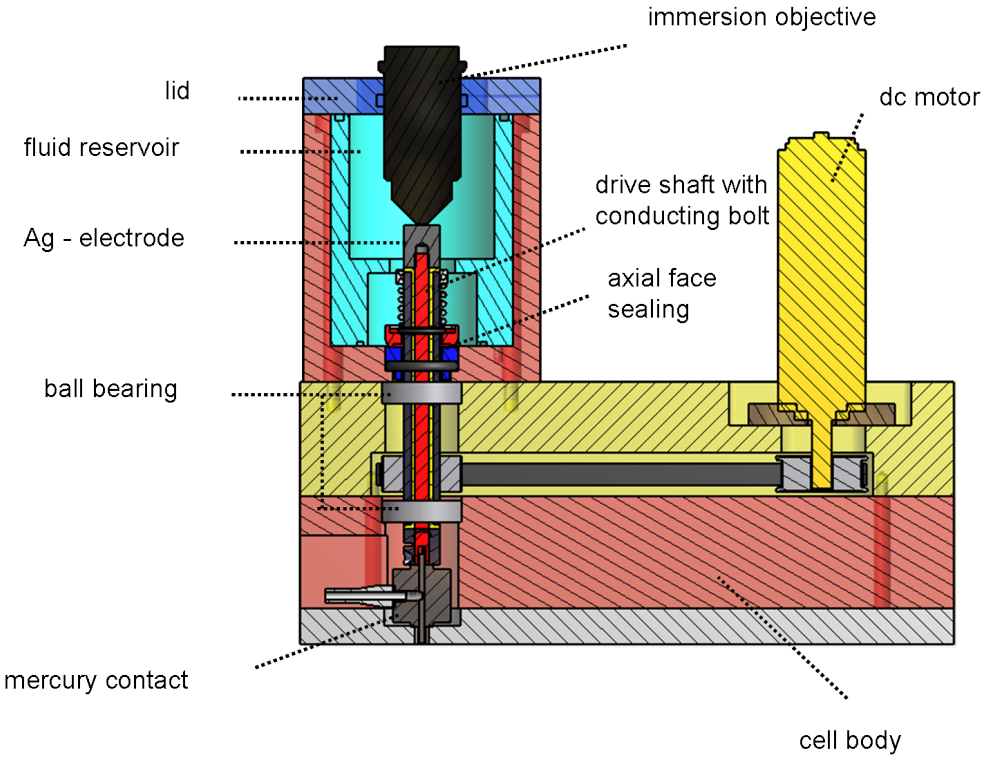

Figure 5.1: Cross section of the novel SERRS cell design. High precision rotation of the electrode allows for minimal-invasive observation of the protein by low-power laser irradiation. Permanent electrical contact is achieved by a mercury contact connected by a conductive bolt to the Ag-RDE. The drive shaft is sealed against the cell body by an axial face sealing.

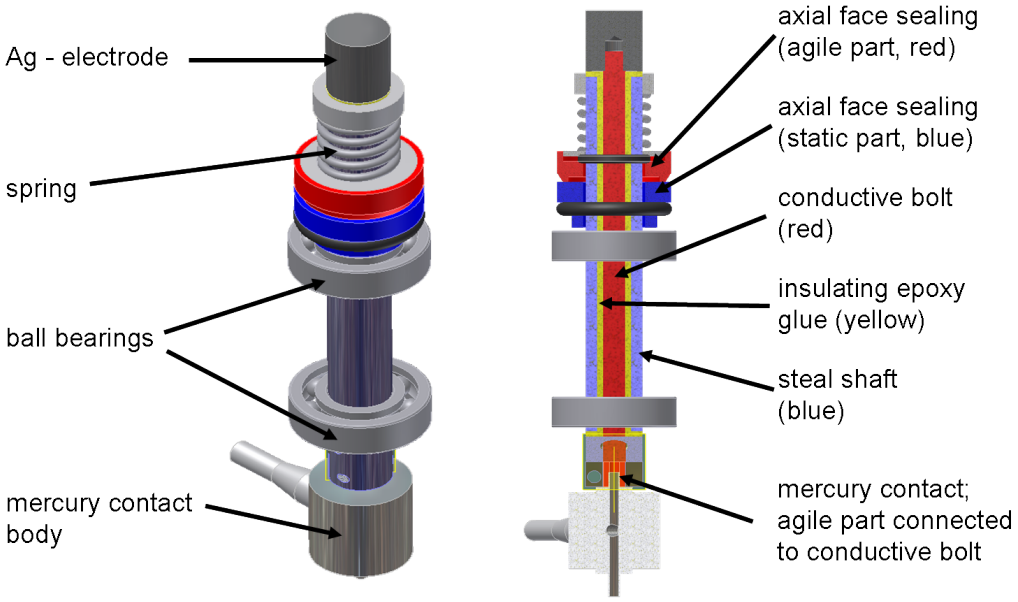

Figure 5.2: The drive shaft was the most challenging part developing the SERRS measuring cell. Running smoothness is assured by using a rigid stainless steel rod which is embedded into the PMMA cell body by high precision ball bearings. A conductive bolt is concentrically mounted by an epoxy glue having good insulating properties. The static part of the face sealing sealed the liquid reservoir against the cell body by an o-ring. The agile part was pressed against it by means of a spring. The Ag electrode was screwed on top while on the bottom the conductive bolt was connected to the agile part of the mercury contact, thus providing electric contact between the silver electrode and the potentiostat.

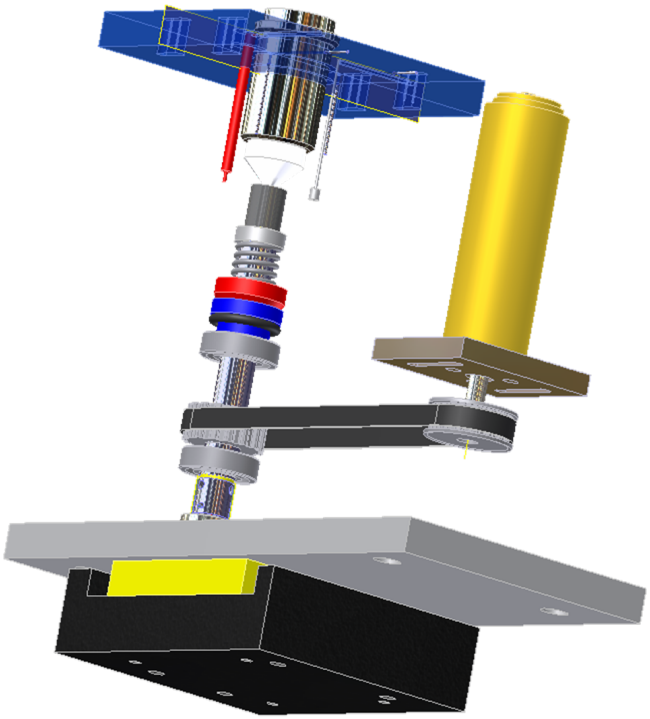

Figure 5.3: The working principle of the new measuring cell for SERRS. Only the functional components are shown. The RDE is illuminates from top by means of a water immersion objective. The backscattered light is collected by the same. A counter electrode and a reference electrode were also inserted into the lid. An offset of the RDE from the center of the microscope objective can be adjusted by a linear optical table.

on a linear optical table whereby the offset of the silver electrode from the center of the microscope objective was tunable. The working principle of the novel cell design is demonstrated in Figure 5.3 where only the functional groups are depicted.

5.1.3 Conclusion

The essential element of the SERRS setup turned out to be the measuring cell. Previous experiments with different sealing gaskets such as retaining ring seals proved to be not sufficient to prevent the electrolyte from leaking into the ball bearings [65, 73]. A tight seal was achieved only by an axial face seal that requires a strong motor for rotation. Other important factors were the machining precision that prevents wobbling of the electrode, thus keeping it in focus and at the same time allowing for a low laser power.

5.2 Electron Transfer Kinetics of Cytochrome c Probed by Time-Resolved SERRS

5.2.1 Introduction

Heterogeneous electron transfer of heme proteins adsorbed on metal surfaces can be investigated by spectro-electrochemistry [20, 67–72, 74–76]. A combination of surface-enhanced infrared absorption spectroscopy (SEIRAS) [77–79] and surface-enhanced Raman scattering (SERS) is particularly advantageous in this context. SEIRAS is designed to register changes of the protein backbone whereas SERS is sensitive to vibrations of the porphyrine ring [80–82], particularly in the resonance Raman (RR) mode [31, 83]. A strong absorption band in the visible blue frequency range is characteristic for heme proteins corresponding to the $\pi - \pi^*$ transition of the porphyrin. In order to obtain resonance Raman spectra the excitation wavelength must be concur with this transition. The band was named *Soret band* after Jacques-Louis Soret who discovered the characteristic absorption in 1883 [30]. In case of cc the Soret band is found at 410 nm.

Cc is known to adsorb on self-assembled monolayers (SAMs) bearing different end groups in different orientations. The heme cleft is either oriented perpendicularly to the electrode or at a 90° angle in the case of terminal carboxyl [84, 85] and pyridyl groups [86], respectively, thus facilitating electron transfer (eT). These orientations were investigated in detail by TR-SERRS [72]. ET rates were found in the range of $k_{eT} = 42 - 2400\,\mathrm{s}^{-1}$ depending on the tunnelling distance to the heme center given by the spacer length of the SAM. Cc adsorbed to OH-terminated layers, however, attracted less attention, as the heme cleft is directed away from the surface so as to hamper eT. Kinetic constants of cc adsorbed to mercaptoethanol (ME) layers obtained by electrochemistry were reported to be in the range of $k_{eT} = 20\,\mathrm{s}^{-1}$ [87]. TR-SEIRAS was used to determine eT rates of cc on the same architecture, but on a surface roughened by the assembly of Au nanoparticles (NPs) [88]. By applying overpotentials of +500 and −100 mV, respectively, relatively high eT rates were generated. In this case k_{eT} was found to be in the range of $1800\,\mathrm{s}^{-1}$. It was concluded from this study that the morphology of the surface might also play a role for the eT rate. SERRS also requires rough surfaces [35, 37]. In the present work TR-SERRS was used to investigate eT to cc adsorbed on ME layers.

5.2.2 Results

Cc adsorbed on the ME-modified Ag electrode was shown to be electroactive by cyclic voltammetry. The cyclic voltammogram (CV) shows cathodic and anodic peaks at 207 and 261mV, respectively, with a peak separation of 54mV indicating a diffusion-controlled process (Figure 5.4). However, the peak width of 95 mV is more compatible with an adsorbed species. Adsorption is also indicated by the dependence of electrochemical and SERRS signals on the immersion time and also of the ionic strength of the bulk solution. These results indicate the adsorption of cc at equilibrium with cc in solution.

Reduction and oxidation of cc was then followed by SERR spectra recorded as a function of applied potential (Figure 5.5). This was done using the newly developed SERRS measuring cell (Section 5.1). The marker band region be-

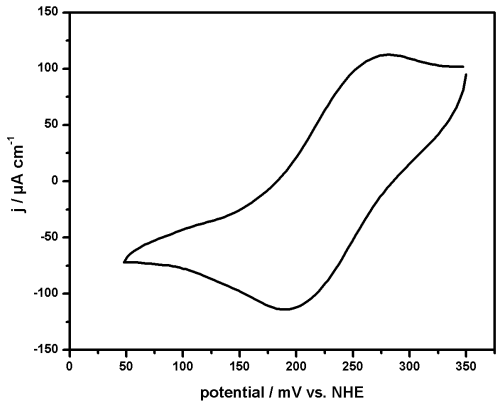

Figure 5.4: CV of cc adsorbed on a SAM of ME on the silver electrode shows cathodic and anodic peaks at 207 and 261 mV, respectively.

tween 1300 and 1650cm^{-1} exhibits four bands, which were assigned previously to the inherent vibrational modes (ν_2, ν_3, ν_4, ν_{10}) of the porphyrine ring [31]. The most prominent bands observed at 1361 and 1374 cm^{-1} account for the reduced and oxidized species, respectively. They are considered in terms of a distortion mode of the pyrrole halfring (ν_4), which is highly sensitive to the redox state of the central metal ion. According to Hu et al. [82] and Li et al. [89] the bands ν_2, ν_3, and ν_{10} originate from C-C stretching modes, which are, $\nu(C_\beta - C_\beta)$, $\nu(C_\alpha - C_m)_{sym}$, and $\nu(C_\alpha - C_m)_{asym}$, respectively.

The potential dependent transition from the reduced to the oxidized state of cc was clearly indicated by a gradual shift of the ν_4 band from 1361 to 1374 cm^{-1} (Figure 5.6). The intensities of the bands were determined by deconvolution of the Raman spectra as shown in Figure 5.7. The intensity of the marker band at 1361 cm^{-1} can be correlated to the concentration of the reduced species of cc. A sigmoid function (Equation 5.1) was fitted to the intensities plotted versus applied potential.

$$I_{SERRS} = \frac{1}{1 + \exp\left[(E - E_{ip})/\varphi\right]} \tag{5.1}$$

I_{SERRS} denotes the relative intensity of the ν_4 band at 1361 cm^{-1}. E_{ip} is the inflection point reflecting the midpoint potential E_m of the heme and φ

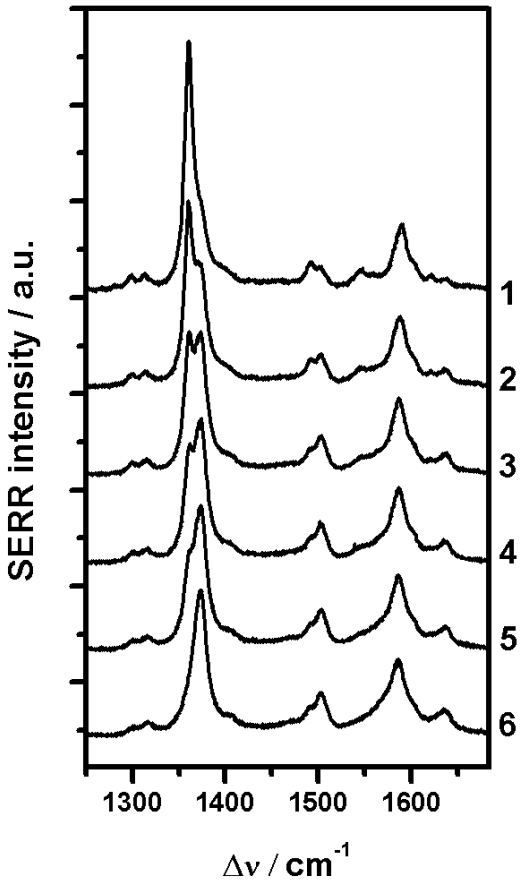

Figure 5.5: Potentiostatic titration of cc by SERRS. Spectra of cc were acquired at different static potentials applied to the immobilized protein. (1) +20, (2) +130, (3) +170, (4) +190, (5) +210, and (6) +330 mV.

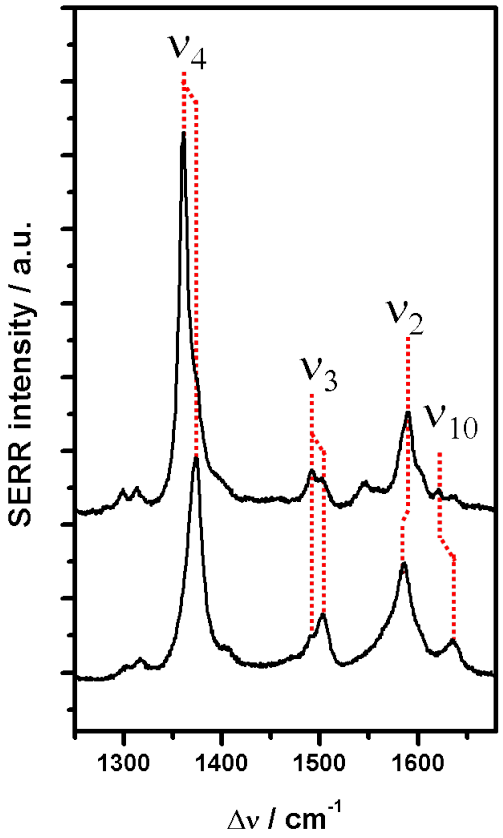

Figure 5.6: Band assignment of the SERR spectra. The band ν_4 resulting from a distortion mode of the pyrrole half-ring was used as a sensitive marker for the redox state of the protein.

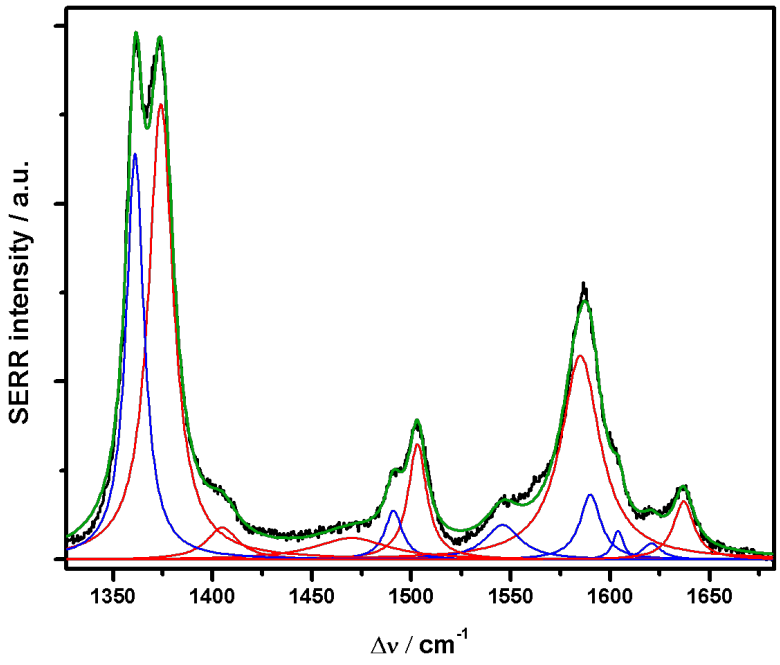

Figure 5.7: Deconvolution of a SERR spectrum recorded at +170 mV. Experimental data (black), overall fit (green), peaks from the reduced (blue), and oxidized (red) species of cc are displayed.

is a scaling factor. Ideally $\varphi = RT/F = 25\,\mathrm{mV}$ at $T = 25\,^{\circ}\mathrm{C}$ in accordance with the Nernst equation. The parameters were determined to be $\varphi = 36\,\mathrm{mV}$ and $E_{ip} = E_m = 160\,\mathrm{mV}$ (Figure 5.8).

TR-SERR spectra were then recorded triggered by the application of periodic potential pulses stepping between the initial potential $E_i = +380\,\mathrm{mV}$ and the final potential $E_f = -110\,\mathrm{mV}$, thereby alternating between the reduced and oxidized state of the protein. The frequency was adjusted to 10 Hz (Figure 5.9). Spectra were taken at different delay times after the application of the initial potential by illuminating the sample during measuring intervals Δt of 5 ms.

By increasing the delay time from 0 up to 100 ms, a series of 20 spectra was obtained, 10 for each half-period. The overall accumulation time of each

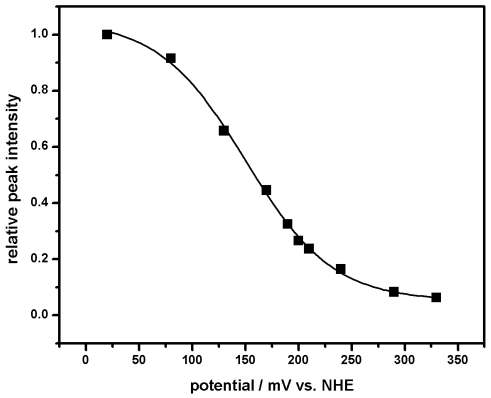

Figure 5.8: Relative intensity of the peak at 1361 cm^{-1} plotted vs the applied potential. Solid squares represent the experimental data. The solid line represents the fitted sigmoid function providing a calculated midpoint potential of $E_m = 160\,\mathrm{mV}$.

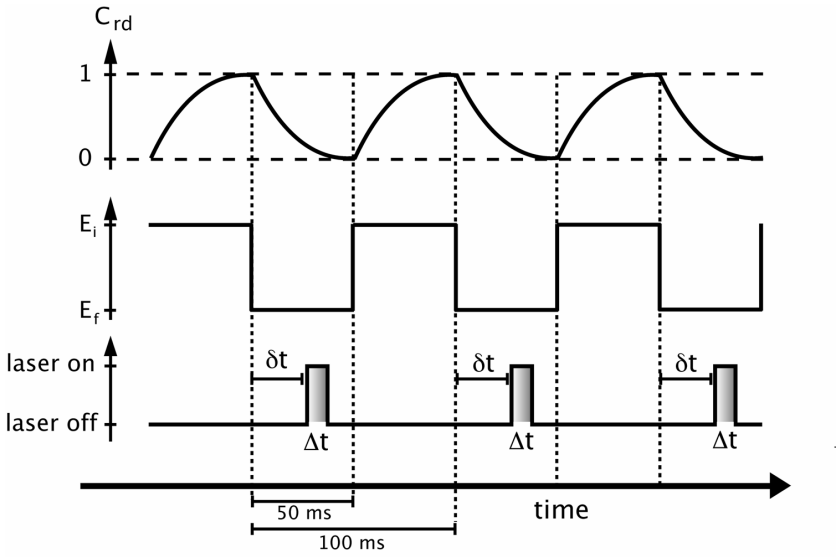

Figure 5.9: In TR-measurements, a periodic step potential is applied to the protein, which is synchronized with the illumination of the sample by short laser pulses ($\Delta t = 5\,\mathrm{ms}$) after different delay times δ. The increase or decrease in concentration of the reduced species of cc is observed by the intensity change of the corresponding Raman peak at 1361 cm^{-1}.

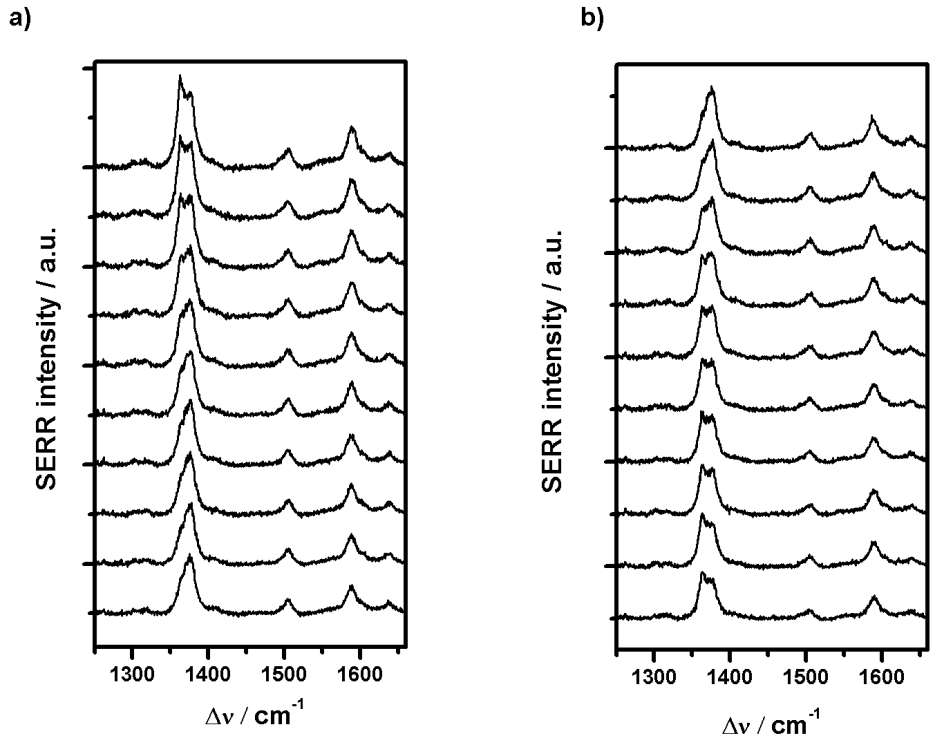

Figure 5.10: Time resolved SERR spectra of cc recorded after different delay times δt (0, 5, 10, 15, 20, 25, 30, 35, 40, and 45 ms from top to bottom) after a potential jump from -110 to +380 mV (a) and after a potential jump from +380 to −110 mV (b).

spectrum and time step was 100 s. Consequently the overall illumination time added up to 5 s.

The oxidation and reduction process was captured in the spectra 1 to 10 (Figure 5.10 a) and 11 to 20 (Figure 5.10 b), respectively. The SERR spectra depicted in Figure 5.10 were plotted from raw data, baseline corrected but not smoothed or averaged over multiple measurements. The peak intensity was plotted as a function of time and monoexponential functions were fitted to the data sets (Figure 5.11 a and b). The fit-functions

$$\Delta I_{ox}(t) = \Delta I_{max,ox} \exp[-k_{ox}(t - t_{0,ox})] + \Delta I_{0,ox} \tag{5.2}$$

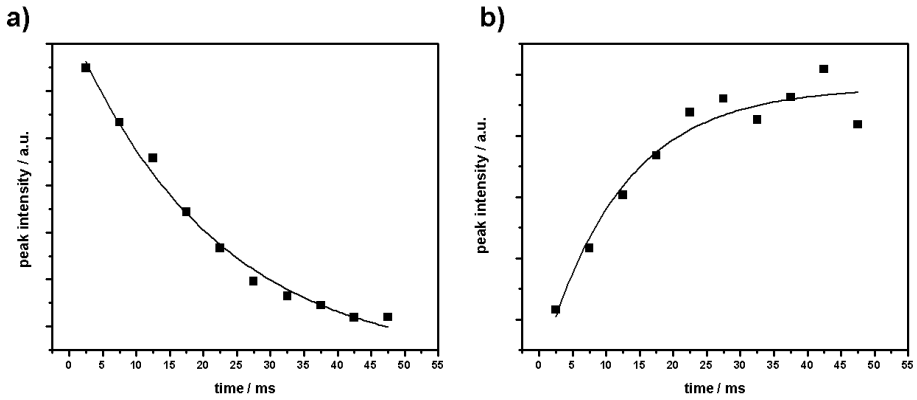

Figure 5.11: Intensity of the SERR peak at 1361 cm^{-1} is plotted vs the time after the potential jump. Experimental data of a single representative sample and a fit to a monoexponential function are depicted. The resulting time constant was calculated to be $k_{ox} = (46 \pm 7)\,s^{-1}$ for the oxidative branch (a) and $k_{rd} = (84 \pm 20)\,s^{-1}$ for the reductive branch (b).

and

$$\Delta I_{rd}(t) = \Delta I_{max,rd}\{1 - \exp[-k_{rd}(t - t_{0,rd})]\} + \Delta I_{0,rd} \tag{5.3}$$

were used for the oxidative and reductive branches, respectively, yielding a rate coefficient of $k_{ox} = (46 \pm 7)\ s^{-1}$ for the oxidative branch and $k_{rd} = (84 \pm 20)\ s^{-1}$ for the reductive branch. $\Delta I_{ox}(t)$ and $\Delta I_{rd}(t)$ are the SERRS intensities as a function of time, $I_{max,ox}$ and $I_{max,rd}$ are the maximal intensities of the SERRS signal, ΔI_0 are the intensities at the starting point of oxidation / reduction, and t_0 are the start times for the oxidative and reductive branches, respectively. The measurements were repeated three times using different samples. Time constants calculated from each individual data set were averaged. The overall error includes the experimental error (e.g., sample preparation) as well as the statistical error.

5.2.3 Conclusion

The standard redox potential ($E^0 = 234$ mV) obtained from cyclic voltammograms corresponds very well to values reported in the literature [87]. This indicates the electroactivity of cc on the electrochemically roughened Ag

surface. The redox potential obtained by potential-dependent static SERR spectra ($E_m = 160\,\mathrm{mV}$), however, was found to deviate from the standard redox potential ($E^0 = 230\,\mathrm{mV}$). This and the increased slope of the Nernst plot obtained by potential-dependent static SERR spectra have also been observed by others [67]. The reason could be the long time the protein is exposed to external potentials. This would indicate a certain instability of the layer structure of cc adsorbed to the ME monolayer.

The time needed to acquire data from TR-SERRS measurements is much shorter. Hence rate constants obtained from monoexponentials obtained by TR-SERRS are considered reliable. They compare favorably with $k_{eT} = 20\,\mathrm{s}^{-1}$ reported in Haas et al. [87] at least as far as the order of magnitude is concerned.

In any case, the eT transfer rate of cc adsorbed to a ME-modified roughened Ag electrode is much lower (between 46 and $84\,\mathrm{s}^{-1}$) than that found by TR-SEIRAS on a Au electrode modified by AuNPs ($\approx 1800\,\mathrm{s}^{-1}$). The low value was explained by the authors of Haas et al. [87] in terms of the orientation of the heme cleft pointing away from the electrode, which is not in favor of an effective eT. The electrochemically roughened Ag electrode behaves very much like a flat electrode modified by ME. Hence the morphology of the surface does not seem to play the same role as in the case of Au electrodes modified by AuNPs.

5.3 Silver Surfaces with Optimized Surface Enhancement by Self-Assembly of Silver Nanoparticles for Spectroelectrochemical Applications

5.3.1 Introduction

Surface enhanced Raman scattering requires the use of metal substrates exhibiting a defined roughness on the nanometer scale. A variety of methods

to produce such substrates were introduced so far [67, 90–92]. The most frequently used method is the electrochemical roughening of silver [67, 90] as used in this work for investigating cc by SERRS (Sections 4.1.3 and 5.2). However, artificial membrane systems such as the ptBLM require flat surfaces, while on the one hand the surface roughness is indispensable for sufficiently high Raman intensities. In this context a novel surface architecture was developed based on a planar silver substrate modified with silver nanoparticles. This architecture proved to allow for both, a proper membrane formation and a high electro magnetic field enhancement. Raman scattering is a weak photon-molecule interaction. The Raman scattering cross section is on the order of magnitude of $10^{-30}\,\mathrm{cm}^{-1}$ [93]. Nevertheless, Raman spectroscopy has become an important analytical tool in many fields of science, such as chemistry, medicine, and the life sciences [94–96]. This is mainly due to the fact this technique experienced a dramatic impulse by the discovery of the surface enhancement effect of roughened surfaces by Fleischmann et al. [35].

Different mechanisms contribute to the enhanced Raman scattering of molecules adsorbed on rough metal substrates. The electromagnetic enhancement effect [36] (EMEE) and the chemical enhancement effect (CEE) [37], the latter also known as charge transfer effect, are of great interest in this context. The EMEE is based on collective electron oscillations in resonance with the exciting laser wavelength yielding high electromagnetic field enhancement in the proximity of the metal surface [97]. In the literature such electron oscillations are often referred to as localized surface plasmons (LSP), particularly if they are excited within nanoscopic metal structures such as colloids or rough surface bumps. When two or more nanostructures approach each other to an extent where there is an overlap between the electromagnetic (EM) fields radiated by the LSPs, so-called coupled LSP oscillations may occur [98–101]. Coupled LSP exhibit an even higher EM field enhancement in the gap between two nanoparticles (NP) [102]. These gaps between resonantly coupled NPs are referred to as "hot spots". Moreover, the resonance frequency of such complexes can be shifted away from the frequency of single NPs [103]. Touching particle pairs exhibit a conductive bridge in

the plane of electron oscillation and are thus capable of being excited with additional LSP modes at lower frequencies [100, 103]. At the same time the primary modes are still red-shifted as in the case of nearly touching particles [101, 103]. The EMEE is capable of enhancing the intensity of Raman spectra of all molecules in close proximity to the metal substrate. Contrary to the EMEE, the CEE only occurs if the probed molecules are adsorbed on the surface. The underlying mechanism is a charge-transfer resonance between the metal substrate and the adsorbed molecule. Assuming the Fermi level of the metal is located between the ground state and an excited state of the molecule, charge transfer transitions from the Fermi level to the excited state, as well as transitions from the ground state to the Fermi level, can contribute to the CEE [39, 47].

Although these effects are now well understood, it is still difficult to differentiate between contributions from EMEE and CEE. EM enhancement may be observed in the absence of chemical enhancement when the molecules are not adsorbed to the metal substrate. In contrast, chemical enhancement is always accompanied by EM enhancement. Notwithstanding the enhancement effects, poor signal-to-noise ratios in Raman spectra are an inherent problem of the weak scattering process. Particularly low intensities are observed while probing a monolayer of molecules in the case of spectroelectrochemistry. The short accumulation time of time-resolved spectra further limits the quality of the spectra. Nevertheless, spectroelectrochemistry as well as time-resolved Raman spectroscopy in combination with the surface enhancement gives access to parameters such as rate constants of electron transfer or conformational changes in proteins inaccessible by normal Raman experiments [104]. In the majority of surface-enhanced (resonance) Raman scattering (SER(R)S) experiments, however, electrochemically roughened silver electrodes were employed [67, 90, 104]. A drawback of this technique is that the enhancement effect is hard to control. It heavily depends on the exact conditions of the oxidation-reduction cycle (ORC), i.e., the duration and magnitude of the applied potential as well as the molarity of the salt solution. Nevertheless, Taylor et al. [105] reported a typical enhancement factor of $2 \cdot 10^4$ for such substrates. Wen and Fang [106] made an attempt to

improve the enhancement factor by adsorbing silver nanoparticles on electrochemically roughened silver electrodes. This technique, however, was not designed to overcome the high surface roughness obtained by any kind of ORC. The high roughness does not allow the arrangement of well-ordered monolayers, often significant in the context of electrochemical processes. Moreover, controlling the enhancement effect remains a problem due to irregularities of the underlayer.

In order to overcome these drawbacks an attempt was made to develop a SERR-active surface by the adsorption of silver colloids on a planar silver surface. Varying the amount of adsorbed NPs gave us the advantage of a controlled enhancement effect. Moreover, the roughness was dramatically reduced compared to the electrochemical roughening as it was determined only by the size of the colloids. Such LSP of nanostuctures have been reported before, however, on dielectric or semiconductive surfaces such as glass, silicon, or ITO [100, 101, 107]. Colloidal particles are not conductively connected in this case, unlike the conducting silver surface. Possible effects of this conductive connection were investigated together with the effect of the distribution of NPs on the Ag surface. The number of NPs on the surface was controlled by varying the adsorption time. The correlation between the number of NPs and Raman intensity was examined using cytochrome c (cc) adsorbed to a monolayer of mercaptoethanol, as a reference. LSPs were excited using the 413 nm line of a Kr^+ laser.

5.3.2 Results

Silver nanoparticles were fabricated by the method developed by Turkevich and Frens using citric acid as a reducing agent (Section 4.1.3. The additional use of formaldehyde proved very effective in suppressing cluster formation. As a result, dynamic light scattering (DLS) revealed a highly monodisperse solution of spherical NPs of an average size of 39 nm (inset, Figure 5.12). UV-vis spectra of the colloidal suspension showed a distinct maximum of the extinction at a wavelength of 410 nm. This corresponds to the wavelength of the laser beam (413nm) used for the excitation of the Raman scattering. The

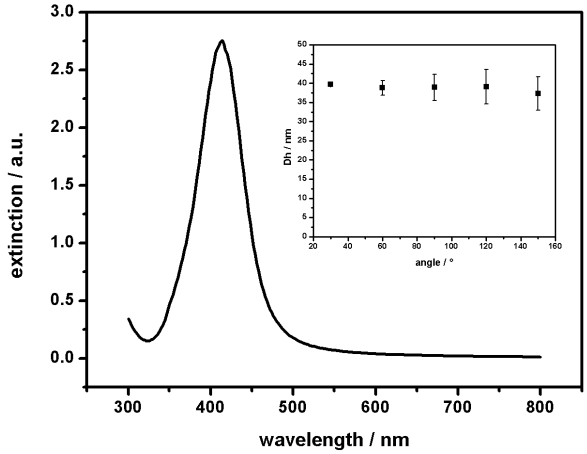

Figure 5.12: UV-vis spectrum of AgNPs in solution. A distinct local maximum at 410 nm indicates the LSP resonance of the nanospheres. Inset: DLS data. The average size of the AgNPs amounts to 39 nm.

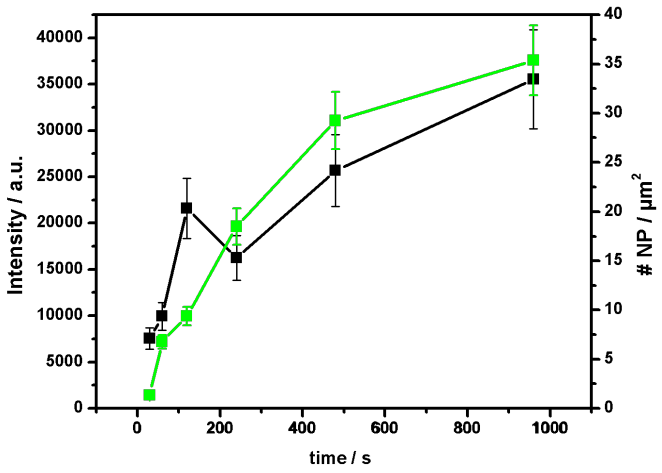

Figure 5.13: Raman intensity of the ν_4 band plotted as a function of NP adsorption time (black) compared to the total number of NPs adsorbed on the surface (green). The Raman intensity is proportional to the number of NPs as long as the interparticle distance does not allow for LSP coupling of neighboring NPs.

absorbance maximum of 410 nm indicates the excitation of localized surface plasmons within the NPs at this particular wavelength (Figure 5.12).

AgNPs thus formed are characterized by a negatively charged envelope of citric acid, which enables them to adsorb on the positively charged monolayer of cysteamine (CA) on the flat surface of a silver rod. Once adsorbed, the NPs could not be removed by rinsing with water or other solutions, even those containing thiols such as mercaptoethanol (ME). Such a solution was later used to modify the outer surface of the assembly of AgNPs with yet another monolayer of ME. Particles were assembled on the surface by immersion into the suspension of AgNPs at the concentration as obtained by the preparation procedure described above.

The number of AgNPs per unit area adsorbed on the SAM of CA was controlled by varying the time of immersion of the polished silver rods in the colloidal suspension. The number of particles finally obtained was taken from SEM images of the modified surfaces. Particle counting was done by the software ImageJ. Within a range of minutes ($\leq$ 16 min) the number of particles increased up to 35 $NPs/\mu m^2$ as a function of the immersion time (Figure 5.13). For each data point 2-3 different samples have been analyzed at 2-3 different spots. The error bars given in the figures represent the experimental error (e.g., particle counting) as well as the sample-to-sample deviation. Particles were explicitly separated from each other in this regime (Figure 5.14). This was not the case when immersion times were longer than 16 min. At a certain particle density ($\approx$ 100 $NPs/\mu m^2$ or after 1 h) adsorption of further particles no longer correlated with time anymore. After 3 h, the particle density reached $\approx$ 270 $NPs/\mu m^2$, and a further adsorption of NPs could not be observed (Figure 5.15). This might be due to repulsive forces originating from the surface charges of the silver spheres. The highest enhancement was not observed on surfaces with the highest NP coverage. Hence, not all NPs contribute to the EM field enhancement as in the low particle density regime. The highest enhancement was achieved after an adsorption time of $\approx$ 2 h when a particle density of $\approx$ 200 $NPs/\mu m^2$ was reached. Further adsorption of NPs did not lead to higher peak intensities, but to a decrease in enhancement. In fact, a definite correlation between the

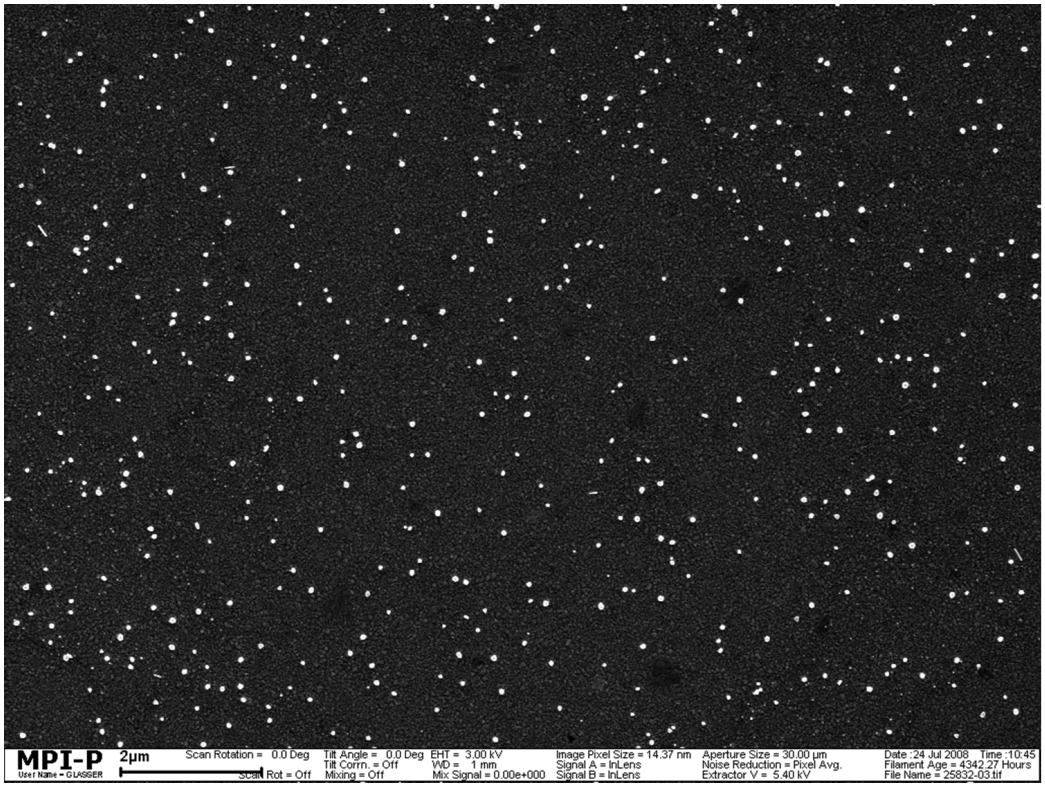

Figure 5.14: SEM image of AgNPs after an adsorption time of 16 min. Individual NPs are strictly separated from each other; hence, no particle interactions occur.

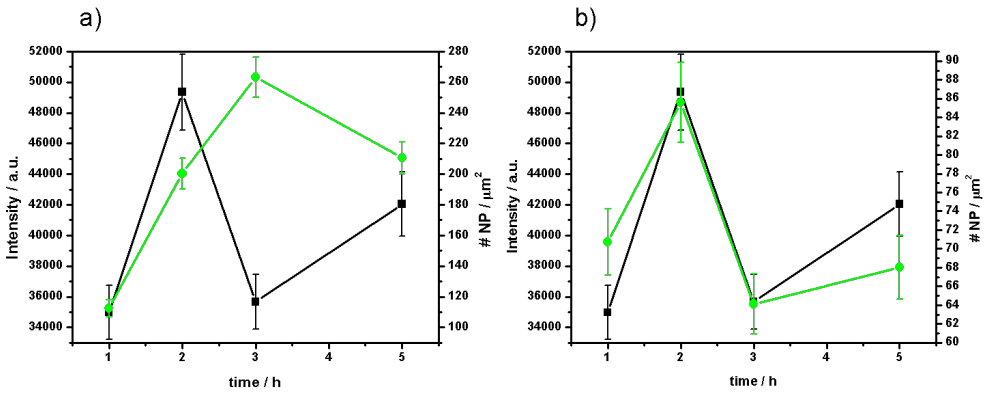

Figure 5.15: Raman intensity of the ν_4 band plotted as a function of NP adsorption time (black) compared to (a) the total number of NPs adsorbed on the surface (green) and (b) the number of strictly separated NPs. The Raman intensities do not correlate with the total number of NPs, but instead with the number of strictly separated NPs.

total amount of NPs and the peak intensities in the Raman spectra was not found (Figure 5.15 a).

This behavior was correlated with the enhancement effect by measurements of SERR spectra of cc adsorbed on the different surfaces via a monolayer of ME. For this purpose the Raman band ν_4 at 1374 cm^{-1} of oxidized cc resulting from a distortion mode of the pyrrole half-ring [82] was used as a marker band. Its peak intensity was then correlated with the surface enhancement. In the low particle density regime ($\leq$ 16 min) the peak intensity of the ν_4 band was directly proportional to the number of particles. Hence, all the NPs contributed equally to the observed signal by enhancing the EM field in close proximity of the individual particles (Figure 5.13).

A detailed analysis of the particle distribution was performed using the software ImageJ (particle detection and counting) and Gimp 2.0 (image processing) to evaluate SEM images. This allowed to discriminate between separate NPs and clusters of adhering NPs (Figure 5.16). The distribution across the plane of the silver surface revealed a steady increase of clusters of particles in direct contact and therefore forming conductive bridges between neighboring particles (Figure 5.16). A strict discrimination between sepa-

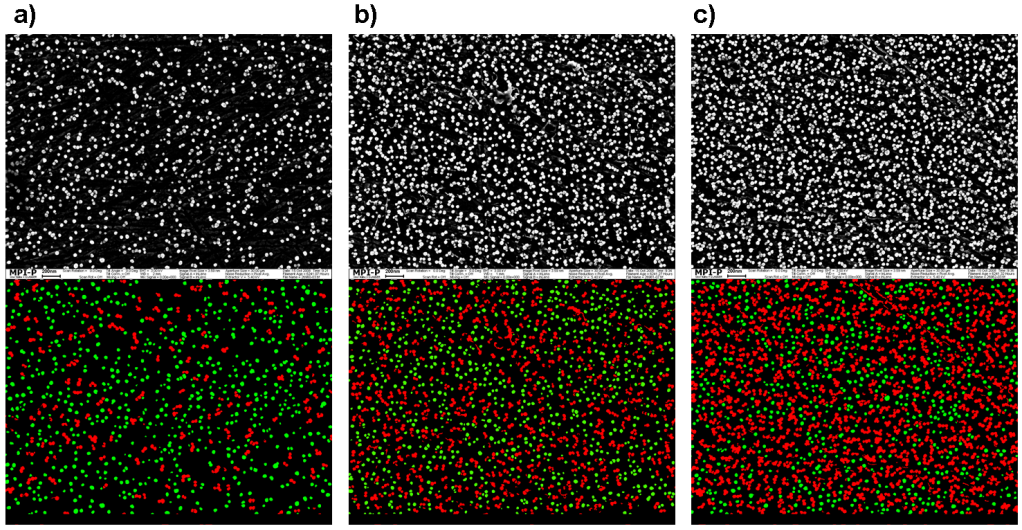

Figure 5.16: SEM images of NPs after adsorption times of 1 (a), 2 (b), and 3 (c) h. The total amount of NPs increases from 1 to 3 h adsorption time. The lower row shows the same SEM images with particle clusters and separated particles colored red and green, respectively. The amount of particle clusters increases from 1 to 3 h adsorption time, while the amount of separated NPs reaches its maximum after 2 h.

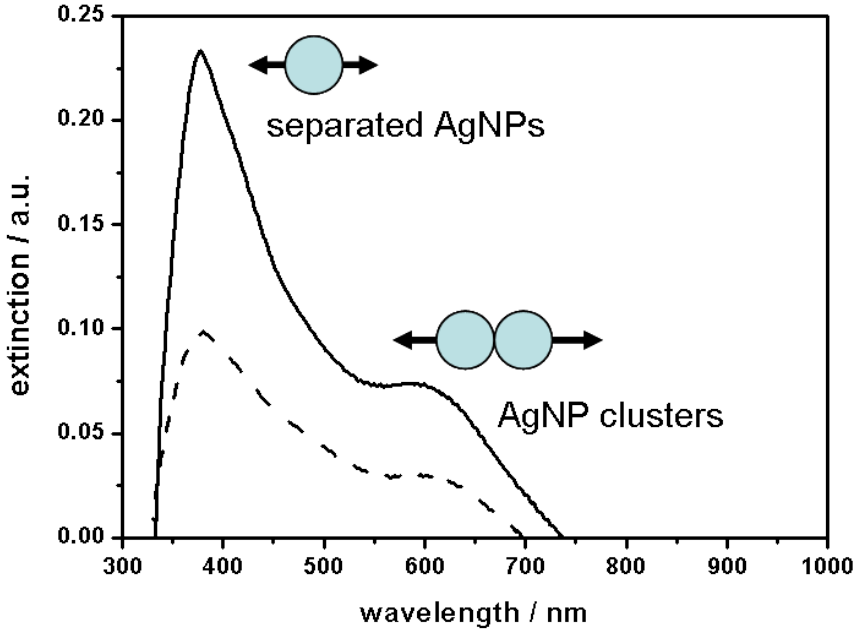

Figure 5.17: Uv-vis spectrum of NPs adsorbed on a 50 nm Ag film on a glass substrate after adsorption times of 1 h (lower trace) and 2 h (upper trace). Local maxima of the extinction are observed at around 390 and 600 nm due to LSP resonance of separated NPs and particle clusters, respectively.

rated NPs and those arranged in clusters gives evidence of the correlation between the peak intensities of Raman spectra and the amount of separate NPs (Figure 5.15 b). NPs arranged in clusters of two or more particles did not contribute to the enhanced Raman signal. UV-vis spectroscopy revealed large shifts to higher wavelengths in the LSP resonance of particle aggregates (Figure 5.17). The spectra were recorded using 50 nm evaporated silver on a glass slide as a substrate for AgNP adsorption. The two local extinction maxima at 390 and 600 nm resulted from different modes of LSP resonance. They were assigned to the LSP resonance of separated NPs and the particle clusters of two or more particles, respectively. Thus, NP aggregates were not amenable to the excitation of LSPs at the same wavelength as a single NP. Consequently, they did not contribute to surface-enhanced Raman scattering. Large red shifts in the resonance frequency of particles touching each others were shown previously, both theoretically and experimentally [100, 101, 107].

Nevertheless, the resonance frequency of the LSP of single NPs was still in a range to be excited with the 413 nm laser line, although Ag was used as a conductive substrate in contrast to the work of others, who used dielectric substrates such as glass. However, the extinction maximum of isolated AgNPs was slightly downshifted to $\approx$ 390 nm. This effect can be explained in terms of the permittivity of the surrounding media of the AgNPs, which is known to affect the LSP resonance frequency. In the case of the AgNP suspension the surrounding medium was basically water, while in the case of adsorbed NPs, the NPs were surrounded by air. The permittivity of water exceeds the permittivity of air, whereby LSP resonance is shifted to higher energies.

A conductive substrate was employed in order to perform spectroelectrochemical measurements. Therefore, all NPs were in electric contact with each other via the plane of the silver electrode. This did not seem to affect the resonance frequency of the LSP. It can be concluded that optical properties of NP assemblies are affected only by conductive bridges in the plane of local electron oscillations.

As a further parameter of the image analysis, the average distance to the next neighbor (NN) was obtained (Figure 5.18). Single, nontouching NPs

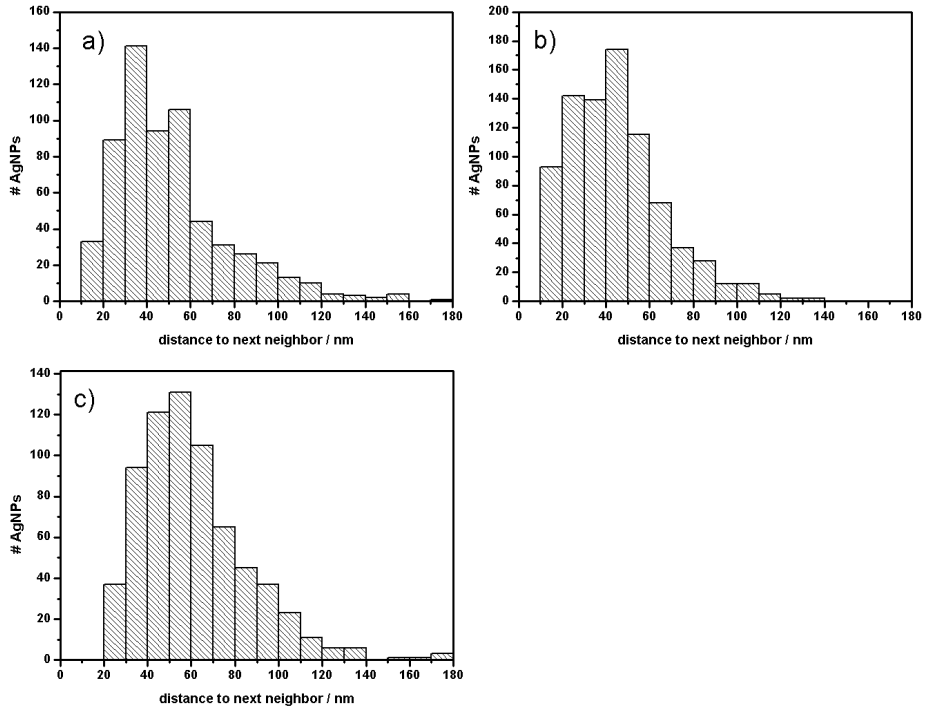

Figure 5.18: Histograms show the statistical distribution of the distance to the next neighbor for each particle. The NP adsorption times were 1 (a), 2 (b), and 3 h (c). The average distances to the next neighbor were 51, 45, and 51 nm, respectively.

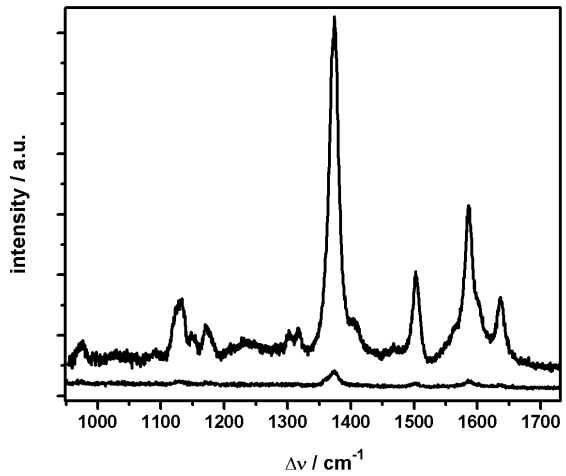

Figure 5.19: Raman spectra of cytochrome c adsorbed on a layer of AgNPs (upper trace) and adsorbed on the plane of a polished silver electrode (lower trace).

were separated by 45–51 nm on average, the distance being in the range of the particle diameter. In the case of 2 h assembly time, the distribution of NN shows a tendency to distance lower than the NP diameter, as compared to both the 1 and 3 h. This could explain the slightly disproportional increase in Raman intensity compared to the increase in separated NPs after an adsorption time of 2 h. The effect might be due to such coupled LSPs and the increase in the EM field strength as a consequence of the coupling effect. However, from the distance distribution to the NNs it follows that coupled LSPs are of importance for only a minor fraction of the separated NPs.

In Figure 5.19, the Raman scattering spectra of cc is depicted. The AgNP-modified substrate used in this case was prepared under the conditions found to be optimal in terms of Raman signal enhancement; i.e., AgNPs were allowed to adsorb for 2 h. The signal accumulation time was 15 s, and the laser power was adjusted to less than 100 μW. A SEM image of this AgNP substrate is shown in Figure 5.20. Finally, the total average SERRS

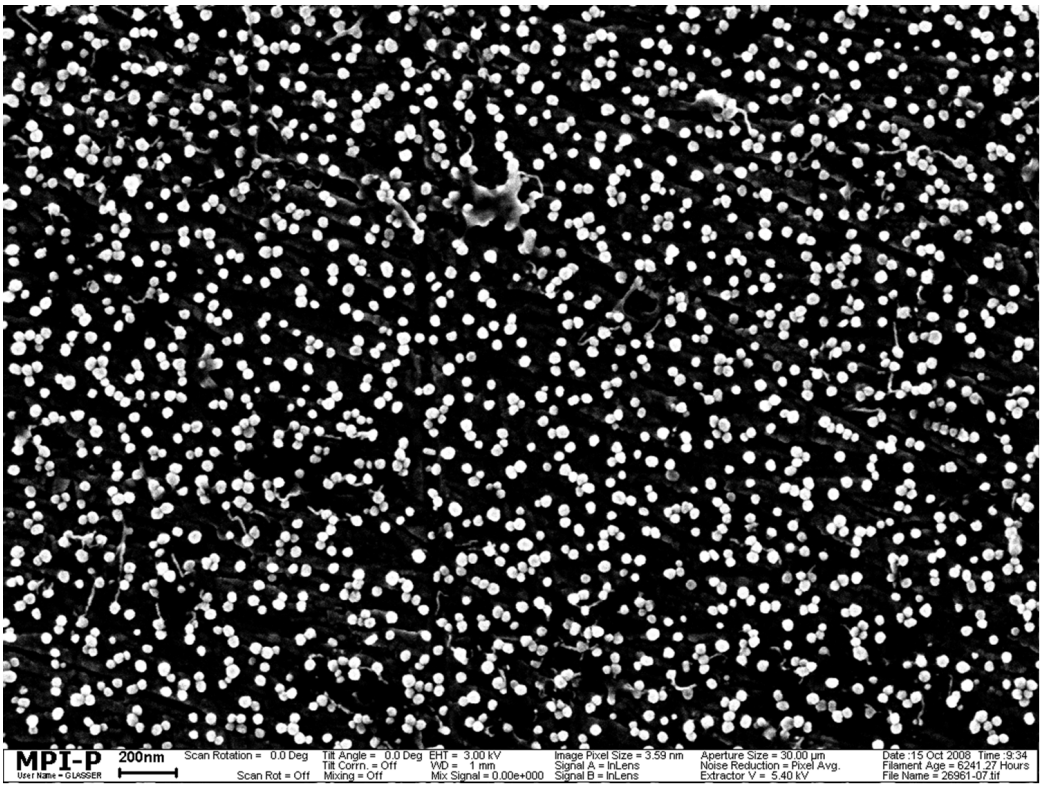

Figure 5.20: SEM images of AgNPs after an adsorption time of 2 h. The image illustrates the narrow distribution in size of the adsorbed NPs. Most NPs are separated from their next neighbor, but a small fraction is arranged in clusters of two or more particles.

enhancement factor was calculated according to Le Ru et al. [108]

$$EF = \frac{I_{SERRS}}{I_{RR}} \cdot \frac{N_{surf}}{N_{vol}} \tag{5.4}$$

with I_{SERRS} and I_{RR} the Raman intensity observed on the SERRS-active surface and in solution, respectively, and N_{surf} and N_{vol} the number of sampled molecules adsorbed on the surface and in solution. N_{surf} and N_{vol} was estimated respectively to be $3.75 \cdot 10^6$ and $3.75 \cdot 10^8$ molecules from the peak area of cyclic voltammograms of cytochrome c (Figure 5.4) and the molarity of the sample solution and the volume illuminated by the laser. The SERRS intensity was ≈ 100 times higher compared to the resonance Raman intensity, while the signal accumulation time was 15 and 150 s, respectively. Taking these data into account, the enhancement factor was calculated to be $EF = 10^5$. The SERRS intensity increased by a factor of up to 4 on the newly developed surface compared to previous experiments with cytochrome c adsorbed on electrochemically roughened silver electrodes. The enhancement factor for electrochemically modified silver substrates is known to be in the range of $2 \cdot 10^4$ [105], which is in line with the calculated EF of 10^5 for the novel silver substrate modified with AgNPs.

In order to test the electrochemical activity of the newly developed SER(R)S-active silver substrate, a spectro-electrochemical titration of cc was performed. Cytochrome c was adsorbed on a SAM of ME. Changing the applied potential stepwise between -50 and +350 mV vs NHE, SERR spectra were taken (Figure 5.21). The protein showed a transition from the reduced to the oxidized state, as deduced from the ν_4 band changing from 1361 to 1374cm^{-1}. This is in line with the previous studies on cc on electrochemically roughened silver electrodes (Section 5.2) [104]. The relative intensity of the ν_4 band at 1361 cm^{-1} was plotted as a function of applied potential (Figure 5.22) and fitted to the sigmoidic function

$$I_{SERRS} = \frac{1}{1 + \exp\left[(E - E_{ip})/\varphi\right]} \tag{5.5}$$

where I_{SERRS} denotes the relative intensity of the ν_4 band at 1361 cm^{-1}. E_{ip}

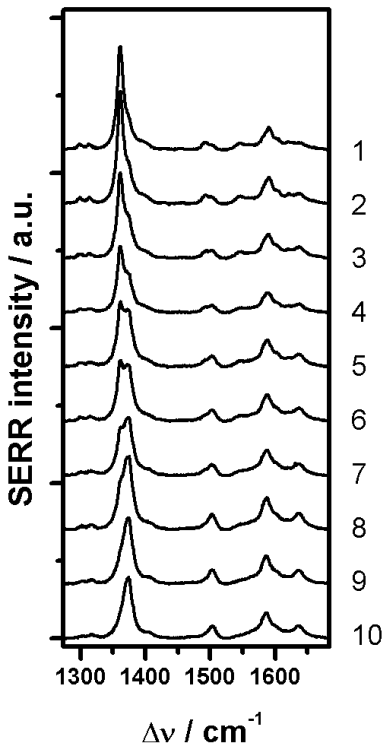

Figure 5.21: Potentiostatic titration of cc by SERRS. Spectra of cc were acquired at different static potentials applied to the protein immobilized on the SERR-active Ag surface. (1) -50, (2) +20, (3) +80, (4) +130, (5) +170, (6) +190, (7) +210, (8) +250, (9) +300, and (10) +350 mV vs NHE.

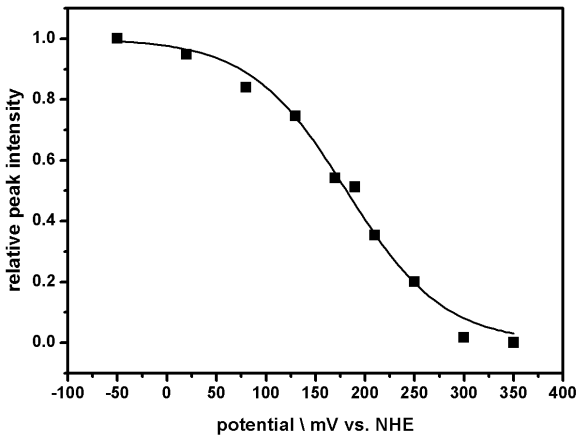

Figure 5.22: Relative intensity of the ν_4 band at 1361 cm^{-1} plotted vs the applied potential. Solid squares represent the experimental data. The solid line is the fit of Equation 5.5 providing a calculated standard potential of $E_m = 181$ mV.

is the potential of the inflection point, which reflects the midpoint potential E_m of the redox center, and φ is a scaling factor. Ideally, $\varphi = RT/F \approx 26$ mV, and $E_{ip} = E_m$ in accordance with the Nernst equation. E_{ip} revealed a midpoint potential of $E_m = (181 \pm 4)$ mV, and the scaling factor was $\varphi = 49$ mV. From this fact it can be concluded that cc adsorbed to a monolayer of ME can be electrochemically reduced and oxidized on the newly developed SERR-active surface.

5.3.3 Conclusion

A SE(R)RS-active surface was developed by assembling a monolayer of Ag NPs on a silver plane. By varying the number of NPs per unit area the enhancement factor could be tuned so as to exceed that of electrochemically roughened silver electrodes. Under optimum conditions the total average enhancement factor calculates to $EF = 10^5$. The enhancement factor was shown to be determined largely by the number of explicitly isolated NPs rather than NP clusters. This effect could be explained in terms of LSPs equivalent to NPs on nonconducting surfaces such as glass. Distances

between single NPs were not small enough to play a decisive role for the enhancement factor at the particular wavelength used (413 nm). The conducting underlayer of the Ag plane, on the other hand, did not seem to be prohibitive for the surface enhancement, while it allowed the application of spectroelectrochemistry. This was tested by potentiostatic titration of cc adsorbed on a SAM of ME. The results demonstrate an electrochemical activity similar to electrochemically roughened electrodes.

At the same time the new SE(R)RS-active substrates are easy to produce. This is quite an important fact since investigations of complex systems such as CcO in a ptBLM architecture can require the preparation of a large number of samples. Preparing the biomimetic membrane system not only presupposes experience but it also needs a long time to proceed through all fabrication steps (up to 5 days). Hence, an easy and fast preparation of the SE(R)RS-active substrates is an important feature for the user.

In the context of spectroelectrochemistry, the newly developed surface has the potential to replace electrochemically roughened silver as a standard substrate for SER(R)S measurements.

5.4 Cytochome c Oxidase: Electrochemically Induced Electron Transfer Probed by Surface Enhanced Resonance Raman Spectroscopy (SERRS)

5.4.1 Introduction

Electrochemical reduction and oxidation can provide interesting insight into structure-function relationships of redox proteins, particularly in combination with spectroscopic techniques [109, 110]. Raman as well as FTIR spectroscopy in combination with electrochemical excitation provided information about changes in heme structures and peptide groups under static and time-resolved conditions, respectively [111–113]. Electron transfer kinetics

of redox enzymes was investigated by protein film voltammetry [114, 115] under turnover and non-turnover conditions. However, a basic problem inherent in these studies is the effective link between electrode and electron acceptor within the protein. Mediators were used in many cases allowing but only for static measurements of equilibrium states [116, 117]. Catalytic turn-over, on the other hand, can be observed when direct electron transfer (ET) is ensured. Protein films were successfully applied for this purpose. However, unspecific adsorption may result in tunnel pathways different from the one initiated by the natural substrate. A way out is electronic wiring of the protein, preferably by a conjugated linker. Another possibility is the immobilization of the protein via his-tag technology, which we had introduced earlier, in particular for the application with membrane proteins. A lipid bilayer was reconstituted around the protein to form a protein tethered bilayer lipid membrane (ptBLM). Direct ET had been shown to occur to Cytochrome c Oxidase (CcO) from R. sphaeroidis provided it was immobilized with the first electron acceptor Cu_A directed toward the electrode [20, 75, 118]. Fast scan voltammetry indicated the sequential ET along the four redox centers Cu_A, heme a, heme a_3 and Cu_B thus mimicking the natural tunnel pathway through the protein [118]. Moreoever, CcO could be electrochemically manipulated to acquire two distinct conformational states [119] one of which, in the presence of O_2, was shown to be catalytically active. Changes in amino acids including secondary structures involved in redox reactions were revealed by potentiometric titrations followed by surface-enhanced infrared absorption spectroscopy (SEIRAS) [119]. For mechanistic studies resonance Raman (RR) spectroscopy proved to be a powerful technique. This is because excitation within the heme $\pi - \pi^*$ electronic absorption transitions selectively enhances vibrational modes of the heme porphyrin ring and bound ligands without the interference from the modes associated with the protein matrix [28, 120–125]. The Raman active vibrational modes of the porphyrine ring of the hemes are sensitive to the redox state of the central metal ion [67]. Resonance Raman (RR) spectra of the CcO in solution were measured in the fully oxidized and reduced form obtained by chemical reduction and oxidation using dithionite/ferricyanide, respectively [116, 117]. Band assignments

to different vibrational modes were performed on the basis of these measurements. The surface-enhancement effect of rough surfaces combined with RR spectroscopy resulted in the invention of SERRS, which was soon applied to heme proteins including CcO [126]. Direct ET to CcO immobilized in a ptBLM measured by SERRS had indicated the electrochemical reduction of the hemes, however a detailed analysis of the potential dependent changes by deconvolution of the partially overlapping SERRS bands was not possible. This restriction was due to the fact that these experiments were conducted on conventional SERR-active surfaces, i.e. Ag surfaces subject to repeated electrochemical reduction/oxidation cycles. This technique gives rise to very rough surfaces thus providing surface enhancement, however, due to the extremely irregular features a poor substrate for a properly arranged lipid bilayer membrane. In the present study this is improved by using a the SERR-active surface described in Section 5.3, comprising Ag nanoparticles (NPs) assembled on a smooth Ag surface [58]. Bilayer lipid membranes (BLMs) were shown to form on spherical particles [127, 128]. Hence ptBLMs can be expected to assemble around NPs as well. Potentiometric titrations were performed in order to observe electrochemical reduction and oxidation of the hemes followed by SERRS.

5.4.2 Results

CcO was tethered to the silver electrode modified with silver nanoparticles (AgNPs) and stabilized by reconstitution into a ptBLM (Figure 5.23). Electrochemical impedance spectroscopy (EIS) and surface plasmon resonance (SPR) spectroscopy were employed to monitor the binding of CcO to the linker molecule as well as the reconstitution into a ptBLM. CV was then used to test the catalytic activity of the enzyme. SERRS was performed to characterize and analyze electron transfer to and between heme a/a_3.

SPR spectroscopy

SPR spectra were recorded on both plain TSS and on TSS modified by AgNPs. The AgNPs led to a broadening of the plasmon excitation curve

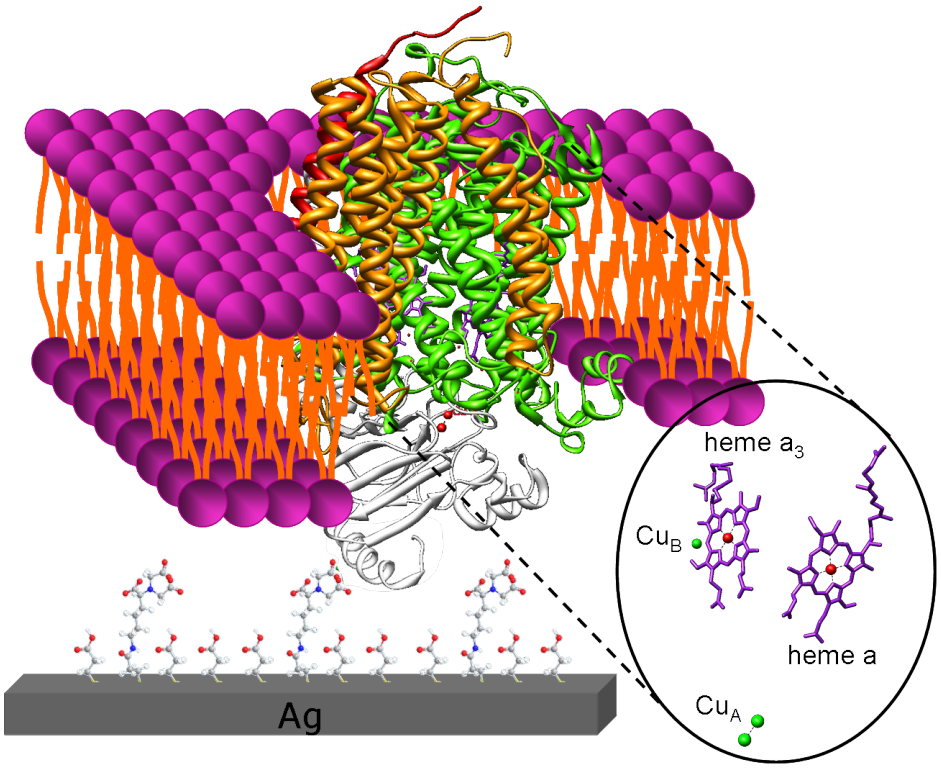

Figure 5.23: CcO in a biomimetic architecture. The protein with the his-tag attached to SU II was immobilized on top of the SERRS-active substrate and subsequentialy stabilized by reconstitution into a ptBLM. In this configuration the enzyme could be addressed by direct electron transfer to the redox centers.

compared to the one obtained on TSS (inset Figure 5.24). Nevertheless, the trailing edge of the curve was steep enough to follow the kinetics of protein adsorption and membrane reconstitution (Figure 5.24). The starting point was the AgNP modified silver substrate functionalized with the Ni - DT-NTA immersed in DDM containing PBS. As soon as the solubilized CcO was added a strong increase in reflectivity was observed indicating the adsorption of CcO. After 45 min the adsorption process was complete. The excess of protein was removed by rinsing with DDM/PBS. The SPR measuring cell was then filled with DiPhyPC/DDM/PBS and biobeads were added. The reconstitution was indicated by a further increase of reflectivity in the time range between 250 and 1750 min (Figure 5.24). The formation of the membrane was complete after roughly 25 h when the reflectivity remained constant. Rinsing with PBS did not lead to any further changes; hence the membrane was stable upon formation. However, in contrast to our earlier investigations of ptBLMs on ultra flat gold surfaces, definite thicknesses could not be deduced due to ill-defined SPR scans caused by the roughness of the surface.

EIS

The adsorption of protein and the reconstitution into the ptBLM were also monitored by EIS. Spectra of the AgNPs functionalized Ag electrode were taken after functionalizing with Ni - DTNTA (in DDM/PBS) (A), after binding of the protein (in DDM/PBS) (B) and after the reconstitution into a ptBLM (in PBS) (C). Comparison of the frequency normalized admittance plots (Figure 5.25) revealed a significant decrease in capacity due to the tethering of the protein. A further decrease was observed after reconstitution of the attached protein into the ptBLM based on DiPhyPC as the lipid component. At the same time the resistance increased upon membrane formation and reached at least 1.5 MΩ . Because of the roughness of the surface and related inhomogeneities we abstained from fitting a model circuit to the data. Hence, definite values of capacitance and resistance cannot be given. The decrease of the capacitance and the increase of the resistance, however, are

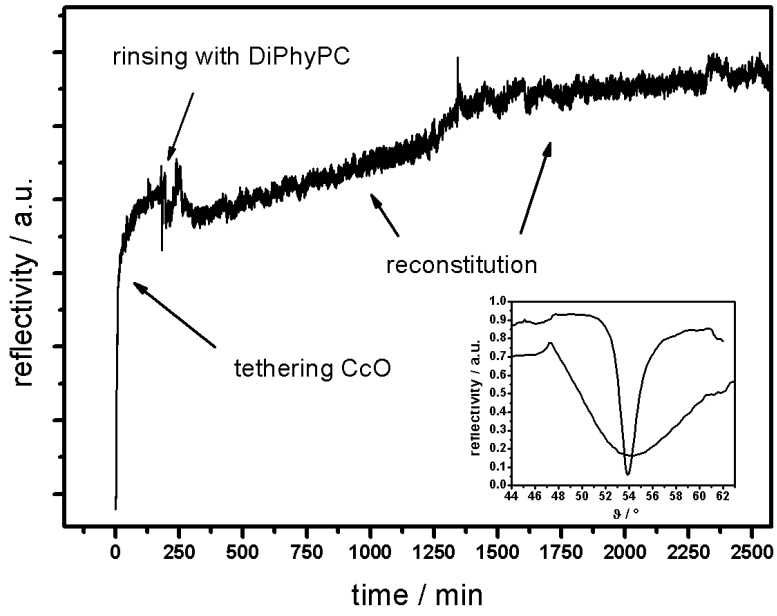

Figure 5.24: Frequency normalized admittance plots (a) and Bode plots (b) of the SERRS-active silver electrode after functionalisation with DTNTA - Ni (triangles), after adsorption of CcO (circles) and after reconstitution into the ptBLM (squares). Due to the replacement of water molecules by protein and phospho-lipids, the capacity was significantly decreased. Solid lines are provided to guide the eye.

clearly indicated as expected for the formation of the ptBLM, when detergent and water molecules around the proteins are replaced by lipid bilayer patches.

Cyclic Voltammetry (CV)

The catalytic activity of the enzyme was verified by CV. Under aerobic conditions two cathodic peaks appeared at -170 an $-410\,\mathrm{mV}$, assigned previously [20] to repeated (catalytic) electron transfer and proton translocation, respectively (Figure 5.26). Changing to anaerobic conditions (inset Figure 5.26), the electron transfer peak persisted whereas the proton transfer peak disappeared as expected [20]. However, the electron transfer peak was shifted by more than 400 mV in the negative direction vs. known midpoint potentials of the redox centers. This is exactly the same behavior as we observed previously on smooth gold (TSG) as well as on Au surfaces modified by the controlled growth of Au NPs [119]. This behavior had been considered in terms of the transformation of the CcO from a non-activated to an activated state taken as an equivalent to the resting and pulsed state of the CcO. The shift of the midpoint potentials to negative values was also confirmed by SEIRAS [119]. In the context of the present paper the CV data indicate together with the data from SPR and EIS that a well-ordered ptBLM had been formed even on the relatively rough newly developed SERRS active Ag surface. The electron transfer peak between -200 and 600 mV taken under anaerobic conditions was considerably broadened. Moreoever, the total charge calculated from the peak area amounted to $6 \pm 4 \cdot 10^{-6}$ C/cm^2, corresponding to a surface concentration of $\Gamma = 15 \pm 10$ pmol/cm^2 assuming 4 electrons transferred per protein. The errors represent the sample-to-sample deviation. On flat gold (TSG) surfaces Γ was found to be around $6\,\mathrm{pmol/cm^2}$, which corresponds to a closely packed monolayer of CcO molecules [118]. The comparatively high surface concentration together with the relatively high sample-to-sample deviation on silver electrodes can be explained in terms of the higher effective surface area caused by the AgNPs.

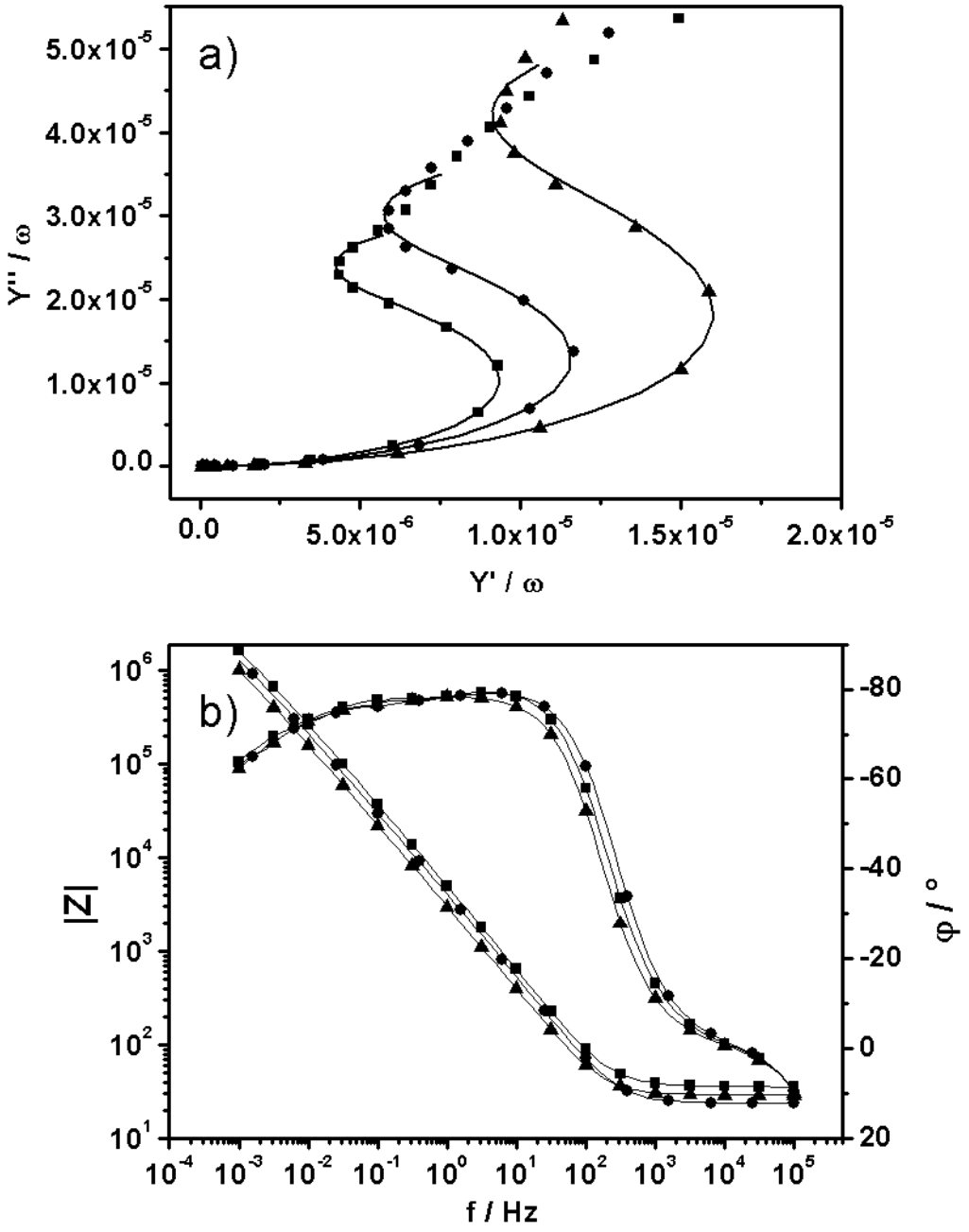

Figure 5.25: Kinetics of CcO adsorption and membrane formation on TSS modified by AgNPs followed by SPR spectroscopy at a constant angle of $\vartheta = 52°$. The inset shows the plasmon excitation angle scan of plain TSS and TSS modified by AgNPs, both showing a minimum at $\vartheta \approx 54°$. In contrast to the sharp angle scan of plain TSS, the curve is broadened after AgNP adsorption. Nevertheless, the kinetics of protein adsorption and membrane formation could be observed.

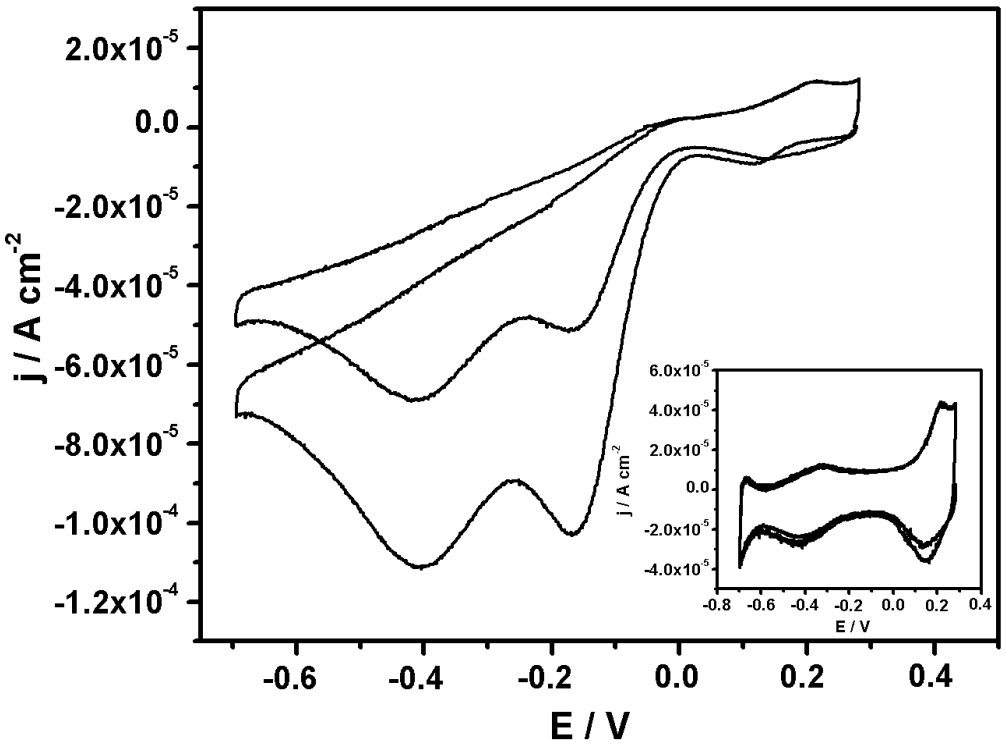

Figure 5.26: Cyclic voltammogramms of CcO under aerobic conditions. In the presence of oxygen catalytic activity of the protein is indicated by two distinctive cathodic peaks at -170 and $-410\,\mathrm{mV}$, which were previously assigned to repeated (catalytic) electron transfer and proton translocation, respectively. Under anaerobic conditions (inset) catalytic turnover is suppressed and only one peak corresponding to non-recurrent electron transfer persists.

SERRS

SERR spectra obtained with the AgNP modified substrates were well comparable or better than the spectra obtained on electrochemically roughened Ag surfaces regarding SERR-intensity and resolution. For a comparison see the earlier the publication of Friedrich et al. [20]. No averaging or smoothing was necessary. Spectra in the marker band region, between 1300 and 1700 cm^{-1} were recorded under strictly anaerobic conditions as a function of potential applied to the substrate. Starting at 200 mV the potential was varied in steps of 100 mV down to −500 mV (Figure 5.27). Heme a and heme a_3 both contributed to the intensity of the Raman scattered light in this frequency range. Bands were assignments to vibrational modes of heme a/a_3 according to Lee et al. [116]. The bands at 1359/1370cm^{-1} indicate the $\nu_{4,rd}/\nu_{4,ox}$ mode of both hemes in the reduced and oxidized state, respectively. At the most positive potential the bands at 1359 and 1370 cm^{-1} indicate that the hemes are already partially reduced. Thereafter the spectrum remained unchanged down to −100 mV. At −200 mV the peak at 1359 cm^{-1} started to increase indicating further reduction down to −400 mV where almost no contribution from an oxidized heme species was observed. A quantitative analysis was performed by deconvolution (Figure 5.28 and 5.29) of the partially overlapping SERRS peaks.

The intensities of the $\nu_{4,rd}/\nu_{4,ox}$ peaks corresponding to the relative concentration of reduced and oxidized species were plotted as a function of potential (Figure 5.30). The sigmoid function

$$I_{SERRS} = \frac{1}{1 + \exp\left[(E - E_{ip})/\varphi\right]} \tag{5.6}$$

was fitted to the data, where I_{SERRS} denotes the relative intensity of the ν_4 band at 1359 and 1370 cm^{-1}, respectively. E_{ip} is the potential of the inflection point, which reflects the midpoint potential E_m of the redox center, and φ is a scaling factor. Ideally, $\varphi = RT/F \approx 26$ mV, and $E_{ip} = E_m$ in accordance with the Nernst equation. Evaluating $\nu_{4,rd}$ revealed a midpoint potential of $E_m = -266 \pm 25$ mV and a scaling factor of $\varphi = 52 \pm 21$ mV.

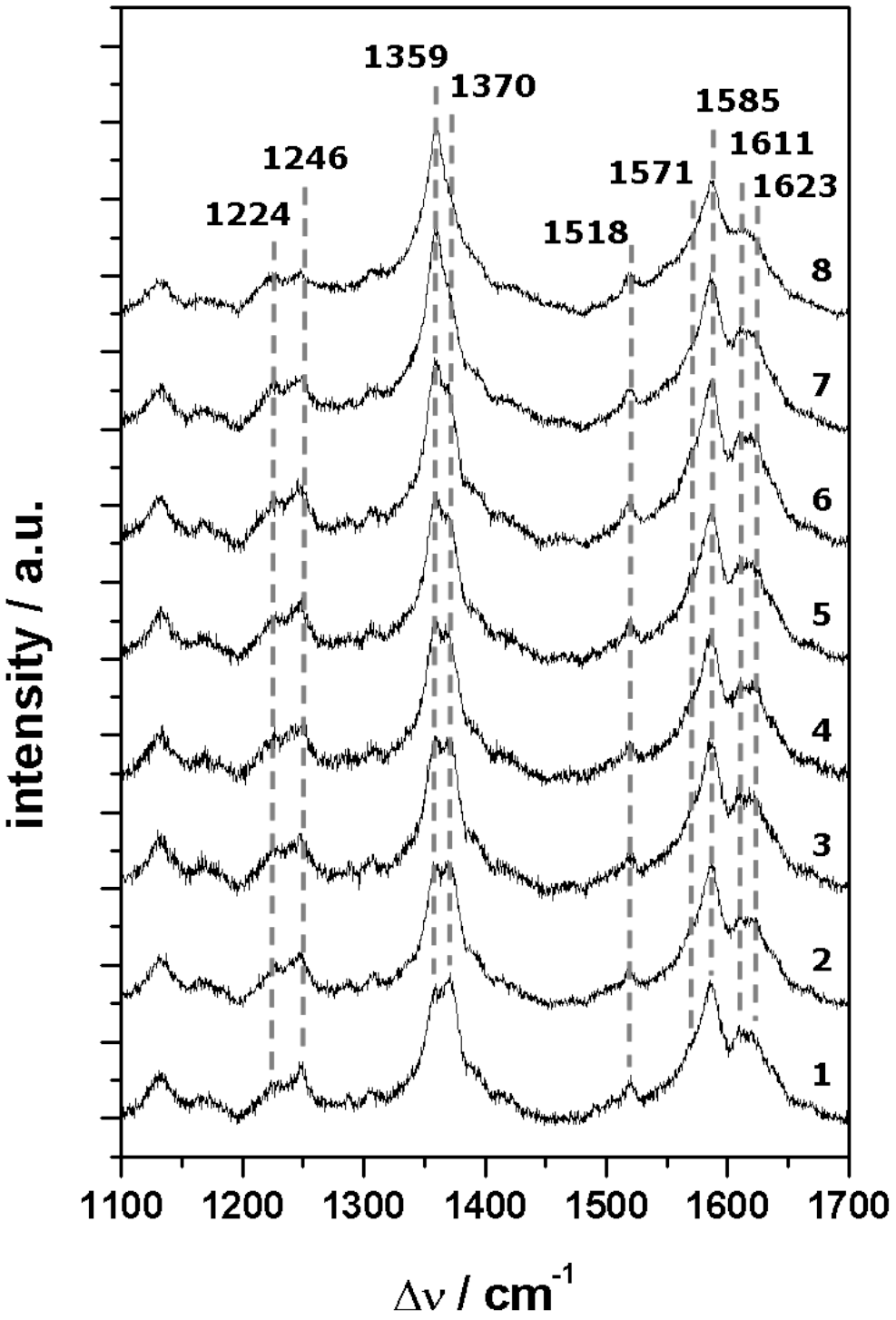

Figure 5.27: SERR spectra demonstrating the marker band region of CcO in the ptBLM recorded as a function of applied potential (E_{app}). E_{app} = 200 mV (1), 100 mV (2), 0 mV (3), −100 mV (4), −200 mV (5), −300 mV (6), −400 mV (7) and −500 mV (8) vs. NHE. The laser power was 100 µW and the accumulation time was 150 s.

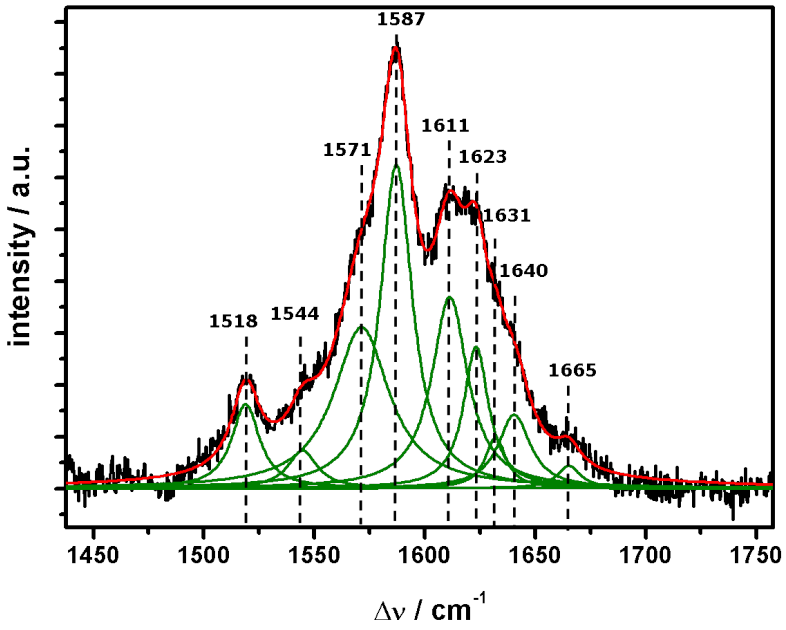

Figure 5.28: Deconvolution of the overlapping bands in the region between 1450 and 1750 cm^{-1} for the spectrum recorded at -300 mV. The band resulting from the vibrational mode ν_{11} of reduced heme a, appearing at 1518 cm^{-1} is well separated from the other strongly interfering bands.

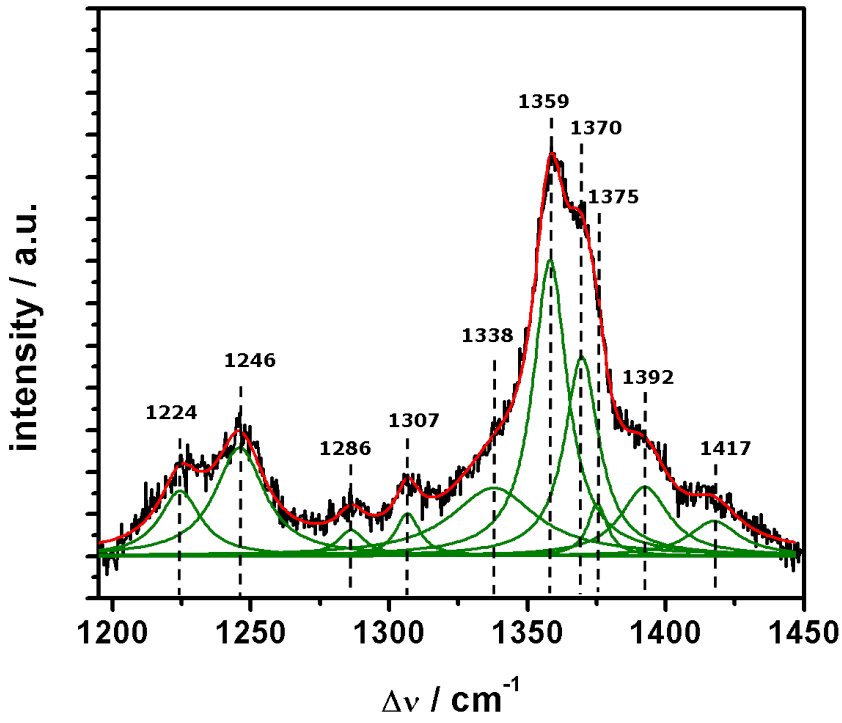

Figure 5.29: Deconvolution of the SERRS bands between 1200 and 1450 cm^{-1} for the spectrum recorded at -300 mV. Contributions from reduced ($\nu_{4,rd}$, 1358 cm^{-1}) and oxidized ($\nu_{4,ox}$, 1370 cm^{-1}) hemes were detected, while reduced species dominated.

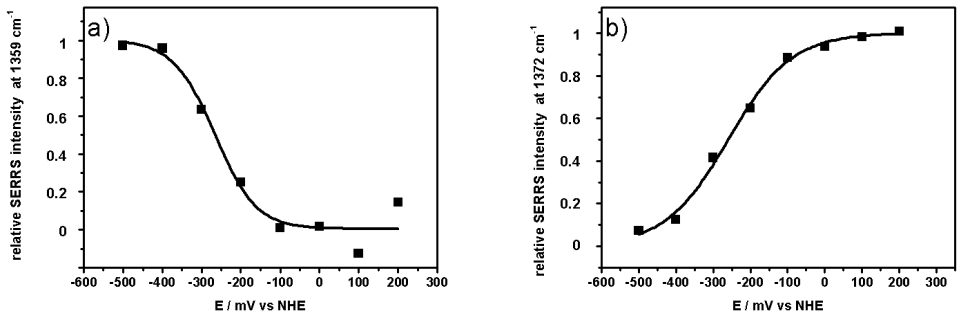

Figure 5.30: Relative SERRS intensities of $\nu_{4,rd}$ (a) and $\nu_{4,ox}$ (b) plotted as a function of E_{app}. A sigmoidal function was fitted to the data points revealing a midpoint potential $E_m = -266 \pm 25$ mV and -260 ± 14 mV, respectively.

This finding was confirmed by evaluation of $\nu_{4,ox}$ resulting in $E_m = -260 \pm 14$ mV and a scaling factor of $\varphi = 85 \pm 12$ mV. These data agree with midpoint potentials of the hemes of CcO in the activated state found by CV as well as SEIRAS and SERRS on electrochemically roughened Ag [20, 119]. Different from our previous findings the ν_4 mode showed that the hemes are already partly reduced at 200 mV, becoming gradually reduced with decreasing potentials. However, the ν_4 band does not discriminate between heme a and a_3. Other bands are more specific, for example the bands in the region between 1550 and 1650 cm^{-1}. The most prominent band in this region was found at 1587 cm^{-1} (ν_2), which was assigned to the vibration of ferrous hexacoordinated low-spin (6cLS) heme a. At the same time the contribution from high-spin heme a_3 (6cHS) observed at 1571 cm^{-1} was much weaker, indicated only by a shoulder on the left of the more intense peak at 1585 cm^{-1} due to heme a. Contributions from ν_{10}, $\nu_{C=C}$ and $\nu_{C=O}$ were found at 1640 cm^{-1}, 1623/1631 cm^{-1} and 1611/1665 cm^{-1}, respectively, with the strongest band at 1611 cm^{-1}. This band was assigned to the formyl stretching vibration $\nu_{C=O}$ of reduced heme a. In fact, there were at least nine overlapping bands within the range between 1500 and 1650 cm^{-1} (Figure fig:deconv-cco-high-wn, Table 5.4.2). Information about ligation, redox and coordination states can be derived; however the strong overlap inhibited a reliable deconvolution and a quantitative analysis of these bands. In contrast ν_{11} appearing at 1518 cm^{-1} was well separated from other peaks and assigned to the vibration of the reduced form of heme a. Heme a_3 did not contribute to this band, thus allowing us to discriminate between heme a and heme a_3 interfering at 1359/1370 cm^{-1} (ν_4). The band at 1518 cm^{-1} did not change throughout the titration. Hence, heme a remains in the reduced state in the potential range from +200 to −500 mV, whereas the intensity changes in the ν_4 band could be attributed exclusively to the reduction of heme a_3. This unexpected result was further tested by first measuring a SERR spectrum at open circuit. The ν_4 band showed the double peak, split almost equally into $\nu_{4,rd}$ and $\nu_{4,ox}$, whereas ν_{11} appeared at 1518 cm^{-1} indicating reduced heme a. Applying a potential of $E_{app} = 200$ mV did not yield any further changes, while a sudden drop of potential to −500 mV led to an increase

$\Delta\nu/\mathrm{cm}^{-1}$	mode	heme	redox
1359	ν_4	a,a_3	rd
1370	ν_4	a,a_3	oc
1518	ν_{11}	a	rd
1544	ν_{11}	a	ox
1571	ν_2	a_3	rd
1587	ν_2	a	rd
1611	$\nu_{C=O}$	a	rd
1623	$\nu_{C=C}$	a	rd
1631	$\nu_{C=C}$	a	rd
1640	ν_{10}	a	ox
1665	$\nu_{C=O}$	a_3	rd

Table 5.1: Band assignments to vibrational modes of hema a/a_3 in the reduced and oxidized form, respectively.

of the 1359 cm^{-1} ($\nu_{4,rd}$), whereas 1370 cm^{-1}($\nu_{4,ox}$) decreased almost to zero. Thus, heme a and heme a_3 were completely reduced at this potential. At the same time no changes in the intensity of ν_{11} could be identified. Changing the potential back to 200 mV resulted in a spectrum identical to the initially recorded spectrum at 200 mV. The procedure could be repeated a couple of times showing reproducible results. Hence, electron transfer from the Ag electrode to heme a_3 was shown to be fully reversible, whereas heme a remained in the reduced state within the potential range of -500 to 200 mV. This was in line with the formyl stretching vibration $\nu_{C=O}$ at 1611 cm^{-1} also indicating the reduced form of heme a throughout the potential window.

5.4.3 Conclusion

We conclude from these results that the CcO on the Ag surface modified by AgNPs was present in a mixed-valence state, in which heme a is reduced and heme a_3 is oxidized at open circuit potential. It is highly likely that heme a could also be oxidized if only we were able to apply more positive potentials. However, the range of potentials applicable to the Ag electrode is limited to +200 mV at the positive edge of the potential window, while the midpoint potential of heme a is reported to be more positive [123, 129]. That means

heme a could only be oxidized at potentials $>$ 250 mV, provided CcO is in the non-activated state. In the activated state, on the other hand, the midpoint potentials of all the redox centers were found to be shifted in the negative direction to around -200 mV; the same range that we found for oxidation/reduction of heme a_3. We conclude that the enzyme is not only in a mixed-valence state but also in a mixed-conformational state between a non-activated and an activated state. This is different from our previous experiments on electrochemically roughened Ag electrodes. Both hemes were shown to be reduced according to the SERR spectra. However, in this case a well-ordered lipid membrane was not formed around the protein and it was not catalytically active. This could be due to the much larger roughness of the conventional SERR active surface as well as an ill-controlled surface coverage in our previous experiments. Later on the linker molecule was synthesized ex-situ and self-assembled in defined mixing ratios with a dilution molecule. The kinetics of direct ET but also membrane formation was shown to critically depend on these preparation conditions. In the present study and despite of the roughness of the Ag surface the formation of a lipid membrane could be detected. The same holds for the catalytic activity of the CcO illustrating the significance of the surface architecture for electrochemical excitation. We conclude that the present result is much more reliable. Both hemes could be discriminated in the SERR spectra and reduction/oxidation of heme a_3 could be clearly demonstrated. The polished silver surface modified with AgNPs appeared to be well designed to immobilize a membrane protein such as the CcO and to reconstitute it into a ptBLM. The architecture of this substrate allowed us to perform not only surface enhanced Raman scattering, but also SPR and EIS measurements. The formation of a ptBLM was monitored by SPR and EIS. The capacity after protein immobilization and reconstitution was slightly higher compared to experiments performed on flat gold surfaces. This was considered in terms of the increase in the effective surface area. Nevertheless, a distinct decrease in capacity was observed upon membrane formation due to the replacement of water and detergent molecules by phospholipids. ($\epsilon_{lipid} \approx 2,2 < \epsilon_{CcO} \approx 30 < \epsilon_{H_2O} \approx 80$) [21, 130]. Reconstitution was also demonstrated by an increasing reflectance

in the kinetic trace of the SPR due to the same reasons. After formation of the ptBLM the enzyme showed catalytic turnover as measured by CV under aerobic conditions. Hence, the enzyme seemed to be immobilized in a stable and fully functional form. This can also be deduced from the high quality of the SERR spectra, which are known to be very sensitive to the integrity of the protein.

5.5 Electron Transfer Kinetics of Cytochrome c Oxidase Probed by Time-Resolved Surface Enhanced Resonance Raman Spectroscopy

5.5.1 Introduction

Time-resolved (TR) spectroscopic techniques have been widely used to investigate the kinetics of complex proteins such as Cytocgrome c Oxidase (CcO). These techniques include, for example, Raman, IR [131] and UV-vis [132] absorption spectroscopy. Fourier transform infrared (FTIR) spectroscopy is well designed to detect changes of amino acids and peptide structures [133, 134]. Raman spectroscopy, particularly in the Resonance Raman (RR) mode, is sensitive to redox changes of the hemes, since the $\pi - \pi^*$ electronic absorption transition selectively enhances vibrational modes of the heme structure [31, 133]. Hence changes of the redox, coordination and spin state of the central metal ion can be detected. Oxygen reduction taking place at the binuclear catalytic heme a_3-Cu_B center was probed by RR spectroscopy. Multiple oxygen-associated RR bands were observed and assigned to the different reaction intermediates of CcO [124, 135–137]. Complex setups including artificial cardiovascular systems have been used to detect and assign these bands by using oxygen isotopes [138, 139]. CcO is known to exist in at least two different states, the resting state and the pulsed state. CcO in the resting state was investigated by RR spectroscopy in the solubi-

lized form of the enzyme [133, 140, 141]. The oxygen activation was probed by TR-RR spectroscopy in whole mitochondria [142]. In the majority of cases, TR-(R)R studies concentrate on the reaction mechanism of dioxygen reduction at the catalytic binuclear center of CcO. For that purpose dioxygen reduction mechanism is initiated by photodissociation of the CO adduct of either the two-electron [132, 143, 144] or fully reduced [131, 145] CcO species. In these investigations the CO-inhibited CcO species is solubilized by a detergent, dissolved in oxygen-containing buffer solution. In order to obtain a sufficiently high signal-to-noise ratio photodissociation of the CO adduct is repeated periodically. Another possibility to initiate protein kinetics, however, less widely used, is photoinduced electron transfer (ET) to CcO [146, 147]. These techniques employ the CcO in either in solubilized form in solution or else in partially dried lipid-enriched layers immobilized on an ATR crystal. By contrast we have introduced direct electron transfer from an electrode into the enzyme via the first electron acceptor, Cu_A to initiate the sequential ET along the four redox centers Cu_A, heme a, heme a_3 and Cu_B, thus mimicking the natural tunnel pathway through the protein. For this purpose, CcO from Rhodobacter sphaeroidis is immobilized in a unidirectional fashion to the SERR-active Ag surface using his-tag technology. The protein is then reconstituted by in-situ dialysis into a protein tethered bilayer lipid membrane (ptBLM) [20, 21, 75]. In our previous surface enhanced resonance Raman (SERR) study [148] signals obtained on Ag electrodes modified by silver nanoparticles (AgNPs) proved to be sensitive enough to detect reduction/oxidation of the heme structures within monolayers of CcO embedded into a ptBLM. At the same time the Ag surface can be used as an electrode for electrochemical excitation. Potentiometric titrations showed the enzyme to be present in a mixed-valence state under open circuit conditions. Heterogeneous electron transfer between CcO and substrate was electrochemically controlled by applying static potentials between 200 mV and −500 mV. Characteristic changes in the spectra were observed and identified with redox transitions of heme a_3 [148], while heme a remained in the reduced state throughout. In the present investigation this technology is extended into the time domain by applying periodic potential pulses. In

this way redox transitions of the hemes can be observed by TR-SERRS in-situ undergoing non-recurrent or catalytic ET. The enzyme had been shown to be catalytically active under our experimental conditions [20, 119, 148]. However, the present study concentrates on ET in a strictly anaerobic environment. The kinetics of direct ET to heme a_3 will be elucidated using different mathematical approaches. Recently we derived a model describing sequential ET into multi-redox center proteins such as CcO [118]. This model was modified to become consistent with the properties of the mixed-valence state of CcO. Using this model allowed us to derive electrochemical rate constants together with the standard potential of heme a_3.

5.5.2 Results

Time-resolved (TR) experiments probing CcO in the ptBLM architecture (Figure 5.31) were performed under strictly anaerobic conditions, hence catalytic turnover was inhibited. TR spectra were recorded by application of periodic potential pulses stepping between the initial potential E_i and the final potential E_f with the frequency f_p. Synchronized Raman excitation with a delay time δt after stepping from E_i to E_f was achieved using laser pulses with the length Δt. Observation of time-resolved reduction and oxidation was achieved by choosing $E_i = 200\,\mathrm{mV}$, $E_f = -500\,\mathrm{mV}$ and $E_i = -500\,\mathrm{mV}$, $E_f = 200\,\mathrm{mV}$, respectively. The marker band region between 1300 and 1700 cm^{-1} was observed, thereby focusing attention on the porphyrin ring modes $\nu_{4,rd}/\nu_{4,ox}$ and ν_{11} at 1359/1370 cm^{-1} and 1518 cm^{-1}, respectively. Formyl stretching $\nu_{C=O}$ of reduced heme a at 1611 cm^{-1} was also observed. CcO under open circuit conditions and at all positive potentials up to 200 mV and had been found earlier to be present in a mixed valence state, with heme being reduced, while heme a_3 was oxidized. Reduction of heme a_3 was achieved at a midpoint potential of $E_m = -266\,\mathrm{mV}$ [148] (Section 5.4). It was shown that the midpoint potential of heme a remained at around 230 mV according to literature values, while that of heme a_3 was shifted to negative values. Such a shift was found to be characteristic of the transformation of CcO into an activated state. Considering the wide potential range, TR-SERR

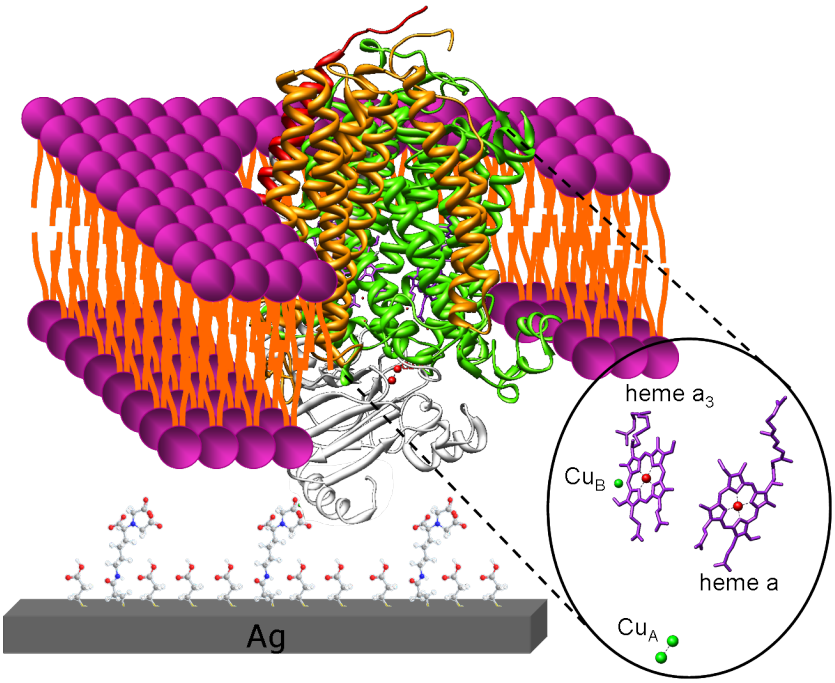

Figure 5.31: CcO immobilized in a ptBLM on a silver electrode. A his-tag anchor attached to subunit II of CcO yields an orientation with the cytochrome c binding site directed towards the electrode, therefore direct electron transfer to Cu_A is achieved.

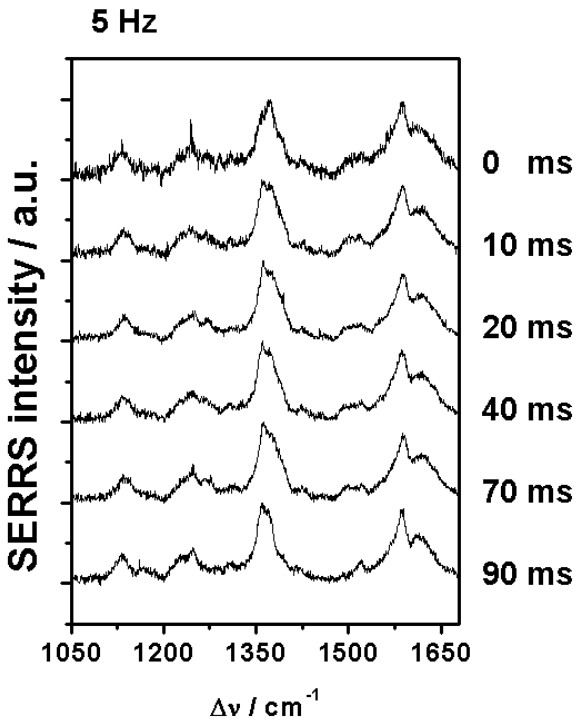

Figure 5.32: TR-SERRS spectra of CcO in a ptBLM; $f_p = 5$Hz. The changes in the band ν_4 were identified with the changes of the redox state of heme a_3. Most significant changes were observed between 0 and 10 ms.

spectra were recorded using potential pulses in the range between +200 and −500 mV.

In order to monitor the time-dependent redox changes an appropriate frequency f_p must be chosen which is fast enough to capture the essential changes in the spectra and slow enough to allow for a sufficiently high number of data points. At first $f_p = 5$ Hz and $\Delta t = 10$ ms was used. The series of spectra is depicted in Figure 5.32. Band fitting was performed as described in Section 5.4 to identify peak intensities of the bands $\nu_{4,rd}$ and $\nu_{4,ox}$, which correspond to the concentrations of reduced and oxidized hemes, respectively. Relative concentrations were plotted as a function of time. The plot is characterized by a sharp drop of intensity of the $\nu_{4,ox}$ band, indicating a reduction process which is fast compared to $f_p = 5$ Hz. In a second

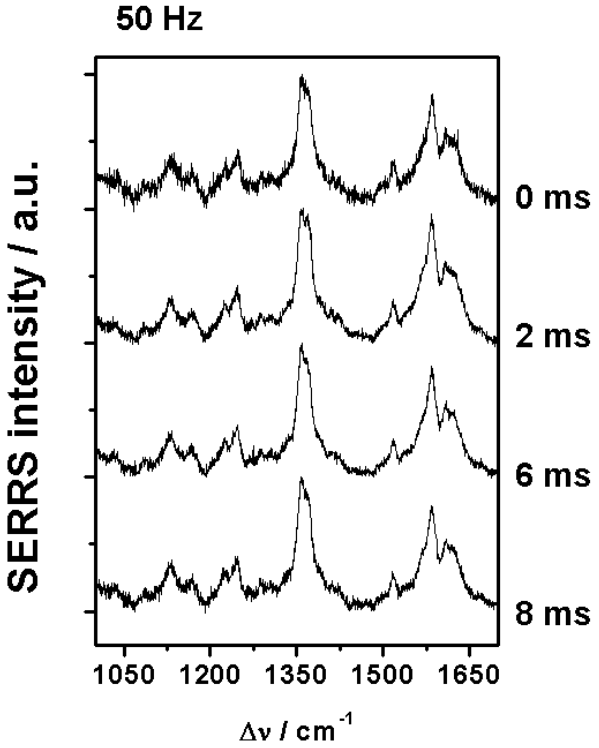

Figure 5.33: TR-SERRS spectra of CcO in a ptBLM; $f_p = 50$ Hz. Changes in the band ν_4 were rather small and continuous over the observed period of time, indicating an electron transfer rate which is low compared to the excitation frequency.

experiment, $f_p = 50$ Hz and $\Delta t = 2$ms were used in order to resolve the reduction process in more detail. Spectra after δt = 0, 2, 6 and 8 ms are depicted in Figure 5.33. The band ν_4 shows that the hemes did not become fully oxidized and reduced at this frequency and changes in the intensities of $\nu_{4,rd}$ and $\nu_{4,ox}$ were much smaller. Hence, plotting the relative intensities as a function of time led to flat curves mirroring the fractional changes in the redox state. Further, oxidation was probed time resolved with $f_p = 10$ Hz and $\Delta t = 5$ ms. At this frequency the enzyme reached the fully reduced state at $\delta t = 0$ ms. Spectra taken at $\delta t = 5$, 10, 25 and 45 ms illustrate the time-dependent changes (Figure 5.34).

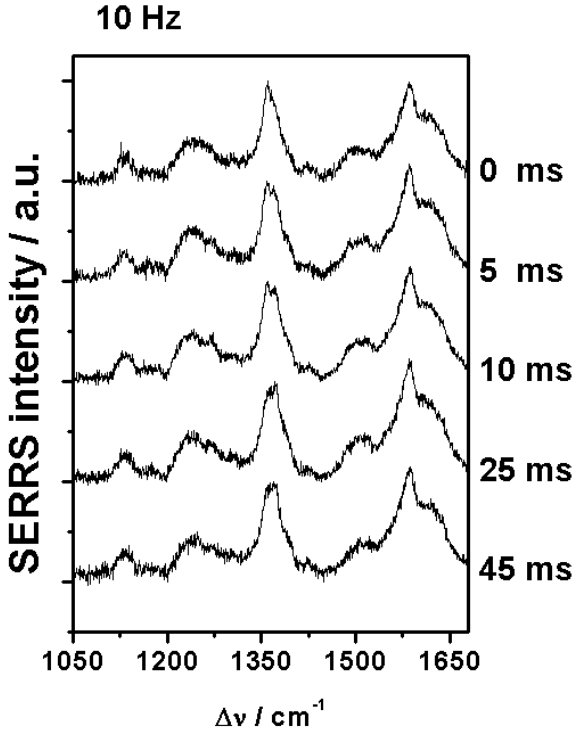

Figure 5.34: TR-SERRS spectra of CcO in a ptBLM; $f_p = 10$Hz. At this particular frequency the time-dependent changes of the redox state are captured much more accurately compared to $f_p = 5$ Hz and $f_p = 50$ Hz.

frequency band	5 Hz		10 Hz		50 Hz	
	$\nu_{4,rd}$	$\nu_{4,ox}$	$\nu_{4,rd}$	$\nu_{4,ox}$	$\nu_{4,rd}$	$\nu_{4,ox}$
$k/(s^{-1})$	237 ± 175	140 ± 55	143 ± 30	135 ± 47	113 ± 154	308 ± 355
$k/(s^{-1})$	185 ± 175		138 ± 26		272 ± 183	
$k/(s^{-1})$	158 ± 26					

Table 5.2: Potential dependent rate constants derived using different excitation frequencies f_p.

Data analysis by fitting mono-exponential functions

As a first approximation single exponential functions were fitted to the TR-SERRS data. The fit-function is described by

$$\Delta int(t) = \Delta int_{max} \left[1 - \exp(-kt)\right] + \Delta int_0 \tag{5.7}$$

where Δint(t) is defined as

$$\Delta int(t) = int(t) - int(0). \tag{5.8}$$

Δint_{max} is the maximal intensity change, and Δ int_0 is a correction term accounting for the experimental error of the reference intensity int(0). When fitting parameter values, first an individual k was fitted for each frequency f_p and band ($\nu_{4,rd}$ and $\nu_{4,ox}$). Then a common k for each frequency was derived and finally a common k for all frequencies. The results are presented in Table 5.5.2. In Figure 5.35 the SERRS intensities of the bands $\nu_{4,rd}$ and $\nu_{4,ox}$ are depicted for each frequency f_p together with the fitted curves. Figure 5.36 shows the same data but as an overlay of the three frequencies for better comparison.

Electrochemical rate constants: deriving k_0

Fitting single exponential functions according to Equation 5.7 does not take into account that the effective rate constant k, significantly depends on potentials applied relative to the standard potential of the redox couple. Coupled chemical reactions can further affect the ET rates. Therefore, a sequential

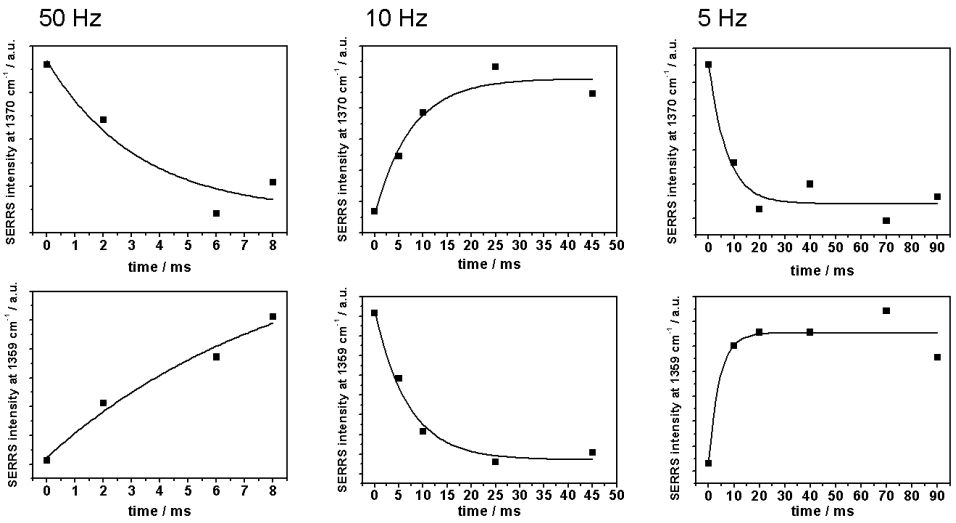

Figure 5.35: SERRS peak intensities of $\nu_{4,rd}$ and $\nu_{4,ox}$ plotted as a function of delay time δt (squares) compared to the fitted mono-exponential function (solid line).

4-electron transfer model was developed in our group by to account for ET to the CcO under anaerobic conditions, starting with the fully oxidized CcO [118]. This model is not applicable to the present experiment since it starts with heme a in the oxidized state, while in this case redox changes of heme a_3 were observed with heme a present in the reduced form. Hence electrochemical kinetics are treated in terms of a one-electron transfer model, using the following equations for a redox couple adsorbed to an electrode:

$$dp_{rd}/dt = -dp_{ox}/dt = k_f p_{ox}(t) - k_b p_{rd}(t) \tag{5.9}$$

with

$$p_{rd}(t) + p_{ox}(t) = 1. \tag{5.10}$$

Here p_{rd} and p_{ox} denote the probabilities of the reduced and oxidized states, respectively. The forward and backward rate coefficients in Equation 5.9 are potential-dependent according to

$$k_f = k_0 \exp\left[-(E - E_0)/2\varphi_0\right] \quad with \quad \varphi_0 = RT/F \tag{5.11}$$

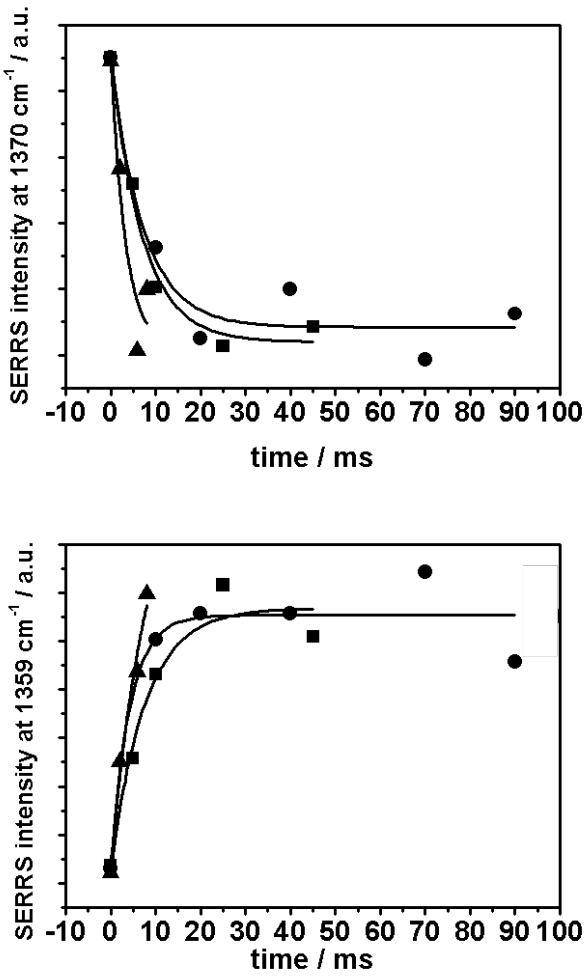

Figure 5.36: An overlay of the progress of the SERRS intensities at $f_p = 5\,\mathrm{Hz}$ (circles), 10 Hz (squares) and 50 Hz (triangles). Even though the excitation frequency was significantly varied the response of the redox center was approximately constant as expected.

and

$$k_b = k_0 \exp\left[(E - E_0)/2\varphi_0\right] \quad with \quad \varphi_0 = RT/F. \tag{5.12}$$

k_0 is the electrochemical rate constant, while E and E_0 denote the applied and the standard potential, respectively. If the charging of the surface is much faster than the electron uptake the charging current can be disregarded, and the kinetics initiated by a potential jump can be described as follows.

reduction process

A high oxidizing potential $E_{ox} > E_0$ is initially applied ($E_i = E_{ox}$) and then instantaneously changed to a low reducing potential $E_{rd} < E_0$ ($E_f = E_r d$), hence $k_b << k_f$ (see Equation 5.11 and 5.11) and can be disregarded. It then follows from Equation 5.9

$$dp_{ox}/dt \approx -k_f p_{ox}(t) \quad and \quad o_{ox}(t) = \exp(-k_f t) \tag{5.13}$$

Hence by means of $p_{rd}(t) = 1 - o_{ox}$ and noting that $p_{rd}(0) = 0$ it follows

$$p_{ox}(t) - p_{ox}(0) = -\left[1 - \exp(-k_f t)\right] \quad and \quad p_{rd}(t) - p_{rd}(0) = 1 - \exp(k_f t). \tag{5.14}$$

Comparing Equation 5.14 with Equation 5.7 shows that

$$k_{ox\to rd} = k_{0,ox\to rd} \exp\left[-(E_{rd} - E_0)/2\varphi_0\right] \tag{5.15}$$

where $k_{ox\to rd}$ and $k_{0,ox\to rd}$ denote, respectively k in Equation 5.7 and k_0 in Equation 5.11 for ox $\to$ rd.

oxidation process

On the analogy of the reduction process, it follows that

$$k_{rd\to ox} = k_{0,rd\to ox} \exp\left[(E_{ox} - E_0)/2\varphi_0\right] \tag{5.16}$$

where $k_{rd\rightarrow ox}$ and $k_{0,rd\rightarrow ox}$ denote, respectively k in Equation 5.7 and k_0 in Equation 5.11 for rd $\rightarrow$ ox. Assuming $E_0 = -266$ mV, as derived by static SERRS (Section 5.4) under otherwise exactly the same conditions, $k_{0,rd\rightarrow ox}$ and $k_{0,ox\rightarrow rd}$ can be calculated using Equations 5.15 and 5.16. It was assumed that $k_{0,ox\rightarrow rd} = k_{0,rd\rightarrow ox}$. The data is presented in Table 5.5.2.

Model fitting: deriving a common E_0 and k_0

Model fitting of TR-SERRS data was performed by a co-operation partner, XXX, in Basel.

It was assumed that $k_{0,ox\rightarrow rd} = k_{0,rd\rightarrow ox}$. Moreover, the rate constants k and k_0 are considered independent from the frequency f_p used for excitation. Therefore it is reasonable to fit an electron transfer model to the data of the reduction and oxidation process simultaneously. This model is described by Equations 5.9, 5.11 and 5.12. Moreover

$$\Delta int(t) = \Delta int_{max} \left[p_{rd/ox}(t) - p_{rd/ox}(0) \right]. \tag{5.17}$$

The charging current of the surface was taken into account by using time constants between $\tau = 0.1$ and 0.01 ms. However no significant differences in the fit results were observed. Therefore only the case with 0.01 ms is presented here (Figure 5.37). The correction term Δint_0 (Equation 5.7) was rather small, and was therefore disregarded. This method is preferable since it offers the possibility of fitting a common k_0 by using the whole data set obtained at different excitation frequencies f_p, simultaneously. Given the fact that at least one frequency was used to measure the reverse electron transfer direction, not only a common k_0, but also a common E_0 can be derived. The fit results are given in Table 5.5.2.

5.5.3 Conclusion

TR-SERRS using periodic potential pulses of different frequencies showed time traces varying systematically with time, independent of the excitation frequency f_p. 10 Hz proved to be the best in terms of number of data points

frequency band	5 Hz		10 Hz		50 Hz	
	$\nu_{4,rd}$	$\nu_{4,ox}$	$\nu_{4,rd}$	$\nu_{4,ox}$	$\nu_{4,rd}$	$\nu_{4,ox}$
$k_0/(\mathrm{s}^{-1})$	2.49 ± 1.84	1.46 ± 0.57	0.016 ± 0.003	0.015 ± 0.005	1.41 ± 1.92	3.11 ± 3.59
$k_0/(\mathrm{s}^{-1})$	1.96 ± 0.71		0.016 ± 0.003		2.78 ± 1.86	

Table 5.3: Electrochemical rate constants derived using different excitation frequencies f_p.

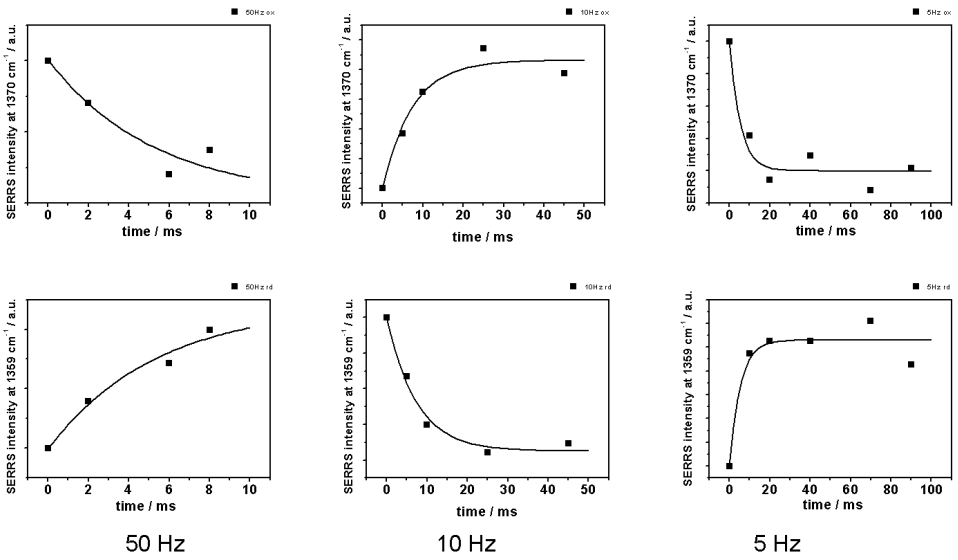

Figure 5.37: Simultaneously fitted curves (5, 10, and 50Hz) together with the corresponding TR-SERRS data. As a result a common standard potential and rate constant of the the redox center heme a_3 was obtained, amounting to $E_0 = (-142 \pm 8)$ mV and $k_0 = (0.183 \pm 0.028)\ \mathrm{s}^{-1}$, respectively.

frequency band	5 Hz		10 Hz		50 Hz	
	$\nu_{4,rd}$	$\nu_{4,ox}$	$\nu_{4,rd}$	$\nu_{4,ox}$	$\nu_{4,rd}$	$\nu_{4,ox}$
$E_0/(\mathrm{mV})$	-142.0 ± 7.8					
$k_0/(\mathrm{s}^{-1})$	0.183 ± 0.028					

Table 5.4: Electrochemical rate constant k_0 and standard potential E_0 as derived by fitting an electron transfer model to the data set obtained at different frequencies f_p, simultaneously.

and distribution within the time window. As a first approximation, time traces were evaluated using single exponentials. An effective rate constant $k = (158 \pm 26)\,\mathrm{s}^{-1}$ was achieved applying -500 and 200 mV as a reductive and oxidative potential, respectively. This rate constant is mainly dominated by the applied overpotential and therefore does not represent an intrinsic property of the protein. However, it is a characteristic of the ptBLM system on the silver substrate and mirrors the maximum transfer rate which can be reached using this architecture. This ET rate is fast compared to the finding of Hrabakova et al. [70]. In this case CcO that had been determined recently by TR-SERRS to be as slow as $0.002\,\mathrm{s}^{-1}$ on a similar surface architecture. However, in this case ET was nonspecific with respect to the orientation of the CcO. Moreover, a catalytic current was not demonstrated and the effect of the potential was not taken into account. The authors considered their data in terms of long distance ET directly to the hemes. By contrast, under the experimental conditions used in this work four electrons are injected into the protein via Cu_A, provided it was immobilized with Cu_A directed toward the electrode [118]. In order to achieve this goal, we had to consider that the activity of the tethered protein strongly depends on the packing density of the surface layer [62]. Therefore, the slow ET rate reported by Hrabakova et al. [70]is more likely due to a high packing density.

In a second step the influence of the potential was taken into account using Equations 5.15 and 5.16, which permitted the electrochemical rate constant k_0 to be determined. For the reduction process the rate constant was derived to be in the range of $k_0 = 2\,\mathrm{s}^{-1}$, while the rate constant for the oxidation process was determined to be $k_0 = 0.016\,\mathrm{s}^{-1}$, however assuming $E_0 = -260\,\mathrm{mV}$ as derived by potentiometric titration using SERRS (Section 5.4). Using the more advanced approach of fitting an electron transfer model to different excitation frequencies, a common E_0 and k_0 was derived. This method is considered to be more reliable, since the unrealistic discrepancy between the forward and backward rate constants could be avoided. The standard potential and rate constant was found to be $E_0 = (-142.0 \pm 7.8)\,\mathrm{mV}$ and $k_0 = (0.183 \pm 0.028)\,\mathrm{s}^{-1}$, respectively. The electrochemical rate constant k_0 obtained from the TR SERRS data, however, is slow compared to $370\,\mathrm{s}^{-1}$

obtained by fast-scan voltammetry for the enzyme in the fully activated state [118]. This is explained by the fact that the enzyme was not completely activated prior to the measurement using the procedure described before [119]. In a final analysis it can be concluded that in this state CcO is characterized by hampered ET to the center heme a_3. Therefore, TR-SERRS proved to be a good choice to identify electron transfer rates to heme a_3 of CcO.

Chapter 6

Final Conclusion

Electronic wiring in combination with surface enhanced infrared absorption spectroscopy (SEIRAS) had revealed that Cytochrome c Oxidase (CcO) can exist in a non-activated and activated state, which was considered equivalent to the resting and pulsed state, discovered by biochemical assays, respectively. The activated state was characterized by a shift of the midpoint potentials of the redox centers to values around $-200\,\mathrm{mV}$, whereas in the non-activated state they were in the range between 200 and 300 mV, known from biochemical assays. Spectro-electrochemical investigations using SERRS revealed that in addition an intermediate state exists in which the midpoint potential of heme a_3 is shifted in the negative direction while the midpoint potential of heme a remains at around 230 mV according to literature values. This finding was achieved on the basis of significant improvements of the experimental conditions for SERRS and the implementation of the protein tethered bilayer lipid membrane (ptBLM) on a specially developed SERRS substrate.

At first a measuring cell was designed, which enabled highly sensitive time-resolved (TR) SERRS using low power excitation. The drive shaft turned out to be the most crucial element of the construct. It was manufactured extremely precisely so as to keep the top plane of the silver electrodes in the focal plane of the confocal Raman microscope even at a rotating speed of 800 revolutions per minute. At the same time permanent electrical con-

tact to the silver electrode was achieved by manufacturing the drive shaft using a core / cladding principle. The outer cladding was made from steel providing mechanical stability. A conductive bolt served as the inner core and was connected on one side to the mobile part of a mercury contact and on the other side to the working electrode. The bolt was separated from the cladding by insulating glue. A dynamic seal was utilized to seal the liquid reservoir into which the rotating shaft extended from the cell body. The lid into which the microscope objective extended was equipped with feed pipes for gas (oxygen or argon) and buffer solution as well as the reference and counter electrode. The concept proved to be much more reliable than previous approaches which had problems with leaking of the rotating liquid reservoir and with wobbling of the electrode, leading to an unsteady Raman signal. The quality of the Raman spectra was significantly improved with respect to the constancy of the SERRS intensity.

Electron transfer kinetics of cytochrome c was probed by time-resolved surface enhanced resonance Raman spectroscopy using the newly designed measuring cell. Using a self-assembled monolayer of mercaptoethanol as spacer layer between silver electrode and protein led to an adsorption of cytochrome c with the heme cleft directed away from the silver electrode. SERR spectra were taken showing bands assigned to vibrational modes of the heme's porphyrine ring. Depending on the redox state of the central iron ion, the prominent ν_4 band was observed at 1361 (Fe^{2+}) and 1374 cm^{-1} (Fe^{3+}). Spectra were recorded as a function of applied potential. This allowed to monitor the potential dependent electron transfer between functionalized silver electrode and cytochrome c. The quality of the Raman spectra allowed to identify the measured band intensities with the relative concentrations of reduced / oxidized species of cytochrome c. Plotting the relative concentrations as a function of the applied potential revealed a Nernst-characteristic. Time-resolved SERRS was performed, which allowed the time-dependent evolution of reduction and oxidation of the heme center to be observed. The time constants for reduction and oxidation were derived from SERRS to be $k_{ox} = (46 \pm 7)\ s^{-1}$ and $k_{rd} = (84 \pm 20)\ s^{-1}$. Therefore it was deduced that in this case the orientation of cytochrome c with the heme cleft pointing

away from the electrode hampers electron transfer. Furthermore this investigation proved the reliability of the measuring cell and the concept used for time-resolved SERR experiments.

Silver electrodes roughened by repeated oxidation reduction cycles were used for probing electron transfer kinetics of cytochrome c by SERRS. The fractal structure of this surface resulted in increased Raman intensities due to the surface enhancement effect. Surface enhancement is based on the excitation of localized surface plasmons within the irregularities of the rough silver. However, the surface resulting from this method was full of fissures and was characterized by a coral-like structure. Hence the surface was not compatible with an unidirectional attachment of cytochrome c oxidase and a proper membrane formation around the protein. A novel surface architecture was developed which fostered the formation of a protein tethered bilayer lipid membrane. For that purpose flat silver substrates were modified by controlled adsorption of silver nanoparticles. The ex situ prepared nanoparticles showed localized surface plasmon resonance at 409 nm which was well in line with the wavelength of 413 nm used for resonance Raman excitation. Cytochrome c was used as a benchmark system for evaluating the magnitude of surface enhancement. Comparing the amount of nanoparticles per surface area with the SERRS intensity of cytochrome c revealed that the maximum intensity was not reached for highest nanoparticle coverage. In fact particles arranged in clusters did not contribute to the surface enhancement. The resonance frequency of clusters was shown to be shifted to higher wavelengths due to coupling effects of surface plasmons. Surfaces with the highest concentration of silver nanoparticles separated from each other led to highest Raman intensities. On that basis the immersion time of silver electrodes in the nanoparticle suspension was optimized. Finally the novel SERRS substrate exhibited an enhancement factor of up to $EF = 10^5$. Compared to conventional SERRS substrates the enhancement was increased by a factor of five.

The ptBLM was implemented on the nanoparticle modified silver substrates. Tethering of Cytochrome c Oxidase and membrane formation was monitored by surface plasmon resonance (SPR) spectroscopy and electro-

chemical impedance spectroscopy (EIS). The angle-dependent plasmon excitation curve revealed broadened excitation compared to smooth silver substrates such as template stripped silver. The reason was considered to be interactions between the evanescent surface plasmon and localized surface plasmons. Nevertheless SPR kinetics could be used to demonstrate CcO adsorption kinetics and membrane formation around the nanoparticles. Cyclic voltammetry revealed catalytic turnover in the presence of oxygen. Enzymatic activity was suppressed under anaerobic conditions. Electrochemically induced electron transfer was investigated by SERRS. The midpoint potential of heme a_3 was determined to be $E_m = (-260 \pm 15)\,\mathrm{mV}$, whereas heme a was shown to be reduced at open circuit potential and within the potential window +200 to $-500\,\mathrm{mV}$. It was concluded that heme a had preserved the midpoint potential ($E_m = -260\,\mathrm{mV}$) of the non-activated form, while the midpoint potential of heme a_3 was shifted to negative values. This mixed-valence state was considered as an intermediate between the fully activated and non-activated state. Hence, the ptBLM system was established on a SERRS active substrate enabling direct electron transfer to the catalytic center heme a_3-Cu_B.

As a consequence of the advanced SERRS measuring cell, the novel nanostructured silver substrate and the establishment of the ptBLM on such surfaces, electron transfer to the catalytic center of CcO could be monitored by TR-SERRS. Triggering electron-transfer by electrochemical potential pulses between 5 and 50 Hz revealed a time constant for the reduction of heme a_3, which was independent from the excitation frequency f_p. The rate constant derived from fitting single exponential functions to the data resulted in an average value $k = 160\,\mathrm{s}^{-1}$ at a potential of $-500\,\mathrm{mV}$ applied to the electrode.

In an advanced approach an electrochemical one-electron transfer model was fitted to the TR-SERRS data, simultaneously for all excitation frequencies f_p. The model comprises the potential dependence of the rate constant according to the Butler-Volmer equation. Further the charging current due to the rearrangement of charges on the interface was taken into account. As a result the electrochemical rate constant and the standard potential were derived and found to be $k_0 = 0.2\,\mathrm{s}^{-1}$ and $E_0 = -140\,\mathrm{mV}$, respectively. The

electrochemical rate constant k_0 obtained from the time-resoved SERRS data, however, is low compared to $370\,s^{-1}$ obtained by fast-scan voltammetry and TR-SEIRAS for the enzyme in the fully activated state. It was concluded, that the not fully activated form of CcO is characterized by hampered electron transfer to the center heme a_3.

There are indications from TR-SEIRAS that k_0 of the non-activated state of CcO is much lower than $k_0 = 0.2\,s^{-1}$. Even though a definite value could not be assigned on the basis of TR-SEIRAS, the value of $k_0 = 0.2\,s^{-1}$ of the intermediate form perfectly fits into the picture of the non-activated state gradually being transferred into the fully activated state.

List of Figures

List of Tables

Bibliography

[1] P. Rich. The cost of living. *Nature*, 421(6923):583–583, 2003.

[2] R. A. Reid, J. Moyle, and P. Mitchell. Synthesis of adenosine triphosphate by a protonmotive force in rat liver mitochondria. *Nature*, 212 (5059):257–&, 1966.

[3] C. A. Varotsis and G. T. Babcock. Photolytic activity of early intermediates in dioxygen activation and reduction by cytochrome-oxidase. *Journal Of The American Chemical Society*, 117(45):11260–11269, November 1995.

[4] T. Tsukihara, H. Aoyama, E. Yamashita, T. Tomizaki, H. Yamaguchi, K. ShinzawaItoh, R. Nakashima, R. Yaono, and S. Yoshikawa. The whole structure of the 13-subunit oxidized cytochrome c oxidase at 2.8 angstrom. *Science*, 272(5265):1136–1144, 1996.

[5] S. Iwata, C. Ostermeier, B. Ludwig, and H. Michel. Structure at 2.8-angstrom resolution of cytochrome-c-oxidase from paracoccus-denitrificans. *Nature*, 376(6542):660–669, 1995.

[6] M. K. F. Wikstrom. Proton pump coupled to cytochrome-c oxidase in mitochondria. *Nature*, 266(5599):271–273, 1977.

[7] J.M. Berg, J.L. Tymoczko, and L. Stryer. *Biochemistry*. W.H. Freeman and Company - New York, 2006.

[8] M. Svensson-Ek, J. Abramson, G. Larsson, S. Tornroth, P. Brzezinski, and S. Iwata. The x-ray crystal structures of wild-type and eq(i-286)

mutant cytochrome c oxidases from rhodobacter sphaeroides. *Journal Of Molecular Biology*, 321(2):329–339, 2002.

[9] S. FergusonMiller and G. T. Babcock. Heme/copper terminal oxidases. *Chemical Reviews*, 96(7):2889–2907, November 1996.

[10] T. Kitagawa and T. Ogura. Oxygen activation mechanism at the binuclear site of heme-copper oxidase superfamily as revealed by time-resolved resonance raman spectroscopy. *Progress In Inorganic Chemistry, Vol 45*, 45:431–479, 1997.

[11] H. Michel, J. Behr, A. Harrenga, and A. Kannt. Cytochrome c oxidase: Structure and spectroscopy. *Annual Review Of Biophysics And Biomolecular Structure*, 27:329–356, 1998.

[12] H. Michel. Cytochrome c oxidase: Catalytic cycle and mechanisms of proton pumping-a discussion. *Biochemistry*, 38(46):15129–15140, November 1999.

[13] G. Antonini, F. Malatesta, P. Sarti, and M. Brunori. Proton-pumping by cytochrome-oxidase as studied by time-resolved stopped-flow spectrophotometry. *Proceedings Of The National Academy Of Sciences Of The United States Of America*, 90(13):5949–5953, July 1993.

[14] V. Y. Artzatbanov, A. A. Konstantinov, and V. P. Skulachev. Involvement of intra-mitochondrial protons in redox reactions of cytochrome-a. *Febs Letters*, 87(2):180–185, 1978.

[15] R. W. Hendler, K. Pardhasaradhi, B. Reynafarje, and B. Ludwig. Comparison of energy-transducing capabilities of the 2-subunit and 3-subunit cytochromes aa3 from paracoccus-denitrificans and the 13-subunit beef-heart enzyme. *Biophysical Journal*, 60(2):415–423, August 1991.

[16] P. Brzezinski and R. B. Gennis. Cytochrome c oxidase: exciting progress and remaining mysteries. *Journal Of Bioenergetics And Biomembranes*, 40(5):521–531, 2008. Times Cited: 14.

[17] R. M. Kluck, E. BossyWetzel, D. R. Green, and D. D. Newmeyer. The release of cytochrome c from mitochondria: A primary site for bcl-2 regulation of apoptosis. *Science*, 275(5303):1132–1136, 1997.

[18] D. R. Green and J. C. Reed. Mitochondria and apoptosis. *Science*, 281 (5381):1309–1312, 1998.

[19] S. Tan, H. T. Tan, and M. C. M. Chung. Membrane proteins and membrane proteomics. *Proteomics*, 8(19):3924–3932, October 2008.

[20] M. G. Friedrich, J. W. F. Robertson, D. Walz, W. Knoll, and R. L. C. Naumann. Electronic wiring of a multi-redox site membrane protein in a biomimetic surface architecture. *Biophysical Journal*, 94(9):3698–3705, May 2008.

[21] F. Giess, M. G. Friedrich, J. Heberle, R. L. Naumann, and W. Knoll. The protein-tethered lipid bilayer: A novel mimic of the biological membrane. *Biophysical Journal*, 87(5):3213–3220, November 2004.

[22] C. V. Raman and K. S. Krishnan. A new type of secondary radiation. *Nature*, 121:501–502, January 1928.

[23] D. A. Long. *The Raman Effect: A Unified Treatment of the Theory of Raman Scattering by Molecules*. John Wiley & Sons, 2002.

[24] R. Aroca. *Surface-Enhanced Vibrational Spectroscopy*. John Wiley & Sons Ltd., 2006.

[25] W. Smith and G. Dent. *Modern Raman Spectroscopy*. John Wiley & Sons Ltd., 2005.

[26] P. P. Shorygin. Intensivnost linii kombinatsionnogo rasseyaniya i stroenie organicheskikh soedinenii. *Zhurnal Fizicheskoi Khimii*, 21(10): 1125–1134, 1947.

[27] A. C. Albrecht. Theory of raman intensities. *Journal Of Chemical Physics*, 34(5):1476–&, 1961.

[28] T. G. Spiro and T. C. Strekas. Resonance raman spectra of hemoglobin and cytochrome - inverse polarization and vibronic scattering. *Proceedings Of The National Academy Of Sciences Of The United States Of America*, 69(9):2622–&, 1972. Times Cited: 265.

[29] T. G. SPIRO and T. C. STREKAS. Resonance raman-spectra of heme proteins - effects of oxidation and spin state. *Journal Of The American Chemical Society*, 96(2):338–345, 1974.

[30] J. Soret. Analyse spectrale: Sur le spectre d absorption du sang dans la partie violette et ultra-violette. *Comptes rendus de l'Académie des sciences*, 97:1269–1270, 1883.

[31] T. G. Spiro and X. Y. Czernuszewicz, R. S.and Li. Metalloporphyrin structure and dynamics from resonance raman-spectroscopy. *Coordination Chemistry Reviews*, 100:541–571, April 1990.

[32] K. Nakamoto. Metal isotope-effect on metal-ligand vibrations. *Angewandte Chemie-International Edition*, 11(8):666–&, 1972.

[33] Y. Saito, K. Nakamoto, and M. Cordes. Metal isotope-effect on metal-ligand vibrations .8. far-infrared and raman spectra of zinc halide complexes of pyridine. *Spectrochimica Acta Part A-Molecular Spectroscopy*, A 28(8):1459–&, 1972.

[34] T. Kitagawa, M. Abe, and H. Ogoshi. Resonance raman-spectra of octaethylporphyrinato-ni(ii) and meso-deuterated and n-15 substituted derivatives .1. observation and assignments of non-fundamental raman lines. *Journal Of Chemical Physics*, 69(10):4516–4525, 1978.

[35] M. Fleischmann, P. J. Hendra, and Mcquilla.Aj. Raman-spectra of pyridine adsorbed at a silver electrode. *Chemical Physics Letters*, 26 (2):163–166, 1974.

[36] D. L. Jeanmaire and R. P. van Duyne. Surface raman spectroelectrochemistry .1. heterocyclic, aromatic, and aliphatic-amines adsorbed on

anodized silver electrode. *Journal Of Electroanalytical Chemistry*, 84 (1):1–20, 1977.

[37] M. G. Albrecht and J. A. Creighton. Anomalously intense raman-spectra of pyridine at a silver electrode. *Journal Of The American Chemical Society*, 99(15):5215–5217, 1977.

[38] J. B. Jackson and N. J. Halas. Surface-enhanced raman scattering on tunable plasmonic nanoparticle substrates. *Proceedings Of The National Academy Of Sciences Of The United States Of America*, 101: 17930–17935, 2004.

[39] J. R. Lombardi and R. L. Birke. A unified approach to surface-enhanced raman spectroscopy. *Journal Of Physical Chemistry C*, 112(14):5605–5617, April 2008.

[40] D.-S. Kerker, M.and Wang, H. Chew, O. Siiman, and L.A. Bumm. *Surface enhanced Raman scattering.* Plenum Press, New York and London, 1982.

[41] T. E. Furtak. Current understanding of the mechanism of surface enhanced raman-scattering. *Journal Of Electroanalytical Chemistry*, 150 (1-2):375–388, 1983.

[42] J. C. Rubim, P. Corio, M. C. C. Ribeiro, and M. Matz. Contribution of resonance raman-scattering to the surface-enhanced raman effect on electrode surfaces - a description using the time-dependent formalism. *Journal Of Physical Chemistry*, 99(43):15765–15774, 1995.

[43] J. F. Arenas, J. Soto, I. L. Tocon, D. J. Fernandez, J. C. Otero, and J. I. Marcos. The role of charge-transfer states of the metal-adsorbate complex in surface-enhanced raman scattering. *Journal Of Chemical Physics*, 116(16):7207–7216, 2002.

[44] J. F. Arenas, D. J. Fernandez, J. Soto, I. Lopez-Tocon, and J. C. Otero. Role of the electrode potential in the charge-transfer mechanism of

surface-enhanced raman scattering. *Journal Of Physical Chemistry B*, 107(47):13143–13149, 2003.

[45] A. Otto. The 'chemical' (electronic) contribution to surface-enhanced raman scattering. *Journal Of Raman Spectroscopy*, 36(6-7):497–509, June 2005.

[46] M. E. Lippitsch. Ground-state charge-transfer as a mechanism for surface-enhanced raman-scattering. *Physical Review B*, 29(6):3101–3110, 1984.

[47] J. R. Lombardi, R. L. Birke, T. H. Lu, and J. Xu. Charge-transfer theory of surface enhanced raman-spectroscopy - herzberg-teller contributions. *Journal Of Chemical Physics*, 84(8):4174–4180, April 1986.

[48] R. H. Ritchie. Plasma losses by fast electrons in thin films. *Physical Review*, 106(5):874–881, 1957.

[49] T. Turbadar. Complete absorption of light by thin metal films. *Proceedings Of The Physical Society Of London*, 73(469):40–44, 1959.

[50] A. Otto. Excitation of nonradiative surface plasma waves in silver by method of frustrated total reflection. *Zeitschrift Fur Physik*, 216(4): 398–&, 1968.

[51] E. Kretschmann and H. Raether. Radiative decay of non radiative surface plasmons excited by light. *Zeitschrift Fur Naturforschung Part A-Astrophysik Physik Und Physikalische Chemie*, A 23(12):2135–&, 1968.

[52] B. Rothenhausler, J. Rabe, P. Korpiun, and W. Knoll. On the decay of plasmon surface-polaritons at smooth and rough ag-air interfaces - a reflectance and photo-acoustic study. *Surface Science*, 137(1):373–383, 1984.

[53] W. Knoll. Interfaces and thin films as seen by bound electromagnetic waves. *Annual Review Of Physical Chemistry*, 49:569–638, 1998.

[54] R.B.M. Schasfoort and A.J. Tudos, editors. *Handbook of Surface Plasmon Resonance*. The Royal Society od Chemistry, 2008.

[55] N. Horn and M. Kreiter. Plasmon spectroscopy: Methods, pitfalls and how to avoid them. *Plasmonics*, in press, 2010.

[56] A.J. Bard and L.R. Faulkner. *Electrochemical Methods - Fundamentals and Applications*. John Wiley & Sons Ltd., 2001.

[57] R. Naumann, S. M. Schiller, F. Giess, B. Grohe, K. B. Hartman, I. Karcher, I. Koper, J. Lubben, K. Vasilev, and W. Knoll. Tethered lipid bilayers on ultraflat gold surfaces. *Langmuir*, 19(13):5435–5443, June 2003.

[58] M. Grosserueschkamp, C. Nowak, D. Schach, W. Schaertl, W. Knoll, and R. L. C. Naumann. Silver surfaces with optimized surface enhancement by self-assembly of silver nanoparticles for spectroelectrochemical applications. *Journal of Physical Chemistry C*, 113(41):17698–17704, 2009.

[59] B. V. Enustun and J. Turkevich. Coagulation of colloidal gold. *Journal Of The American Chemical Society*, 85(21):3317–&, 1963.

[60] G. Frens. Particle-size and sol stability in metal colloids. *Kolloid-Zeitschrift And Zeitschrift Fur Polymere*, 250(7):736–&, 1972.

[61] C. Hiser, D. A. Mills, M. Schall, and S. Ferguson-Miller. C-terminal truncation and histidine-tagging of cytochrome c oxidase subunit ii reveals the native processing site, shows involvement of the c-terminus in cytochrome c binding, and improves the assay for proton pumping. *Biochemistry*, 40(6):1606–1615, 2001. Times Cited: 25.

[62] C. Nowak, D. Schach, J. Gebert, M. Grosserueschkamp, R.B. Gennis, S. Ferguson-Miller, W. Knoll, D. Walz, and R.L.C Naumann. Oriented immobilization and electron transfer to the cytochrome c oxidase. *Journal of Solid State Electrochemistry*, 2010.

[63] R. Naumann, E. K. Schmidt, A. Jonczyk, K. Fendler, B. Kadenbach, T. Liebermann, A. Offenhausser, and W. Knoll. The peptide-tethered lipid membrane as a biomimetic system to incorporate cytochrome c oxidase in a functionally active form. *Biosensors & Bioelectronics*, 14 (7):651–662, 1999. Times Cited: 82.

[64] V.U. Kirste. *Elektrochemisch gesteuerte zeitaufgelöste Infrarotspektroskopie an Redox-Membranproteinen in einer biomimetischen Membran-Architektur*. PhD thesis, Max Planck Institute for Polymer Research, 2007.

[65] M. Plum. Orientierungsspezifische studie der cytochrom-c-oxidase in einer biomimetischen architektur auf metalloberflächen. Master's thesis, Max Planck Institute for Polymer Research, 2007.

[66] H. Wackerbarth, U. Klar, W. Gunther, and P. Hildebrandt. Novel time-resolved surface-enhanced (resonance) raman spectroscopic technique for studying the dynamics of interfacial processes: Application to the electron transfer reaction of cytochrome c at a silver electrode. *Applied Spectroscopy*, 53(3):283–291, March 1999.

[67] D. H. Murgida, P. Hildebrandt, J. Wei, Y. F. He, H. Y. Liu, and D. H. Waldeck. Surface-enhanced resonance raman spectroscopic and electrochemical study of cytochrome c bound on electrodes through coordination with pyridinyl-terminated self-assembled monolayers. *Journal Of Physical Chemistry B*, 108(7):2261–2269, February 2004.

[68] A. Bonifacio, D. Millo, C. Gooijer, R. Boegschoten, and G. van der Zwan. Linearly moving low-volume spectroelectrochemical cell for microliter-scale surface-enhanced resonance raman spectroscopy of heme proteins. *Analytical Chemistry*, 76(5):1529–1531, March 2004.

[69] D. Millo, A. Bonifacio, A. Ranieri, M. Borsari, C. Gooijer, and G. van der Zwan. ph-induced changes in adsorbed cytochrome c. voltammetric and surface-enhanced resonance raman characterization

performed simultaneously at chemically modified silver electrodes. *Langmuir*, 23(19):9898–9904, September 2007.

[70] J. Hrabakova, K. Ataka, J. Heberle, P. Hildebrandt, and D. H. Murgida. Long distance electron transfer in cytochrome c oxidase immobilised on electrodes. a surface enhanced resonance raman spectroscopic study. *Physical Chemistry Chemical Physics*, 8(6):759–766, February 2006.

[71] J. Grochol, R. Dronov, F. Lisdat, P. Hildebrandt, and D. H. Murgida. Electron transfer in sam/cytochrome/polyelectrolyte hybrid systems on electrodes: A time-resolved surface-enhanced resonance raman study. *Langmuir*, 23(22):11289–11294, October 2007.

[72] H. J. Yue, D. Khoshtariya, D. H. Waldeck, J. Grochol, P. Hildebrandt, and D. H. Murgida. On the electron transfer mechanism between cytochrome c and metal electrodes. evidence for dynamic control at short distances. *Journal Of Physical Chemistry B*, 110(40):19906–19913, October 2006.

[73] M. G. Friedrich. *Vibrational Spectroscopic and Electrochemical Investigations of Multi-centered Heme Proteins in Biomimetic Membrane Architectures*. PhD thesis, Max Planck Institute for Polymerresearch, Mainz, 2007.

[74] K. Ataka, F. Giess, W. Knoll, R. Naumann, S. Haber-Pohlmeier, B. Richter, and J. Heberle. Oriented attachment and membrane reconstitution of his-tagged cytochrome c oxidase to a gold electrode: In situ monitoring by surface-enhanced infrared absorption spectroscopy. *Journal Of The American Chemical Society*, 126(49):16199–16206, December 2004.

[75] M. G. Friedrich, F. Giess, R. Naumann, W. Knoll, K. Ataka, J. Heberle, J. Hrabakova, D. H. Murgida, and P. Hildebrandt. Active site structure and redox processes of cytochrome c oxidase immobilised in a novel biomimetic lipid membrane on an electrode. *Chemical Communications*, 21(21):2376–2377, 2004.

[76] M. Wolpert, O. Maneg, B. Ludwig, and P. Hellwig. Characterization of the cu-a center in the cytochrome c oxidase from thermus thermophilus for the spectral range 1800-500 cm(-1) with a combined electrochemical and fourier transform infrared spectroscopic setup. *Biopolymers*, 74(1-2):73–76, May 2004.

[77] S. J. Huo, Q. X. Li, Y. G. Yan, Y. Chen, W. B. Cai, Q. J. Xu, and M. Osawa. Tunable surface-enhanced infrared absorption on au nanofilms on si fabricated by self-assembly and growth of colloidal particles. *Journal Of Physical Chemistry B*, 109(33):15985–15991, August 2005.

[78] M. Osawa, K. Yoshii, K. Ataka, and T. Yotsuyanagi. Real-time monitoring of electrochemical dynamics by submillisecond time-resolved surface-enhanced infrared attenuated-total-reflection spectroscopy. *Langmuir*, 10(3):640–642, March 1994.

[79] A. Pucci. Ir spectroscopy of adsorbates on ultrathin metal films. *Physica Status Solidi B-Basic Solid State Physics*, 242(13):2704–2713, November 2005.

[80] M. Abe and Y. Kitagawa, T. Aand Kyogoku. Resonance raman-spectra of octaethylporphyrinato-ni(ii) and meso-deuterated and n-15 substituted derivatives .2. normal coordinate analysis. *Journal Of Chemical Physics*, 69(10):4526–4534, 1978.

[81] S. W. Han, Y. C. Ching, S. L. Hammes, and D. L. Rousseau. Vibrational structure of the formyl group on heme-a - implications on the properties of cytochrome-c-oxidase. *Biophysical Journal*, 60(1):45–52, July 1991.

[82] S. Z. Hu, I. K. Morris, J. P. Singh, K. M. Smith, and T. G. Spiro. Complete assignment of cytochrome-c resonance raman-spectra via enzymatic reconstitution with isotopically labeled hemes. *Journal Of The American Chemical Society*, 115(26):12446–12458, December 1993.

[83] H. Brunner, H. Sussner, and A. Mayer. Resonance raman scattering on heme group of oxyhemoglobin deoxyhemoglobin. *Journal Of Molecular Biology*, 70(1):153–156, 1972.

[84] M. C. Leopold and E. F. Bowden. Influence of gold substrate topography on the voltammetry of cytochrome c adsorbed on carboxylic acid terminated self-assembled monolayers. *Langmuir*, 18(6):2239–2245, March 2002.

[85] T. M. Nahir and E. F. Bowden. The distribution of standard rate constants for electron transfer between thiol-modified gold electrodes and adsorbed cytochrome c. *Journal Of Electroanalytical Chemistry*, 410(1):9–13, June 1996.

[86] I. Taniguchi, K. Toyosawa, H. Yamaguchi, and K. Yasukouchi. Voltammetric response of horse heart cytochrome-c at a gold electrode in the presence of sulfur bridged bipyridines. *Journal Of Electroanalytical Chemistry*, 140(1):187–193, 1982.

[87] A. S. Haas, D. L. Pilloud, K. S. Reddy, G. T. Babcock, C. C. Moser, J. K. Blasie, and P. L. Dutton. Cytochrome c and cytochrome c oxidase: Monolayer assemblies and catalysis. *Journal Of Physical Chemistry B*, 105(45):11351–11362, November 2001.

[88] C. Nowak, C. Luening, D. Schach, D. Baurecht, W. Knoll, and R. L. C. Naumann. Electron transfer kinetics of cytochrome c in the submillisecond time regime using time-resolved surface-enhanced infrared absorption spectroscopy. *Journal Of Physical Chemistry C*, 113(6):2256–2262, 2009.

[89] X. Y. Li, R. S. Czernuszewicz, J. R. Kincaid, P. Stein, and T. G. Spiro. Consistent porphyrin force-field .2. nickel octaethylporphyrin skeletal and substituent mode assignments from n-15, meso-d4, and methylene-d16 raman and infrared isotope shifts. *Journal Of Physical Chemistry*, 94(1):47–61, January 1990.

[90] A. Kranich, H. K. Ly, P. Hildebrandt, and D. H. Murgida. Direct observation of the gating step in protein electron transfer: Electric-field-controlled protein dynamics. *Journal Of The American Chemical Society*, 130(30):9844–9848, July 2008.

[91] A. Kassu, P. Robinson, A. Sharma, P. B. Ruffin, C. Brantley, and E. Edwards. Gold/silver coated nanoporous ceramic membranes: a new substrate for sers studies. *Proceedings of the SPIE - The International Society for Optical Engineering*, page 77640M (7 pp.), 2010.

[92] H. Zhao, H. G. Fu, C. G. Tian, Z. Y. Ren, and G. H. Tian. Fabrication of silver nanoparticles/single-walled carbon nanotubes composite for surface-enhanced raman scattering. *Journal Of Colloid And Interface Science*, 351(2):343–347, 2010.

[93] K. Kneipp, H. Kneipp, I. Itzkan, R. R. Dasari, and M. S. Feld. Surface-enhanced raman scattering and biophysics. *Journal Of Physics-Condensed Matter*, 14(18):R597–R624, May 2002.

[94] H. G. M. Edwards, E. M. Newton, D. L. Dickensheets, and D. D. Wynn-Williams. Raman spectroscopic detection of biomolecular markers from antarctic materials: evaluation for putative martian habitats. *Spectrochimica Acta Part A-Molecular And Biomolecular Spectroscopy*, 59(10):2277–2290, August 2003.

[95] E. B. Hanlon, R. Manoharan, T. W. Koo, K. E. Shafer, J. T. Motz, M. Fitzmaurice, J. R. Kramer, I. Itzkan, R. R. Dasari, and M. S. Feld. Prospects for in vivo raman spectroscopy. *Physics In Medicine And Biology*, 45(2):R1–R59, February 2000.

[96] A. G. Ryder. Surface enhanced raman scattering for narcotic detection and applications to chemical biology. *Current Opinion In Chemical Biology*, 9(5):489–493, October 2005.

[97] M. Moskovits. Surface-enhanced spectroscopy. *Reviews Of Modern Physics*, 57(3):783–826, 1985.

[98] H. Devoe. Optical properties of molecular aggregates .2. classical theory of refraction absorption and optical activity of solutions and crystals. *Journal Of Chemical Physics*, 43(9):3199–3208, 1965.

[99] H. Devoe. Optical properties of molecular aggregates .i. classical model of electronic absorption + refraction. *Journal Of Chemical Physics*, 41 (2):393–400, 1964.

[100] L. Gunnarsson, T. Rindzevicius, J. Prikulis, B. Kasemo, M. Kall, S. L. Zou, and G. C. Schatz. Confined plasmons in nanofabricated single silver particle pairs: Experimental observations of strong interparticle interactions. *Journal Of Physical Chemistry B*, 109(3):1079–1087, January 2005.

[101] H. Tamaru, H. Kuwata, H. T. Miyazaki, and K. Miyano. Resonant light scattering from individual ag nanoparticles and particle pairs. *Applied Physics Letters*, 80(10):1826–1828, March 2002.

[102] F. Svedberg, Z. P. Li, H. X. Xu, and M. Kall. Creating hot nanoparticle pairs for surface-enhanced raman spectroscopy through optical manipulation. *Nano Letters*, 6(12):2639–2641, December 2006.

[103] I. Romero, J. Aizpurua, G. W. Bryant, and F. J. G. de Abajo. Plasmons in nearly touching metallic nanoparticles: singular response in the limit of touching dimers. *Optics Express*, 14(21):9988–9999, October 2006.

[104] M. Grosserueschkamp, M. G. Friedrich, M. Plum, W. Knoll, and R. L. C. Naumann. Electron transfer kinetics of cytochrome c probed by time-resolved surface-enhanced resonance raman spectroscopy. *Journal Of Physical Chemistry B*, 113(8):2492–2497, February 2009.

[105] C. E. Taylor, J. E. Pemberton, G. G. Goodman, and M. H. Schoenfisch. Surface enhancement factors for ag and au surfaces relative to pt surfaces for monolayers of thiophenol. *Applied Spectroscopy*, 53(10): 1212–1221, October 1999.

[106] R. Wen and Y. Fang. An investigation of the surface-enhanced raman scattering (sers) effect from a new substrate of silver-modified silver electrode. *Journal Of Colloid And Interface Science*, 292(2):469–475, December 2005.

[107] T. Atay, J. H. Song, and A. V. Nurmikko. Strongly interacting plasmon nanoparticle pairs: From dipole-dipole interaction to conductively coupled regime. *Nano Letters*, 4(9):1627–1631, September 2004.

[108] E. C. Le Ru, E. Blackie, M. Meyer, and P. G. Etchegoin. Surface enhanced raman scattering enhancement factors: a comprehensive study. *Journal Of Physical Chemistry C*, 111(37):13794–13803, 2007.

[109] K. B. Lee, E. S. Jun, G. N. Lamar, I. N. Rezzano, R. K. Pandey, K. M. Smith, F. A. Walker, and D. H. Buttlaire. Influence of heme vinyl-protein and carboxylate protein contacts on structure and redox properties of bovine cytochrome-b5. *Journal Of The American Chemical Society*, 113(9):3576–3583, 1991. ISI Document Delivery No.: FJ121 Times Cited: 44 Cited Reference Count: 55 AMER CHEMICAL SOC.

[110] D. D. Schlereth, V. M. Fernandez, and W. Mantele. Protein conformational-changes in tetraheme cytochromes detected by ftir spectroelectrochemistry - desulfovibrio-desulfuricans norway-4 and desulfovibrio-gigas cytochromes-c3. *Biochemistry*, 32(35):9199–9208, 1993. ISI Document Delivery No.: LW440 Times Cited: 19 Cited Reference Count: 57 AMER CHEMICAL SOC.

[111] E. A. Gorbikova, K. Vuorilehto, M. Wikstrom, and M. I. Verkhovsky. Redox titration of all electron carriers of cytochrome c oxidase by fourier transform infrared spectroscopy. *Biochemistry*, 45(17):5641–5649, 2006.

[112] D. H. Murgida and P. Hildebrandt. Redox and redox-coupled processes of heme proteins and enzymes at electrochemical interfaces. *Physical Chemistry Chemical Physics*, 7(22):3773–3784, 2005. Times Cited: 46.

[113] B. Rost, J. Behr, P. Hellwig, O. M. H. Richter, B. Ludwig, H. Michel, and W. Mantele. Time-resolved ft-ir studies on the co adduct of paracoccus denitrificans cytochrome c oxidase: Comparison of the fully reduced and the mixed valence form. *Biochemistry*, 38(23):7565–7571, 1999. ISI Document Delivery No.: 206ZV Times Cited: 47 Cited Reference Count: 37 AMER CHEMICAL SOC.

[114] C. Leger, S. J. Elliott, K. R. Hoke, L. J. C. Jeuken, A. K. Jones, and F. A. Armstrong. Enzyme electrokinetics: Using protein film voltammetry to investigate redox enzymes and their mechanisms. *Biochemistry*, 42(29):8653–8662, 2003. Times Cited: 90.

[115] F. A. Armstrong, H. A. Heering, and J. Hirst. Reactions of complex metalloproteins studied by protein-film voltammetry. *Chemical Society Reviews*, 26(3):169–179, 1997. Times Cited: 225.

[116] H. M. Lee, T. K. Das, D. L. Rousseau, D. Mills, S. Ferguson-Miller, and R. B. Gennis. Mutations in the putative h-channel in the cytochrome c oxidase from rhodobacter sphaeroides show that this channel is not important for proton conduction but reveal modulation of the properties of heme a. *Biochemistry*, 39(11):2989–2996, 2000. Times Cited: 53.

[117] G. E. Heibel, P. Hildebrandt, B. Ludwig, P. Steinrucke, T. Soulimane, and G. Buse. Comparative resonance raman-study of cytochrome-c-oxidase from beef-heart and paracoccus-denitrificans. *Biochemistry*, 32 (40):10866–10877, 1993. Times Cited: 32.

[118] D. Schach, C. Nowak, R. Gennis, S. Ferguson-Miller, W. Knoll, D. Walz, and R. Naumann. Modeling direct electron transfer to a multi-redox center protein: Cytochrome c oxidase. *Journal of Electroanalytical Chemistry*, DOI 10.1016/j.jelechem.2010.07.009, 2010.

[119] C. Nowak, M. G. Santonicola, D. Schach, J. Zhu, R. B. Gennis, S. Ferguson-Miller, D. Baurecht, D. Walz, W. Knoll, and R. L. C.

Naumann. Conformational transitions and molecular hysteresis of cytochrome c oxidase: Varying the redox state by electronic wiring. *Soft Matter*, DOI:10.1039/C0SM00160K, 2010.

[120] M. Aki, T. Ogura, Y. Naruta, T. H. Le, T. Sato, and T. Kitagawa. Uv resonance raman characterization of model compounds of tyr(244) of bovine cytochrome c oxidase in its neutral, deprotonated anionic, and deprotonated neutral radical forms: Effects of covalent binding between tyrosine and histidine. *Journal of Physical Chemistry A*, 106 (14):3436–3444, 2002. Times Cited: 34.

[121] S. Dopner, J. Hudecek, B. Ludwig, H. Witt, and P. Hildebrandt. Structural changes in cytochrome c oxidase induced by cytochrome c binding. a resonance raman study. *Biochimica Et Biophysica Acta-Protein Structure and Molecular Enzymology*, 1480(1-2):57–64, 2000. Times Cited: 7.

[122] M. Grosserueschkamp, C. Nowak, W. Knoll, and R. L. C. Naumann. Time-resolved surface-enhanced resonance raman spectroelectrochemistry of heme proteins. *Spectroscopy-an International Journal*, 24(1-2):125–129, 2010. Times Cited: 0 13th European Conference on Spectroscopy of Biological Molecules AUG 28-SEP 02, 2009 Palermo, ITALY.

[123] P. A. Harmon, R. W. Hendler, and I. W. Levin. Resonance raman and optical spectroscopic monitoring of heme-a redox states in cytochrome-c-oxidase during potentiometric titrations. *Biochemistry*, 33(3):699–707, 1994. Times Cited: 8.

[124] T. Kitagawa and T. Ogura. Time-resolved resonance raman investigation of oxygen reduction mechanism of bovine cytochrome c oxidase. *Journal Of Bioenergetics And Biomembranes*, 30(1):71–79, 1998.

[125] T. Kitagawa and T. Ogura. Time-resolved resonance raman study of dioxygen reduction by cytochrome c oxidase. *Pure and Applied Chemistry*, 70(4):881–888, 1998. Times Cited: 1 8th International Confer-

ence on Bioinorganic Chemistry JUL 27-AUG 01, 1997 YOKOHAMA, JAPAN.

[126] D. Murgida and P. Hildebrandt. Surface-enhanced vibrational spectroelectrochemistry: Electric-field effects on redox and redox-coupled processes of heme proteins. *Surface-Enhanced Raman Scattering: Physics and Applications*, 103:313–334, 2006. Times Cited: 7.

[127] A. L. Troutier and C. Ladaviere. An overview of lipid membrane supported by colloidal particles. *Advances in Colloid and Interface Science*, 133(1):1–21, 2007. ISI Document Delivery No.: 215EW Times Cited: 31 Cited Reference Count: 118 Troutier, Anne-Lise Ladaviere, Catherine ELSEVIER SCIENCE BV.

[128] G. Nordlund, R. Lonneborg, and P. Brzezinski. Formation of supported lipid bilayers on silica particles studied using flow cytometry. *Langmuir*, 25(8):4601–4606, 2009. ISI Document Delivery No.: 434NP Times Cited: 5 Cited Reference Count: 27 Nordlund, Gustav Lonneborg, Rosa Brzezinski, Peter AMER CHEMICAL SOC.

[129] R. W. Hendler, K. V. S. Reddy, R. I. Shrager, and W. S. Caughey. Analysis of the spectra and redox properties of pure cytochromes-aa3. *Biophysical Journal*, 49(3):717–729, 1986. ISI Document Delivery No.: A4736 Times Cited: 28 Cited Reference Count: 21 BIOPHYSICAL SOCIETY.

[130] S. Sivasankar, S. Subramaniam, and D. Leckband. Direct molecular level measurements of the electrostatic properties of a protein surface. *Proceedings Of The National Academy Of Sciences Of The United States Of America*, 95(22):12961–12966, 1998. Times Cited: 38.

[131] D. Heitbrink, H. Sigurdson, C. Bolwien, P. Brzezinski, and J. Heberle. Transient binding of co to cu-b in cytochrome c oxidase is dynamically linked to structural changes around a carboxyl group: A time-resolved step-scan fourier transform infrared investigation. *Biophysical Journal*,

82(1):1–10, 2002. ISI Document Delivery No.: 511DZ Times Cited: 35 Cited Reference Count: 53 BIOPHYSICAL SOCIETY.

[132] O. Einarsdottir and I. Szundi. Time-resolved optical absorption studies of cytochrome oxidase dynamics. *Biochimica Et Biophysica Acta-Bioenergetics*, 1655(1-3):263–273, 2004. ISI Document Delivery No.: 815ZD Times Cited: 13 Cited Reference Count: 104 ELSEVIER SCIENCE BV.

[133] E. Pinakoulaki, C. Koutsoupakis, S. Stavrakis, M. Aggelaki, G. Papadopoulos, V. Daskalakis, and C. Varotsis. Structural dynamics of heme-copper oxidases and nitric oxide reductases: time-resolved step-scan fourier transform infrared and time-resolved resonance raman studies. *Journal Of Raman Spectroscopy*, 36(4):337–349, 2005. Times Cited: 6.

[134] C. Koutsoupakis, T. Soulimane, and C. Varotsis. Probing the q-proton pathway of ba(3)-cytochrome c oxidase by time-resolved fourier transform infrared spectroscopy. *Biophysical Journal*, 86(4):2438–2444, 2004. ISI Document Delivery No.: 808KI Times Cited: 14 Cited Reference Count: 34 BIOPHYSICAL SOCIETY.

[135] T. Kitagawa. Structures of reaction intermediates of bovine cytochrome c oxidase probed by time-resolved vibrational spectroscopy. *Journal of Inorganic Biochemistry*, 82(1-4):9–18, 2000. ISI Document Delivery No.: 383GA Times Cited: 20 Cited Reference Count: 36 ELSEVIER SCIENCE INC.

[136] T. Ogura and T. Kitagawa. Resonance raman characterization of the p intermediate in the reaction of bovine cytochrome c oxidase. *Biochimica Et Biophysica Acta-Bioenergetics*, 1655(1-3):290–297, 2004. ISI Document Delivery No.: 815ZD Times Cited: 17 Cited Reference Count: 27 ELSEVIER SCIENCE BV.

[137] C. Varotsis, Y. Zhang, E. H. Appelman, and G. T. Babcock. Resolution of the reaction sequence during the reduction of o2 by cytochrome-

oxidase. *Proceedings Of The National Academy Of Sciences Of The United States Of America*, 90(1):237–241, 1993. ISI Document Delivery No.: KF407 Times Cited: 138 Cited Reference Count: 47 NATL ACAD SCIENCES.

[138] T. Ogura, S. Takahashi, S. Hirota, K. Shinzawaitoh, S. Yoshikawa, E. H. Appelman, and T. Kitagawa. Time-resolved resonance raman elucidation of the pathway for dioxygen reduction by cytochrome-c-oxidase. *Journal of the American Chemical Society*, 115(19):8527–8536, 1993. Times Cited: 89.

[139] T. Ogura, S. Takahashi, K. Shinzawaitoh, S. Yoshikawa, and T. Kitagawa. Time-resolved resonance raman investigation of cytochrome-oxidase catalysis - observation of a new oxygen-isotope sensitive raman band. *Bulletin Of The Chemical Society Of Japan*, 64(10):2901–2907, 1991.

[140] E. Pinakoulaki, U. Pfitzner, B. Ludwig, and C. Varotsis. The role of the cross-link his-tyr in the functional properties of the binuclear center in cytochrome c oxidase. *Journal of Biological Chemistry*, 277 (16):13563–13568, 2002. Times Cited: 52.

[141] E. Pinakoulaki, M. Vamvouka, and C. Varotsis. The active site structure of heme a(3)(3+)-c n-cu-b(2+) of cytochrome aa(3) oxidase as revealed from resonance raman scattering. *Journal of Physical Chemistry B*, 107(36):9865–9868, 2003. Times Cited: 4.

[142] T. Takahashi, S. Kuroiwa, T. Ogura, and S. Yoshikawa. Probing the oxygen activation reaction in intact whole mitochondria through analysis of molecular vibrations. *Journal Of The American Chemical Society*, 127(28):9970–9971, 2005. Times Cited: 6.

[143] D. A. Proshlyakov, M. A. Pressler, and G. T. Babcock. Dioxygen activation and bond cleavage by mixed-valence cytochrome c oxidase. *Proceedings Of The National Academy Of Sciences Of The United States Of America*, 95(14):8020–8025, 1998. ISI Document Delivery No.:

ZZ317 Times Cited: 194 Cited Reference Count: 58 NATL ACAD SCIENCES.

[144] C. Varotsis, W. H. Woodruff, and G. T. Babcock. Direct detection of a dioxygen adduct of cytochrome-a3 in the mixed-valence cytochrome-oxidase dioxygen reaction. *Journal of Biological Chemistry*, 265(19):11131–11136, 1990. ISI Document Delivery No.: DL655 Times Cited: 46 Cited Reference Count: 46 AMER SOC BIOCHEMISTRY MOLECULAR BIOLOGY INC.

[145] I. Szundi, G. L. Liao, and O. Einarsdottir. Near-infrared time-resolved optical absorption studies of the reaction of fully reduced cytochrome c oxidase with dioxygen. *Biochemistry*, 40(8):2332–2339, 2001. ISI Document Delivery No.: 404VA Times Cited: 26 Cited Reference Count: 47 AMER CHEMICAL SOC.

[146] T. Nilsson. Photoinduced electron-transfer from tris(2,2'-bipyridyl)ruthenium to cytochrome-c-oxidase. *Proceedings Of The National Academy Of Sciences Of The United States Of America*, 89(14):6497–6501, 1992. ISI Document Delivery No.: JD675 Times Cited: 81 Cited Reference Count: 30 NATL ACAD PRESS.

[147] I. Szundi, J. A. Cappuccio, N. Borovok, A. B. Kotlyar, and O. Einarsdottir. Photoinduced electron transfer in the cytochrome c/cytochrome c oxidase complex using thiouredopyrenetrisulfonate-labeled cytochrome c optical multichannel detection. *Biochemistry*, 40 (7):2186–2193, 2001. ISI Document Delivery No.: 404TR Times Cited: 19 Cited Reference Count: 23 AMER CHEMICAL SOC.

[148] M. Grosserueschkamp, R. B. Gennis, S. Ferguson-Miller, W. Knoll, and R. L. C. Naumann. Cytochome c oxidase: Electrochemically induced electron transfer probed by surface-enhanced resonance raman spectroscopy (serrs). *Journal of Physical Chemistry B*, submitted.